Optimization of the Process for Sol-Gel Derived ZnO:Al Thin Films for Transparent Conducting Oxide Applications

by
Matthew Nagorski

A Thesis
Presented to Lakehead University
in Partial Fulfillment of the Requirement for the Degree of
Master of Science
in
Electrical and Computer Engineering

Thunder Bay, Ontario, Canada

April, 2021

Abstract

Transparent and conducting Al-doped ZnO thin films with c-axis-preferred orientation were prepared on glass substrate via sol-gel route. The physical, optical and electrical properties were investigated to determine an optimal withdrawal speed, aluminum source and treatment in order to obtain a smooth, dense, highly crystalline, conductive and transparent thin film with a high figure of merit for transparent conducting oxide applications. An optimal withdrawal speed was found to be 2.5 cm/min. Optimal aluminum source and concentration was found to be 0.5 at.% using aluminum chloride hexahydrate. An additional treatment in an N_2 environment was found to be the best method to improve the electrical properties of the films while maintaining high crystallinity and transparency.

Acknowledgments

I would like to begin by expressing my gratitude to my supervisor Dr. Alexandrov. Your classes had sparked my interest in material science and the desire to further my education on the subject. Thank you for the opportunity to do my masters under your supervision and providing invaluable guidance throughout this research. I thank my research colleagues for making feel welcome, for the stimulating discussions, the countless memories made together and for your support throughout my research. To my program coordinator Dr. Natarajan, I thank you for challenging me and molding me into the person I am today. Your vast knowledge inspires me to be the life long learner that you are and to never take anything at face value. Finally, I would like to thank you my parents and loved ones for their tireless support throughout this process.

Matthew Nagorski
mnagorsk@lakeheadu.ca

"Nothing in life is to be feared, it is only to be understood. Now is the time to understand more, so that we may fear less" - Marie Curie

Contents

List of Figures

List of Tables

Key Terms

Ligand Ions or molecules capable of bonding to a central metal atom to form a coordination complex

Polydendate Ligand Ions or molecules capable of forming multiple bonds to a central metal atom via two or more atoms

Chelation process in which a polydentate ligand bonds to a central metal ion, forming a ring. The complex produced is called a chelate, and the polydentate ligand is referred to as chelating agent

Sol-Gel A inexpensive chemical solution deposition method

Colloid Suspension in which dispersed phase is ∼1-1000 nm and gravitational forces are negligible. Interactions are dominated by short-range forces. E.g. van der Waals and surface charges

Polymer large molecule made from many smaller molecules (monomers) joined together, end to end

Hydrolysis reaction Polymers being broken down into monomers known as hydrolysis, "to split water", typically a water molecule is 'consumed' in the reaction

Condensation reaction molecules joining together to form a larger molecule, typically releasing a water molecule in the process E.g. two amino acids combine via covalent bond between amine nitrogen of one amino acid and carboxyl carbon of second amino acid

Chapter 1

Introduction, Motivation, and Objectives

1.1 Motivation

The motivation for this work stems from the prevalence of transparent conducting oxides in a wide range of applications. Historically, indium tin oxide has been used for these numerous applications with the majority of ITO being used as contacts in PV cells, and as electrodes in touch screens and flat panel displays. However, the use of transparent conducting oxides is only growing and the rarity as well as toxicity of indium is driving researchers to find an alternative material. ZnO is on the forefront of this movement due to its material properties, abundance, and nontoxic nature. While ZnO can be synthesized using various techniques, keeping with the theme of low cost alternatives leads this work to adopt the sol-gel route which has been extensively researched up until this point. By building on findings of previous groups, one is motivated to outline a optimal methodology to synthesize ZnO thin films via sol-gel route with a high FoM for transparent conducting oxide applications.

1.2 Thesis Objectives

The first objective of this thesis is to provide detailed information on transparent conducting oxides, zinc oxide and sol-gel derived ZnO. Through extensive literature review, reasoning for choices on type and concentration of solvent, stabilizer and precursor are provided. The second objective is to find additional optimal process parameters through numerous experiments in order

to obtain a smooth, dense, highly crystalline, conductive and transparent ZnO thin film with a high FoM for transparent conducting oxide applications. These experiments focus on withdrawal speed, aluminum source and additional treatments on the films. The focus being on their effect on the structural, electrical, and optical properties of the films with the end goal to obtain a sol-gel derived ZnO:Al thin film with a high FoM for transparent conducting oxide applications.

1.3 Thesis Chapter Outline

In chapter 2, transparent conducting oxides are discussed. The chapter explains what transparent conducting oxides are, how they achieve the unique material properties of being electrically conductive while also being transparent in the visible range and some common applications where transparent conducting oxides are used. In chapter 3, zinc oxide is discussed. The focus being on the properties of zinc oxide including: structural, electrical and optical properties. As well as how zinc oxide thin films are commonly prepared and what applications they are commonly used for. Chapter 4 details sol-gel chemistry. The chapter covers the role and effect of the ingredients used for sol-gel derived ZnO. As well as the post-deposition processes which also play an important role in the properties of the final ZnO thin film. Chapter 5 explains the fabrication and characterization techniques used to produce and characterize the sol-gel derived ZnO thin films in this work. Chapter 6, outlines the three experiments conducting in this work in order to find optimal parameters which result in the desirable properties of the obtained ZnO thin films. The results from the experiments are presented in chapter 6. The focus being on the structural, optical and electrical properties of the films produced. A FoM is used to quantify the performance of the films produced for transparent conducting oxide applications. Lasty, chapter 7 summarizes the work done in this thesis.

Chapter 2

Transparent Conducting Oxides

2.1 Introduction

Transparent conducting oxides (TCOs) are a unique class of materials which exhibit both transparency and electrical conductivity. This combination of material properties is unique because transparency and electrical conductivity are basically incompatible. Transparent materials are typically insulators such as SiO_2 glasses. While on the other hand, highly conductive materials usually show metallic luster or deep dark color such as Ag and Al metals which show metallic color with high reflectivity. Therefore, to obtain TCOs, it is necessary to convert transparent insulators to highly conducting semiconductors by increasing electrical conductivity without coloration. This is typically done via substitutional doping in which other elements are introduced into the material in order to alter its properties.

The current use of TCOs in industry is dominated by just a few materials and over the last 30 years, much of the materials work on TCOs has been focused on minor variants of ZnO, In_2O_3 and SnO_2. Thin films of TCOs are widely used in flat panel displays, photovoltaics, energy-efficient low-emittance windows and as oxide based transistors used in flexible devices [1, 2, 3, 4]. Transition-metal-based oxides also offer a broader range of materials applications including ferroelectric, piezoelectric, thermoelectric, gas sensing, superconducting among other applications [5]. Tin oxide is used in PV modules, touch screens, and flat panel displays. However, for the majority of flat panel display applications, crystalline tin dope indium oxide (indium-tin-oxide, ITO) and, more recently, amorphous In-Zn-O (IZO) are the TCOs used most often. It is estimated that between 30 and 40% of the display industry uses IZO [5]. Currently, the fastest

growing portion of the TCO market is for photovoltaic cells. The global PV market is valued at $53.916 billion in 2018, and is projected to reach $333.725 billion by 2026 [6].

In order to be used in the applications just mentioned, TCOs must have a high optical transmission (>80%) in the visible spectrum (380 to 700 nm) which is achieved due to their large band gap, typically greater than 3.3 eV. As well has high electrical conductivity in the range of 1 to 10^4 S cm^{-1} . These opto-electrical properties can be changed by doping the material as in the case of tin doped indium oxide (ITO). Table 2.1 lists dopants or compounds used in doping of various TCO materials.

Table 2.1: Doping of TCO materials [7]

Material	Dopant or compound
SnO_2	Sb, F, As, Nb, Ta
In_2O_3	Sn, Ge, Mo, F, Ti, Zr, Hf, Nb, Ta, W, Te
ZnO	Al, Ga, B, In, Y, Sc, F, V, S, Ge, Ti, Zr, Hf
CdO	In, Sn
ZnO-SnO_2	Compounds Zn_2SnO_4, $ZnSnO_3$
ZnO-In_2O_3	$Zn_2In_2O_5$, $Zn_3In_2O_6$
In_2O_3-SnO_2	$In_4Sn_3O_{12}$
CdO-SnO_2	Cd_2SnO_4, $CdSnO_3$
CdO-In_2O_3	$CdIn_2O_4$
$MgIn_2O_4$	
$GaInO_3$, $(Ga, In)_2O_3$	Sn, Ge
$CdSb_2O_6$	Y
Zn-In_2O_3-SnO_2	$Zn_2In_2O_5$-$In_4Sn_3O_{12}$
CdO-In_2O_3-SnO_2	$CdIn_2O_4$-Cd_2SnO_4
ZnO-CdO-In_2O_3-SnO_2	

2.2 Electrical Conductivity

Electrical conductivity is a fundamental, material specific property of the materials ability to conduct electric current, i.e. allow electrons to travel in the material when subjected to an external electric field. Electrical current I in materials is expressed by Ohm's law given in Eq.(2.1), where V and R are potential difference and resistance respectively. The microscopic form of Ohm's law is expressed in Eq.(2.2). Where J, σ, E are current density, conductivity and electric field strength respectively.

$$I = \frac{V}{R} \tag{2.1}$$

$$J = \sigma E \tag{2.2}$$

$$\sigma = ne\mu \tag{2.3}$$

Conductivity is a useful parameter to categorize materials into metals, semiconductors and insulators. Metals like Ag and Al have relatively high electrical conductivities on the order of 10^5 S cm^{-1}. Semiconductors like Si, when doped with impurities to increase conductivity, can have electrical conductivities on the order of 10^2 S cm^{-1}. The conductivity of typical TCOs like the widely used ITO are somewhere between these two ranges, having conductivity on the order of 10^4 S cm^{-1}. Electrical conductivity is the product of carrier concentration i.e number of free electrons (or holes) per unit volume and the mobility of these charge carriers in the material. The relationship is expressed in Eq.(2.3). Where n, e, μ are carrier concentration of electrons, elementary electric charge and carrier mobility respectively. p is be used to denote carrier concentration if the majority of charger carriers are holes (p-type semiconductor). However, as the majority carriers are electrons in almost all TCOs (n-type semiconductor), n is used in Eq.(2.3).

Carrier mobility can be described as the ease in which charge carriers can move through a material. It is defined in terms of the average scattering time (τ) and the effective mass of the charge carrier (m^*) as expressed in Eq.(2.4). It is evident from Eq.(2.4) that in order to increase mobility, the scattering time must be increased or the effective mass must be decreased. The latter involves new material development while the former relates to the quality of thin film. In general, anything that slows the movement of charge carriers through a material (decreases τ) will result in a decrease in mobility and thus a decrease in conductivity. According to Matthiesens rule [8], resistivity arises from independent but additive scattering processes, such as scattering due to impurities, defects, and grain boundaries. In typical semiconductor materials, the most important sources of scattering are ionized impurity scattering and acoustic phonon scattering, also known as lattice scattering. Grain boundary scattering is only significant when the grains

are smaller than the mean free path of the electron (or hole). Phase separation and porosity will also result in scattering. The latter of which is of particular concern in solution-based processes, as pores can form when solvent and gaseous decomposition products leave the material.

$$\mu = \frac{e\tau}{m^*} \tag{2.4}$$

Table 2.2 lists electrical properties of a typical metal (Ag), doped semiconductor (Si:P n), heavily doped (degenerate) semiconductor (Si:p n++) and transparent conducting oxide (ITO)

Table 2.2: Electrical properties of Ag, Si:P and ITO [9]

Materials	Conductivity σ (S cm^{-1})	Carrier concentration n (cm $^{-3}$)	Mobility μ (cm^{2}V^{-1}s^{-1})
Ag	6.80 x 10^5	5.76 x 10^{22}	72
Si:P n	10^{-2}	10^{14}	1500
Si:P n++	10^2	10^{19}	100
ITO	10^4	10^{20}-10^{21}	20-80

In the case of metals such as Ag, the conductivity arises from the relatively high carrier concentration, as the mobility is not significantly high compared to other materials in Table 2.2. For the case of Si doped with phosphorous, the carrier concentration is relatively low, however, due to its much higher carrier mobility compared to Ag, it's able to behave as an electrical conductor. Further doping of Si will result in increased conductivity due to increased carrier concentration but at a detriment to mobility due to carrier scattering. ITO has similar carrier mobilities to Ag and degenerate P-doped Si. However, the carrier concentration is much higher than in the case of degenerate P-doped Si but lower than Ag resulting in a conductivity somewhere between the two materials.

2.3 Transparency

As mentioned in 2.1, the transparency in the visible range of TCOs comes from the materials wide energy band gap (>3.3 eV). The energy band gap is the range of energies in a solid which no electronic state can exist, i.e. no energy levels which an electron can occupy. A energy band gap exists because in a single atom, electrons reside in atomic orbitals having a discrete energy level. When many atoms ($\sim$10^{22} atoms/cm^3) come together to form a sold, the atomic orbitals overlap and hybridize to form new obitals called molecular orbitals. The previously discrete energy levels form continuous energy bands composed of closely spaced energy levels. The energy bands of

interest are commonly referred to as the valence band and conduction band. The valence band is the highest range of energy levels an electron can occupy at 0K. The conduction band is the lowest range of vacant energy levels and the separation between the two bands is known as the energy band gap. For TCOs, the conduction band is composed of empty metal ns^0 orbitals and the valence band is composed of occupied oxygen 2p orbitals. The molecular orbital diagram and resulting band structure is illustrated in Fig. 2.1.

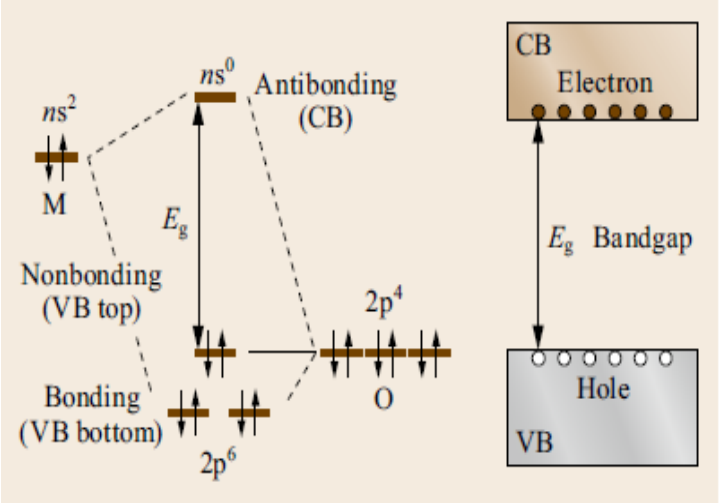

Figure 2.1: Molecular orbital hybridization and band structure in metal oxides [9]

TCOs are transparent in the visible range because photons (quanta of light) in the visible range do not have sufficient energy to be absorbed thereby exciting an electron from the valence band to conduction band and therefore do not interact with the material. Instead, the photons pass through the material and giving rise to its transparency in the visible range. At higher energies (shorter wavelengths), closer to ultraviolet, the photons have sufficient energy to excite electrons from the valence band to conduction band and the light is absorbed by the material resulting in a short wavelength cutoff in the transmission at ∼300 nm due to this fundamental band gap excitation. At low energies (longer wavelengths), near infrared, there is gradual decrease in the transparency and increase in reflectivity due to collective motion of conducting (free) carriers in the material. At such wavelengths, the charge carriers in the conduction band of the material oscillate at the frequency of the incident light, called plasma oscillation (plasmons) and results in reflection of the incident light at the surface of the material. However, as the wavelength decreases towards the visible range, the carriers can not catch up with the fast electric

field oscillations of light and the light is transmitted through the material.

A typical optical spectra of a ZnO TCO is illustrated in Fig. 2.2 showing transmission, reflection and absorption. Across the visible range, oscillations in transmission and reflection are due to thin film interference. There's the short wavelength cut off at ∼300 nm in transmission and a gradual decrease in transmission starting at ∼1000 nm due to collective oscillation of conduction band electrons (plasmons). Maximum absorption occurs at ∼1500 nm which corresponds to the characteristic wavelength of the plasmons denoted by λ_p. The plasmon frequency, ω_p which can be converted to plasmon wavelength are given in Eq.(2.5) and Eq.(2.6) respectively. Where n, m, ϵ_0 and c denote carrier concentration, electron rest mass, permittivity and speed of light in vacuum respectively. Above this plasmon frequency, reflection increases, again, due to collective oscillation of conduction band electrons.

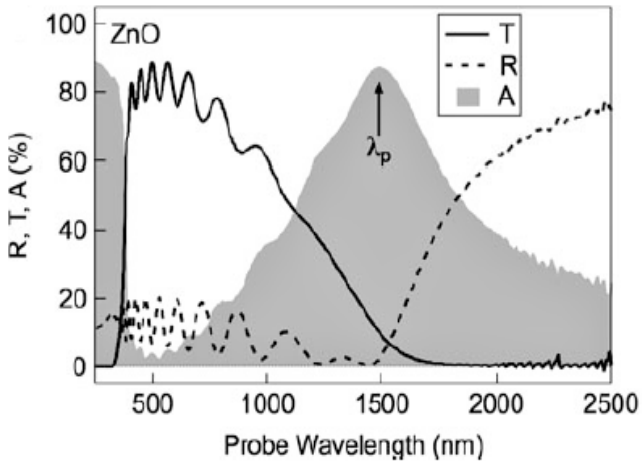

Figure 2.2: Typical optical spectra of ZnO TCO [5]

$$\omega_p = \frac{ne^2}{\epsilon_0 m} \tag{2.5}$$

$$\lambda_p = \frac{2\pi c}{e}\sqrt{\frac{\epsilon_0 m}{n}} \tag{2.6}$$

Eq.(2.6) reveals that as the number of electrons in the conduction band, n, is increased, for example by substituional doping, the plasmon wavelength shifts to shorter wavelengths as $\lambda_p \propto 1/\sqrt{n}$. This creates a fundamental tradeoff between conductivity and transparency at longer

wavelengths. At very high electron concentrations, this can even decreases transparency in the visible range. This is illustrated in Fig. 2.3. The SnO_2 with a lower sheet resistance, i.e. higher conductivity, exhibits lower transmission at higher wavelengths. Depending on the application, this could affect performance or even deem the material unusable for that particular application. For example, the SnO_2 with a lower sheet resistance in Fig. 2.3 would be unusable for optical telecommunication applications at 1500 nm.

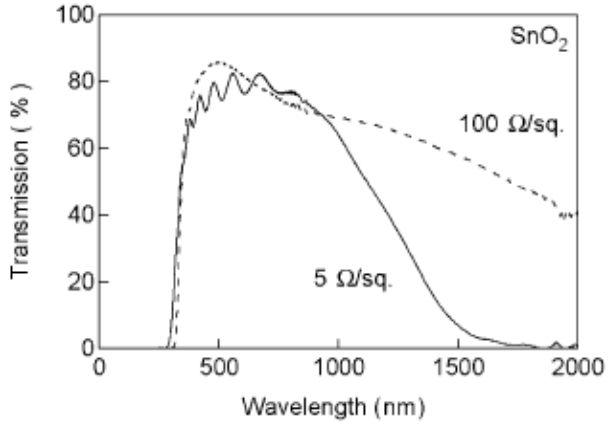

Figure 2.3: Optical spectra of SnO_2 TCO with different sheet resistance [5]

Conduction band electrons not only influence the infrared region but also in the ultraviolet region. As the carrier concentration increases, more electrons occupy the lowest energy levels of the conduction band. As a result, there is a shift in the absorption edge to higher energies (shorter wavelengths), enlarging the apparent energy band gap because electrons from the valence band require more energy to be excited higher in conduction band since the lower energies are already occupied. This energy shift is called band filling or Burstein-Moss shift. This is illustrated in Fig. 2.4 which shows a tauc plot, a typical plot used to determine the optical band gap. The shift in optical band gap from E_{g0} to E_g is due to filling of the lowest conduction bands as shown in the inset in Fig. 2.4

2.4 Applications

As mentioned in section (2.1), TCOs have a wide variety of uses including but not limited to: low-emissivity windows, solar cells, flat-panel displays, electrochromatic mirrors and windows, defrosting windows, oven windows, static dissipation and touch-panel controls. Depending on the

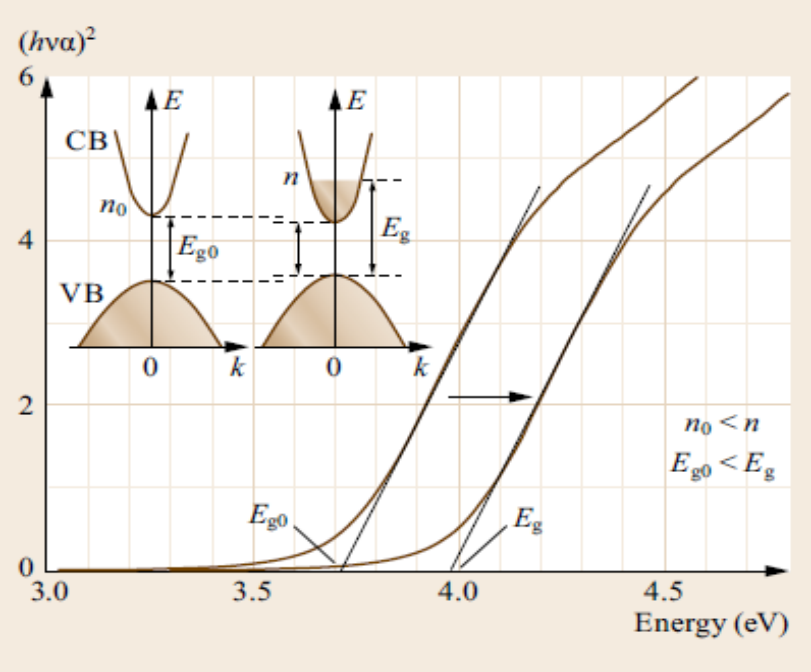

Figure 2.4: Shift of optical band gap due to Burstein-Moss shift [9]

application, specific material properties could be critical. Table 2.3 lists the important properties to consider depending on the application and the best material(s) of choice.

Table 2.3: Choice of TCO [10]

Property	Material
Highest transparency	ZnO:F, Cd_2SnO_4
Highest conductivity	In_2O_3:Sn
Lowest plasmon frequency	SnO_2:F, ZnO:F
Highest plasmon frequency	In_2O_3:Sn
Highest work function, best contact to p-Si	SnO_2:F, $ZnSnO_3$
Lowest work function, best contact to n-Si	ZnO:F
Best thermal stability	SnO_2:F, Cd_2SnO_4
Best mechanical durability	SnO_2:F
Best chemical durability	SnO_2:F
Easiest to etch	ZnO:F
Best resistance to H plasmas	ZnO:F
Lowest deposition temperature	In_2O_3:Sn, ZnO:B
Least toxic	ZnO:F, SnO_2:F
Lowest cost	SnO_2:F

TCOs on window glass improve the energy efficiency of the window because the free electrons reflect infrared radiation for wavelengths longer than the plasmon wavelength. These are known as

low-emmissivity (low-e) windows. In cold climates, the plasmon wavelength should be fairly long, approximately 2 μm, so most of the solar spectrum is transmitted into heat inside the building. In hot climates, a short plasmon wavelength, $\leq$1 μm, is desirable, so that the near-infrared portion of incident sunlight can be reflected out of the building [10]. For other TCO-on-glass applications like electrochromatic windows, defrosting windows, and oven windows, the considerations when choosing a TCO material are low cost, stability and durability.

In photovoltaics, the front surface of solar cells contact is covered by transparent electrodes. In single-crystal silcon cells, the electrode is typically highly doped silicon. However, in flexible thin-film solar cells and other amorphous-silicon cells grown on flexible steel or plastic substrates, the electrodes are typically fluorine doped tin oxide. In the case of thin-film cells grown on plastic substrates, low temperature (<200 °C) deposition is required thus alternatives such as ZnO:B or In_2O_3:Sn are used since they can be deposited at low temperatures.

For flat-panel displays, etchabilility is an important consideration in forming patterns in the TCO electrode. In addition, high conductivity is desirable because the etch patterns create height variations and therefore a thinner, more conductive material is preferred to keep the topography as smooth as possible. ITO has dominated this field, however due to

2.5 Figure of Merit

As mentioned in 2.3, there exists an inherit trade off between conductivity and transparency. As the carrier concentration, n increases, the plasmon wavelength, λ_p is shifted to shorter wavelengths and therefore narrows the transparency range. An effective TCO should have high electrical conductivity combined with low absorption in the visible range. Therefore, an appropriate quantitative measure of a TCO performance is the ratio of electrical conductivity, σ to the visible absorption coefficient α. The first successful suggested definition of a figure of merit (FoM) was reported by Haacke, given in Eq.(2.7) [11], in which the dimension is Ω^{-1} and T, R_{sh} represent optical transmittance and sheet resistance respectively. A larger value indicates better performance. With a similar dimension, a more practical definition was proposed by Jain and Kulshreshtha [12], which evaluates the performance independent of thickness given in Eq.(2.8). A more sophisticated definition first proposed by Gruner and later modified by Coleman which relies on relationship that transmittance and sheet resistance are correlated as the ratio of dc conductivity to the optical conductivity [13, 14]. The derived equation is given in Eq.(2.9) [15].

$$FoM = T^{10}/R_{sh} \tag{2.7}$$

$$FoM = -R_{sh} ln(T)^{-1} \tag{2.8}$$

$$FoM = 188.5[(R_{sh} * T^{-0.5} - 1)]^{-1} \tag{2.9}$$

Chapter 3

Zinc Oxide

3.1 Introduction

Zinc oxide is an inorganic binary compound semiconducting metal oxide. It belongs to both II-VI and oxide semiconductor groups. It is composed of group II zinc and group VI oxygen. Both of which are abundantly available in the earths crust with 132 ppm of Zn and 49.4% O [16]. Zinc oxide occurs naturally as the mineral zincite, which crystallizes in the hexagonal wurzite structure $P6_3mc$ [17]. The first discovery of zincite was in 1810 by Bruce in Franklin (New Jersey, USA). Other zincite deposits can be found in Sarawezza (Tuscany, Italy), Tsumeb (Namibia), Olkusz (Poland), Spain, Tasmania, and Australia.

Investigation of zinc oxide dates back to 1912, following the beginning of the semiconductor age which was triggered by the invention of the transistor [1]. Later in 1960, the first electronic application of zinc oxide as a thin layer for surface acoustic wave devices was developed after the discovery of good piezoelectric properties in zinc oxide [2]. The present resurgence on ZnO research began in the 1990s with numerous conferences, workshops and more than 2000 ZnO-related papers in 2005, with even higher numbers in 2006, compared to slightly more than 100 in 1970 [18]. The recent increased interest is based on the possibility to grow epitaxial layers, quantum wells, nanorods and related nano-structures or quantum dots with the hope to obtain:

- a material for blue/UV optoelectronics, including light emitting diodes or laser diodes in addition to (or instead of) GaN-based structures
- a radiation resistant material for electronic devices in a corresponding environment

- a material for electronic circuits that is transparent in the visible range and/or usable at elevated temperatures
- a diluted- or ferro-magnetic material, when doped with Co, Mn, Fe, V, etc., for spintronics applications
- a transparent, highly conducting oxide, when doped with Al, Ga, In, etc., as a cheaper alternative to ITO.

Though progress has been made, the long standing problem that exists for ZnO is the challenge to reliably produce stable, highly p-doped ZnO which unfortunately is required for several of the above mentioned applications.

3.2 Properties of ZnO

3.2.1 Structural Properties

Most group II-VI binary compound semiconductors crystallize in either cubic, zinc blende or hexagonal wurtzite structure where each cation is surrounded by four anions at the corners of a tetrahedron, and vise versa. This tetrahedral coordination is typical of sp^3 covalent bonding nature. Under ambient conditions, the thermodynamically stable phase of ZnO is the wurtzite structure. While the zinc blende structure can only be stably grown on substrates with cubic crystal structures, and the rocksalt structure can only be obtained at relatively high pressures. The rocksalt structure occurs at relatively high pressures because the reduction of the lattice dimensions causes the interionic Coulomb interaction to favor the ionicity more over the covalent nature [19]. The hexagonal crystal family is described by a right rhombic prism unit cell with two equal axes (a by a), included angle (γ) equal to 120°and a height (c) which is perpendicular to the two base axes and typically of different length. The hexagonal structure has a 6 point group 6 mm (Hermann-Mauguin notation) or C_{6v} (Schoenflies notation), and the space group is $P6_3mc$ or C_{6v}^4. Fig. 3.1 shows the hexagonal crystal with the right rhombic prism unit cell in black. It also details the axes and angle (γ).

In ZnO, the room-temperature lattice constants determined by various experimental measurements and theoretical calculations for wurtzite ZnO are in good agreement. The lattice constants range from 3.2475 to 3.2501 Å for the axes length, a. The lattice constants for the height, c ranges from 5.2042 to 5.2075 Å [19]. The right rhombic prism unit cell contains two molecular units of

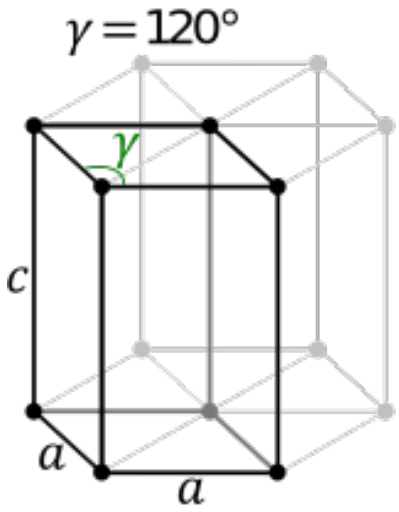

Figure 3.1: Hexagonal crystal with rhombic prism unit cell [20]

ZnO. The zinc atoms are surrounded by 4 oxygen atoms in a nearly tetrahedral configuration. The ZnO structure can also be visualized as a number of alternating planes composed of tetrahedrally coordinated 0^{2-} and Zn^{2+} ions stacked alternatively along the c-axis. This is illustrated in Fig. 3.2 The zinc atoms are represented in gray and oxygen atoms in yellow. The alternatively stacked tetrahedral configuration of coordinated 0^{2-} and Zn^{2+} ions is illustrated by the shaded areas.

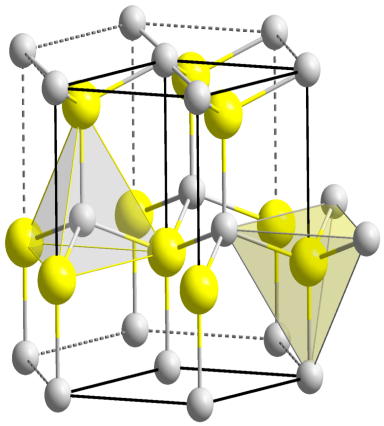

Figure 3.2: Zinc oxide wurtzite crystal structure [21]

The alternative stacking of the tetrahedral coordination results in non-central symmetry in the crystal. The bonding between zinc and oxygen is polar in nature due to the electronegativity difference of the two elements. These two properties of ZnO is what attributes to its piezoelectric

properties. The three coefficients of the piezoelectric tensor d_{15}, d_{31}, d_{33} are rather large, around -10, -5 and 12 x 10^{-12} m/V respectively [2].

The alternative stacking of the tetrahedral coordination also results in polar surfaces where the basal (0001) and (000$\bar{1}$) planes exhibit different bulk terminations with the (0001) terminated by positive Zn charges and the (000$\bar{1}$) terminated by negative O charges. As a consequence of these polar surfaces, ZnO shows normal dipole moment and spontaneous polarization along the c-axis [22]. In addition, the polar surfaces also result in a strongly anisotropic etching behavior. The O terminated surface is easily etched in slightly diluted acids (HCl, H_2SO_4, HN_3, H_3PO_4), while the zinc-terminated surface is quite resistant against these acids [23].

Wurtzite ZnO has three common types of fast growth directions <2$\bar{1}\bar{1}$0> (±[2$\bar{1}\bar{1}$0], ±[$\bar{1}$2$\bar{1}$0], ±[$\bar{1}\bar{1}$20]), <01$\bar{1}$0> (±[01$\bar{1}$0], ±[10$\bar{1}$0], ±[1$\bar{1}$00]) and ±[0001] [24]. Intrinsically, due to the higher energy of the (0001) crystal surface than other planes, ZnO crystals have a strong tendency to grow along the [0001] direction or the c-axis. However, by tuning growth rates along these directions, a wide range of morphologies with predominate crystal facets can be obtained. This is illustrated in Fig. 3.3.

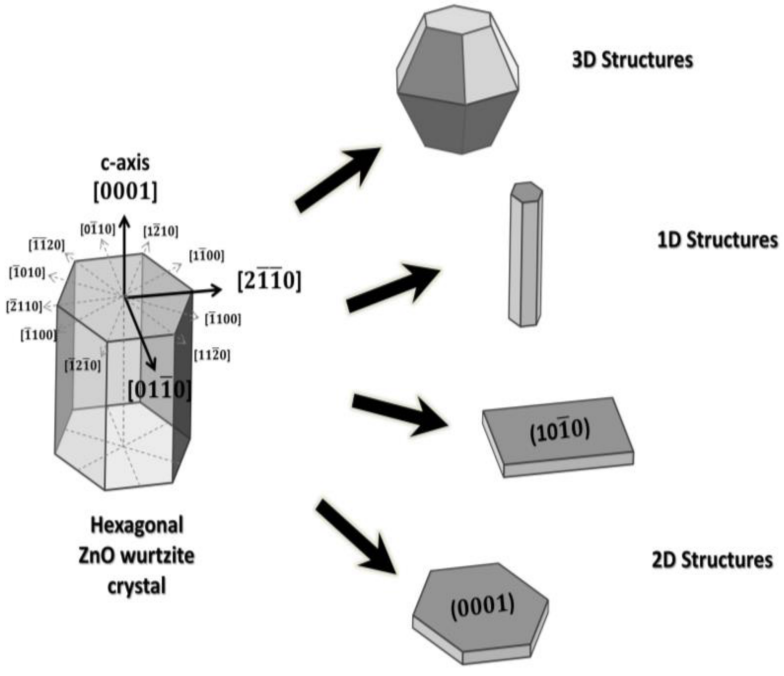

Figure 3.3: Preferential growth directions of ZnO wurtzite crystal and possible structures [25]

3.2.2 Electrical Properties

Electronic Band Structure

The electronic band structure or simply band structure of a given semiconductor is critical in determining its practicality. If the semiconductor in question is to be incorporated in a family of materials for device applications, then an accurate knowledge of the band structure is also pivotal. Theoretically, the band structure is obtained from solving Schrodinger's equation using crystal lattice parameters with numerous techniques of varying complexity and approximations. The band structure for wurtzite ZnO has been calculated previously using density-functional theory (DFT) [26, 27, 28, 29]. However, depending on the DFT method used, the calculated band gaps range significantly from 0.4 to 3.77 eV. In particular, local density (LDA) and generalized-gradient approximations (GGA) underestimate the band gap energy drastically [26, 29]. Despite their shortcomings in estimating the band gap, they are still in good agreement with experimental data. Fig. 3.4 shows the theoretical band structure from LDA by Vogel et al [26] and GGA by Erhart et al [29] calculations known as an *E-k* diagram. The x-axis represents the wave vector of an electron in an infinitely large, homogeneous material with several points of high symmetry called critical points in the Brillouin zone and are labeled accordingly for a hexagonal lattice system. The Brillouin zone is a unit cell in reciprocal space (Fourier transform of real space) and the reciprocal lattice is the Fourier transform of the Bravais lattice. For a hexagonal Bravais lattice with lattice constants c and a, the reciprocal lattice constants are $\frac{2\pi}{c}$ and $\frac{4\pi}{a\sqrt{3}}$ rotated 30^o about the c axis. Fig. 3.5 shows the Brillouin zone for a hexagonal lattice system and Table 3.1 provides a description of the critical points in a hexagonal lattice system. The y-axis in Fig. 3.4 is energy in eV and the solid lines are allowed states which an electron can occupy. The solid lines from 0 down to ∼-8.5 eV correspond to the valence bands and the lines from ∼3.4 eV upwards to 10 eV correspond to the conduction bands. The low lying valence bands (∼-8.5 eV) belong to Zn *3d* states, while the upper valence bands (∼-5 to 0 eV) correspond to O *2p* bonding states. The lowest conduction bands (∼3.4 eV) belong to Zn *3s* states.

The important details to takeaway from the band structure is the locations of both valence band maximum and conduction band minimum, the overall shape of the bands and what atomic orbitals correspond to the upper most valence bands and lowest most conduction bands. If both valence band maximum and conduction band minimum occur at the same critical point then the

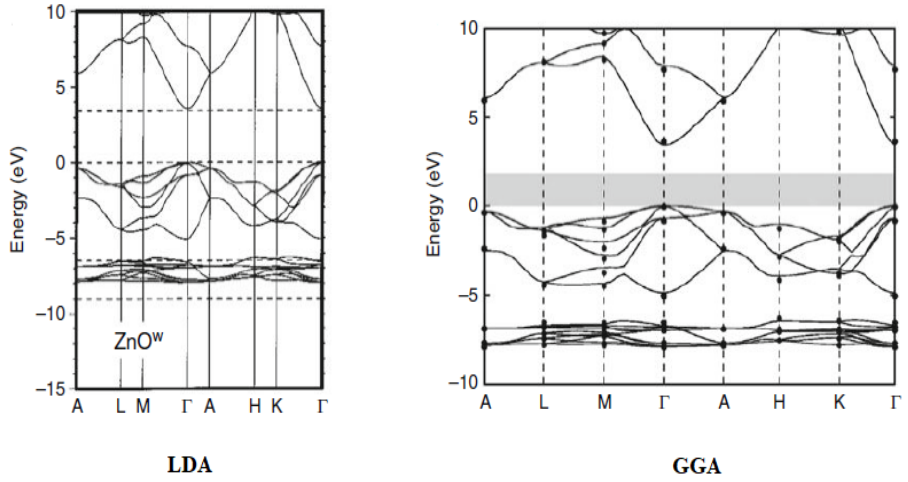

Figure 3.4: Band structure of wurtzite ZnO using local-density calculation of Vogel et al. [26] and generalized-gradient approximation calculation of Erhart et al. [29]

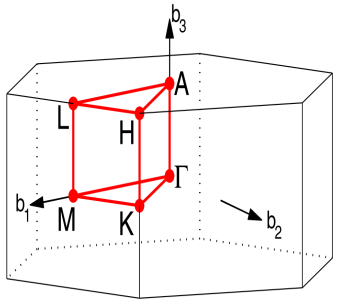

Figure 3.5: Brillouin zone for hexagonal lattice system [30]

Table 3.1: Critical points in hexagonal lattice system

Symbol	Description
Γ	Center of Brillouin zone
A	Center of a hexagonal face
H	Corner point
K	Middle of an edge joining a hexagonal and a rectangular face
M	Center of a rectangular face

semiconductor is a direct band gap semiconductor and a candidate for octoelectronic applications. The position of the conduction band minimum is also important for heterojunctions of ZnO with other semiconductors, for example, in thin film solar cells or light emitting diodes. The shape of the bands contain information regarding the effective mass of electrons and holes and by extension their mobility. A band with low dispersion, which appears more flat across the x-axis, indicates a

higher effective mass and therefore lower mobility compared to a band with high dispersion.

Intrinsic Defects and Doping

It was found by Fritsch in 1935 by Hall and Seebeck measurements that intrinsic (undoped) ZnO is an n-type semiconductor [31]. While the electrical properties of intrinsic ZnO have been investigated for many decades, it wasn't clear until recently, which defect(s) constitute(s) the dominant donor(s) in intrinsic ZnO [32]. Intrinsic point defects are deviations from the ideal structure caused by displacement or removal of lattice atoms. Possible intrinsic defects are vacancies, interstitials, and antisites. As a rule of thumb, the energy required (formation energy) to create a intrinsic defect depends on the difference in charge between the defect and the lattice site occupied by the defect. For example, in ZnO a vacancy or interstitial can carry a charge of ± 2 while an antisite can have a charge of ± 4. This makes vacancies and interstitials more likely in polar compounds and antisite defects less important [33, 34, 35]. However, antisite defects are more important in more covalently bonded compounds like the III-V semiconductors such as GaAs [36]. It is important to note that the formation energy of intrinsic defects is dependent on the chemical potential and the Fermi level position in the band gap [37]. The chemical potential corresponds to the concentration of species, which for gases, is related to its partial pressure. For instance, increasing partial pressure of oxygen leads to a decreased formation energy for defect reactions which either add a oxygen (interstitial) or remove a zinc (vacancy) and vice versa. For charged defects, the formation energy depends directly on the Fermi energy, which is the chemical potential of the electrons (and holes). A donor type defect can be neutral or positively charged depending on its occupation, which is given by the Fermi level position with respect to the defect energy level position. If the Fermi level is above the defect energy level, then the electron resides at the donors defect energy level and is neutral. If, however, the Fermi level is below the defect energy level, then the electron from the donor is transferred to its reservoir whose energy is represented by the Fermi energy. Thus the donor energy level is unoccupied resulting in a positively charged donor defect type. It is important to keep this in mind when discussing electrical transport and is represented schematically in Fig.3.6.

Notice in the plot on the right in Fig.3.6 that the formation energy of intrinsic acceptor defect types decreases with increase in Fermi energy. Generally, donor defects lead to a rise of

the Fermi energy and therefore a lowering of the formation energy of intrinsic acceptor defect types, e.g., zinc vacancies. This mechanism leads to a limitation of the movement of the Fermi level and is called self-compensation [38]. This is well known for many semiconductors and leads to a limitation of the doping. This limitation in doping, in the case of ZnO, is important in two aspects. First is the possibility for p-type doping. Second, and more important is the possibility for degenerate n-type doping. The upper limitation for the Fermi level position must be well above the conduction band minimum in order to achieve a degenerate n-type semiconductor and is a prerequisite for materials to be used as transparent conducting electrodes.

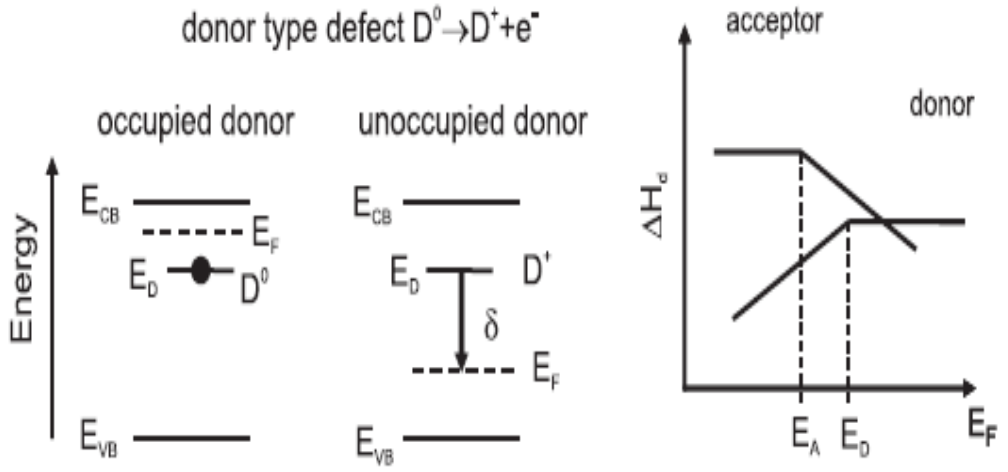

Figure 3.6: Dependence of defect formation energy (ΔH_d) on Fermi energy. δ represents the energy gain when an electron is transferred to its reservoir. E_D, E_CB and E_VB represent donor, conduction band and valence band energy levels respectively [39]

Historically, it was believed that oxygen vacancies were the dominant intrinsic donor type defect, which was supported by experiments showing that annealing a single crystal or thin film under reducing conditions increases carrier concentration, while an oxidizing treatment decreases carrier concentration. It wasn't until experiments conducted in 1998 by Look et al. found that zinc interstitials are the intrinsic shallow donors. Look et al. performed an electrical transport study on pure, intrinsic ZnO singe crystals and generated crystallographic defects using high-energy (MeV) electron irradiation and found defect production to be higher when irradiating the crystal in (001) direction (Zn-face up) compared to irradiating along the (00-1) direction (O-face up) [40]. Erhart et al. [29, 41, 42] performed comprehensive DFT calculations of defect formation energies and diffusion constants in ZnO which support the results of Look et al. These authors concluded

that zinc vacancies and oxygen interstitals act as acceptors, and only zinc interstitials and oxygen vacancies have shallow energetic donor positions in the band gap of ZnO. A shallow donor being defined as one which the defect energy level is no more than $3k_bT$ (0.075 eV at 300K) below the conduction band minimum. However, due to the high formation energy, zinc interstitials are less likely formed compared to oxygen vacancies and thus oxygen vacancies are in fact the dominant intrinsic donor defect [43].

In addition to zinc interstitial and oxygen vacancies, hydrogen has also been found to act as a shallow donor in ZnO. Reports of the doping effect of hydrogen date back to 1950s [44, 45] with support from DFT studies by van de Walle in 2000 [46]. This is an important fact, since hydrogen is present during almost all growth processes, introducing a background doping in both single crystals and thin films. Depending on the growth process, the concentration of hydrogen in ZnO can vary between 5 x 10^{16} cm^{-3} and 1 x 10^{20} cm^{-3} for single crystals grown by chemical transport and ZnO:Al films produced by magnetron sputtering respectively [47]. However, it should be noted that by definition, hydrogen is not an intrinsic defect donor but does act as a shallow donor like zinc interstitials and oxygen vacancies.

Intrinsic donor defects, specifically, zinc interstitials and oxygen vacancies is just one of the ways to achieve low resistivity at room temperatures, i.e., a degenerate semiconductor. The second, is the introduction of extrinsic dopants, either by substituting metals with oxidation number three on Zn metal lattice sites or substituting halogens with oxidation number minus one on oxygen lattice sites. Group III dopants (B, Al, Ga, In) are the most widely used dopants with a comprehensive investigation on ZnO thin films performed by Minami et al [48].

Electrical Transport in ZnO Thin Films

ZnO thin films are polycrystalline in nature, meaning, they are composed of many crystallites of varying size and orientation. These polycrystalline films exhibit a vast amount of grain boundaries, which compose crystallographically disturbed regions and lead to electronic defects (traps) in the band gap of ZnO. These defects are also charged by carriers from the interior of the grains, so depending on the type of carriers (electrons or holes) and the type of defect (electron trap or hole trap) depletion or accumulation zones are formed around the grain barrier due charge balance. In ZnO, which is typically n-type, a depletion zone is generated on both sides of a grain

barrier accompanied by an energetic barrier of height Φ_b for the electrons due to the electron trap character of the defects at the grain boundary. According to Seto [49], who was the first to comprehensively describe carrier transport in polycrystalline silicon, carrier transport across a grain barrier can occur either by thermionic emission or quantum-mechanical tunneling through the barrier if sufficiently high carrier concentrations exist. This is illustrated in Fig.3.7 where carrier transport via thermionic emission and quantum-mechanical tunneling are indicated by TE and T respectively. The red lines represent charge carrier traps and the grain barrier is labeled Φ_b.

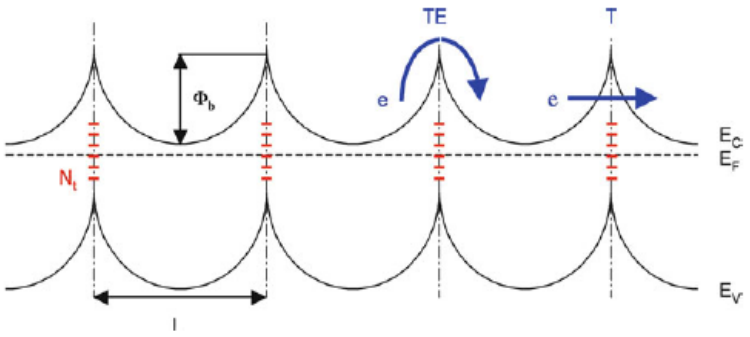

Figure 3.7: Carrier transport across a linear row of grain barriers seperated by distance l [50]

3.2.3 Optical Properties

Optical Properties and Processes in Semiconductors

The main optical properties of a semiconductor are typically its refractive index n and its extinction coefficient K or absorption coefficient α. The refractive index is the ratio of the velocity of light c in vacuum to its velocity v in the medium given in Eq.(3.1). In combination with Maxwell's equations, the well-known formula for refractive index of a material is obtained as given in Eq.(3.2). Where ε_r is the relative permittivity and μ_r is the magnetic permeability. Since μ_r is equal to 1 for nonmagnetic materials, Eq.(3.2) can be simplified to $n = \sqrt{\varepsilon_r}$. ε_r is wavelength dependent, thus the refractive index depends on the wavelength of light as well and is known as dispersion. In addition to dispersion, electromagnetic radiation propagating through a lossy medium experiences attenuation due to various loss mechanisms such as lattice vibrations (phonons), photogeneration, free carrier absorption and scattering. In such a case, the refractive index is a complex function of the frequency of electromagnetic radiation propagating through the material given in Eq.(3.3). Where n indicates phase velocity and K represents attenuation.

$$n = \frac{c}{v} \tag{3.1}$$

$$n = \sqrt{\varepsilon_r \mu_r} \tag{3.2}$$

$$N = n - iK \tag{3.3}$$

In semiconductors, the optical properties originate from both intrinsic and extrinsic effects. Intrinsic optical transitions occur between electrons in the conduction band and holes in the valence band, including excitonic effects due to Coulomb interaction. Extrinsic effects are related to dopants/impurities or point defects and complexes, which typically create electronic states in the bandgap and therefore influence both optical absorption and emission processes. Fig. 3.8 shows a typical relationship between the absorption coefficient and incident photon energy for a crystalline semiconductor, illustrating the various possible absorption processes labeled accordingly. Free carrier absorption is due to the presence of free electrons and holes as described in 2.3. Recall, that an electromagnetic wave with sufficiently low frequency oscillation can interact with free carriers in a material and thereby drift the carrriers. This interaction results in energy loss from the electromagnetic wave due to lattice vibrations through the carrier scattering process. If the semiconductor is doped, a narrow absorption peak will be present due to doping and other impurities that may be present in the material. Lattice absorption or reststrahlen is radiation that is absorbed by vibrations of crystal ions. At these energies, ionic crystals reflect and absorb light strongly due to resonance interaction between the electromagnetic wave and transverse optical phonons. Exciton absorption which typically occurs at low temperature, occurs when a photon excites an electron, creating an electron-hole pair. They are bound together through their attractive Coulomb interaction and the absorbed optical energy remains held within the solid for the lifetime of the exciton. Lastly, the band-to-band or fundamental absorption of photons which excites an electron from the valence to the conduction band. Fundamental absorption occurs when the energy of incident photons are equal or greater than the band gap energy E_g. It has a large absorption coefficient and is probably the most important absorption effect. The value of the energy band gap, and its temperature shift, dE_g/dT, are important factors

in semiconductor-based optoelectronic devices [51]. It is worth mentioning, that in nearly all semiconductors the energy band gap decreases with temperature, hence shifting the fundamental absorption to longer wavelengths.

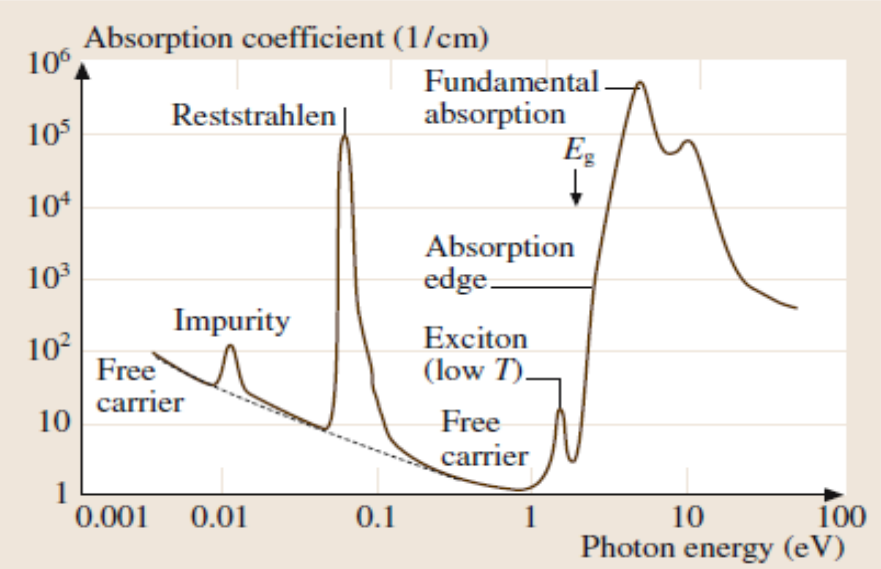

Figure 3.8: Relationship between absorption coefficient and incident photon energy for a crystalline semiconductor with various absorption processes labeled [51]

Direct and indirect transitions are the two types of band-to-band transitions. A direct transition does not involve any phonons. When a photon is absorbed, an electron is excited from the valence to conduction band without a change in the electrons momentum due to the photon momentum being negligible compared to the electron momentum. On an E-k diagram, this is a vertical transition from the conduction band to the valence band and can only occur if the global extrema of the upmost valence and lowest conduction are at the same point in the Brillouin zone, namely at $\boldsymbol{k} = 0$, i.e. at the Γ-point. When the electron returns back to a lower energy in the valence band, a photon is emitted with energy equal to the difference in energies of the energy levels which the electron has transitioned between. This emission process occurs without any phonons involved. However, it should be mentioned that if the electron is excited higher into the conduction band, energy is transferred in the form of phonons while the electron relaxes to the lowest conduction energy level or state. Semiconductors which exhibit this absorption and emission behavior are known as direct band gap semiconductors and can be used in semiconductor-based optoelectronic devices. Unlike direct transitions which don't involve

any phonons, indirect transitions require the absorption and emission of phonons during the absorption process. Despite the involvement of phonons, some indirect band gap semiconductors such as GaP, recombination of a electron with a hole can result in photon emission at certain recombination centers. These recombination centers are generated by the purposeful addition of nitrogen impurities to GaP. Fig.3.9 illustrates the two band-to-band transitions that occur during absorption and Fig.3.10 illustrates the possible transitions that occur when the excited electron returns to the valence band.

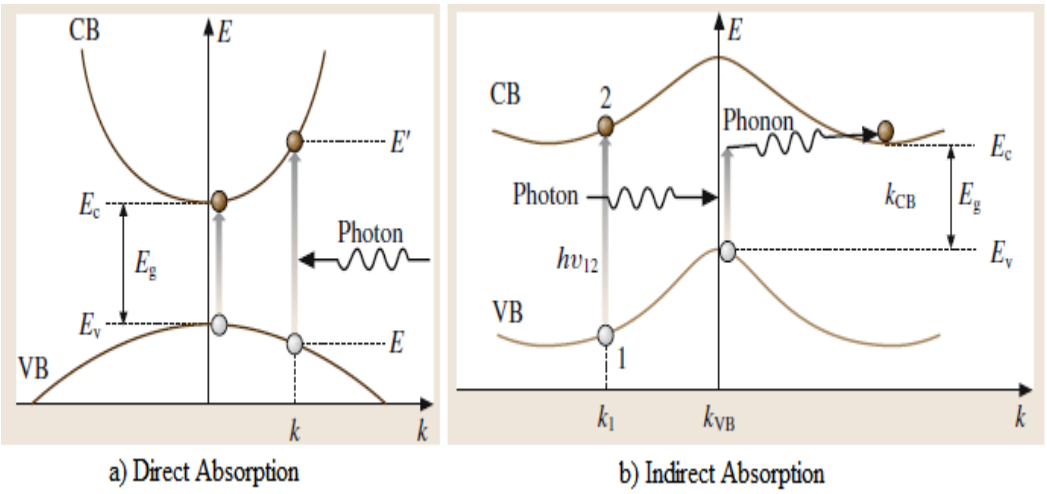

Figure 3.9: Band-to-band absorption [51]

Optical Properties of ZnO

The optical properties of zinc oxide which have renewed interest in optoelectronic applications are due to its direct wide bandgap of 3.37 eV at room temperature [53], large exciton binding energy of 60 meV [54, 55], and efficient radiative recombination. Most notably, the large exciton binding energy paves the way for intense near-band-edge excitonic emission at room temperature and even higher temperatures, because it is 2.4 times the room-temperature thermal energy ($k_BT = 25meV$). This allows for laser operation at room temperatures based on excitonic transitions, as opposed to electron-hole plasma, with several groups already demonstrating optically pumped lasing at room temperature [56, 57, 58, 59, 60]

As already mentioned previously, ZnO is a direct wide-band gap semiconductor with a band gap energy of 3.44 eV at low temperatures and 3.37 eV at room temperature [53]. This property

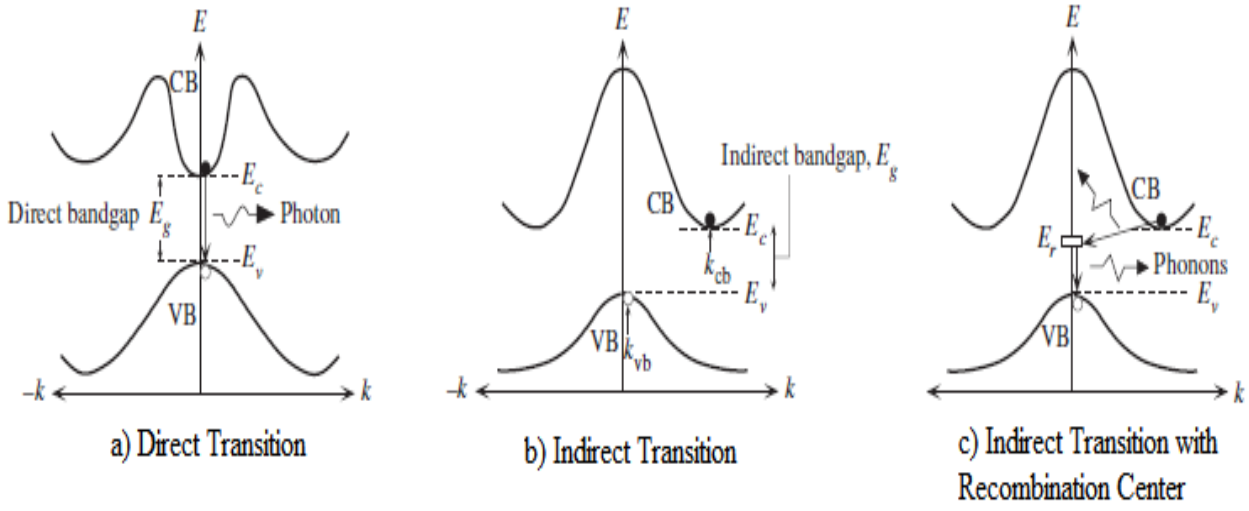

Figure 3.10: Band-to-band emission [52]

allows ZnO to be used for optoelectronic applications such as light emitting diodes and laser diodes. The wide band gap (>3 eV) means ZnO is transparent in the visible spectrum and can be used for blue/UV optoelectronics. Other advantages associated with a large bandgap include high-temperature and high-power operation, lower noise generation, higher breakdown voltages and ability to sustain large electric fields [61]

ZnO also often exhibits green luminescence. The origin of the green luminescence has been a topic of debate with claims that impurity Cu^{2+} ions [62, 63], zinc vacancies [33, 64], oxygen vacancies [65], interstitial zinc ions [66], oxygen antisites [67] and transitions from interstitial zinc ions to zinc vacancies [2] are the cause of the green luminescence. Subsequent experiments showed that there is no correlation between the concentration of copper ions and green luminous intensity but instead revealed that the green luminescence is related to intrinsic zinc vacancy defects [65]. Interstitial zinc ions (shallow donor) and oxygen anitisites can be disregarded due to the high formation energy of such intrinsic defects [68]. Based on results from Kohan et al. [33], and supporting work by Reynolds et al. [69], it can be concluded that the contributors to green luminescence are transitions from shallow donor oxygen vacancies to deep acceptor zinc vacancies.

3.3 Applications of ZnO

3.3.1 Overview

Due to its diverse chemical and physical properties, zinc oxide is widely used in many industries. From the rubber industry to improve the thermal conductivity of typical pure silicone rubber and produce vulcanizates with high tensile strength, tear resistance, hardness and hysteresis [70]. To the pharaceutical and cosmetic industry where it is widely used in the production of various kinds of medicines due to its antibacterial, disinfecting and drying properties [71, 72]. It is used in the textile industry for UV-protective textiles. However, the widest range of applications is in the electronics industry, where its optical and electrical properties allow it to be utilized in various optoelectronic devices including green phosphors [73], light-emitting diodes [74], photodiodes [75], and UV-lasers [76]. Its piezoelectric properties allow it to be used in surface-acoustic wave devices and sensors [77].

3.3.2 Transparent Conducting Oxides and Thin Film Transistors

ZnO is best used in TCO applications where high transparency, resistance to H plasma, and etching is required. Indium tin oxide has been the dominate material used for transparent electrodes. However, highly-doped ZnO has been used as an alternative in some applications due to the relatively high cost of indium. Thin films solar cells require a transparent electrode for light transmission while providing electrical access for extraction of the photocurrent. In display technologies such as liquid crystal displays, transparent electrodes are used to apply an electric field for reorientation of the liquid crystals while still allowing the transmission of light. In both examples, highly-doped ZnO has been used as an alternative to indium tin oxide. ZnO doped with fluorine also makes an excellent ohmic contact to n-Si due to its low work function.

Thin film transistors (TFTs) technology has been dominated by amorphous Si (a-Si) and polycrystalline Si (poly-Si). However, a growing interest for an optically transparent analog, the transparent thin film transistor (TTFT) to be used in a wide range of commercial and military applications where transparency is required has resulted in numerous research groups to explore devices based on ZnO. The transparent nature of ZnO, potential achievement of low-cost polycrystalline ZnO suggest that ZnO may find a niche application in transparent thin film technologies.

3.3.3 Gas Sensors

ZnO nanostructures have been extensively studied for gas sensing applications. A gas sensor converts chemical information (concentration) of a particular gas present in the surrounding into an electrical or optical signal. The device functions by firstly recognizing a particular gas through adsorption, reduction or electrochemical reactions to/by sensor materials or electrode (receptors) then transduction of that information in the form of signals. The interaction between gas and sensor can be any physical or chemical effect on or around the receptors, such as reaction product, adsorbed formations, generation of heat of reactions, changes in receptors mass, dimensions, surface/bulk properties and changes in the electrode potentials [78].

In the case of semiconductors, the changes in the work function and work function dependent resistance are monitored. The surface conductivity of ZnO is recorded in response to the adsorbed gas. The ZnO surface exhibits point defects, which affect the conductivity of ZnO. Oxygen vacancies are dominant defects in ZnO films generated by annealing at high temperature. The resistance of ZnO-based sensors is monitored, which correspond to the adsorption and desorption of gas molecule on the sensors surface [79]. Oxygen from the air is adsorbed on the surface of ZnO, converting the oxygen into oxygen ions by taking electrons from the conduction band. This results in less charge carrier species, subsequently increasing resistance. If for example, ammonia molecules were to react with O_2 on the surface, electrons will flow back into the conduction band consequently reducing resistance. The reaction with oxygen and ammonia is given by Eq.(3.4). The gas sensing properties of ZnO depend on surface area, porosity, defect concentration, and working temperature [79]. ZnO has also been widely used for detecting other gases such as H_2, NH_3, CH_4, CO, NO_2, ethanol and acetone [80, 81, 82, 83, 84].

$$2\,NH_3(g) + 7\,O^- \longrightarrow 2\,NO_2(g) + 3\,H_2O\,(g) + 7\,e^- \tag{3.4}$$

3.4 Preparation Methods of Thin Film ZnO

Most of the current applications of ZnO, such as transparent conductive electrodes for solar cells, piezoelectric devices, gas sensors and varistors utilize polycrystalline films grown on glass substrates. This is achieved by various deposition techniques including chemical spray pyrolysis,

screen painting, electrochemical deposition, sol-gel and oxidation of Zn films. These techniques are appealing due to their ability for relatively low temperature and large area deposition. However, are not applicable for electronic and optoelectronic applications, where high-quality single-crystal epitaxial films with minimal concentrations of native defects and controlled incorporation of impurities is required. For such requirements, other deposition methods including pulsed laser deposition, chemical vapor deposition, metal-organic chemical vapor deposition and molecular-beam epitaxy are utilized.

ZnO has been grown on numerous non-native substrates including sapphire, GaAs, CaF_2, $ScAlMgO_4$, Si, GaN and glass [85]. Heterostructures are often used to fabricate devices such as light emitting diodes. Due to the difficulty in obtaining p-type ZnO, typically the substrates just mentioned are used as the p-type material. Physical vapor deposition and solution-based processes are the two methods that can be utilized to achieve the desired oxide thin film.

3.4.1 Physical Vapor Deposition

Physical vapor deposition (PVD) is a coating process and an umbrella term used to describe a variety of methods to deposit thin films via the condensation of a vaporized form of a solid material onto various substrates [86]. PVD techniques can be further broken down into evaporative or sputtering. Evaporative techniques typically heat a target material in the presence of a vacuum and inert gas. The target material vaporizes and is deposited on the substrate in the form of a thin film.

In sputtering processes, desired atoms are removed from a target material using a high-energy ion source in the presence of a vacuum and inert gas. Once vaporized, the atoms move toward the surface of the substrate and are deposited in the form of a thin layer. There are many types of PVD methods including: chemical vapor deposition, metal-organic chemical vapor deposition, molecular-beam epitaxy and magnetron sputtering. These processes yield higher quality thin films compared to solution-based processes and are employed in areas where such criteria is required such as for optoelectronic devices. However, these processes are costly, requiring vacuum systems in order to operate.

3.4.2 Solution-Based Processes

Solution-based routes start with a precursor which is the chemical reagent containing the cation of interest and reacts to form the desired material and phase. Precursor selection is

based on solvent being used, formulation and desired processing route. Solution routes to TCOs typically use acetates, chlorides, or nitrates as precursors because of their low cost and availability from commercial suppliers. Another option is metal-organic compounds as their solubility in polar or non-polar solvents can by adjusted with choice of organic substituent. Other precursors used include: carboxylates, β-Diketonates, homometallic alkoxides, oxo-alkoxides, heterometallic alkoxides and organometallics [87].

Once a precursor is selected, a coating solution is formulated by addition of a solvent and other additives. Metal-organic deposition (MOD) solutions and nanoparticle suspensions are the two main types of coating solutions that can be formulated. Each having their own advantages and disadvantages. Nanoparticle suspensions have the benefit of not requiring excessive thermal processing temperatures since the material of interest has already been pre-synthesized. However, it typically requires the use of a stabilizer which needs to be removed during sintering and depending on the deposition method used, the particles may clog nozzles in certain printing methods. In the case of MOD based solutions, preparation is typically more straight forward compared to nanoparticle suspensions. However, additional thermal processing is required to drive off organics or counter-ions in order to yield the oxide phase.

Regardless of the choice in solution formulation, solution-based routes are appealing because they allows for deposition at atmospheric pressure with minimal equipment cost. It can also be scaled to allow for uniform, large-area coverage. Coating techniques can be classified into two categories: direct growth of material on the substrate during deposition or liquid coating that requires additional processing to remove solvent and yield the desired oxide phase. Direct growth methods include electrochemical and electroless chemical bath deposition (CBD). These methods rely on the controlled reaction and precipitation of reagents in solution. Nucleation and subsequent film growth occurs on the surface of the substrate immersed in the solution bath. Liquid coating techniques include spin-coating, dip-coating, spray-coating and various printing techniques such as screen printing and inkjet printing. Liquid coatings are more common for creating TCOs compared to direct growth methods despite their sensitivity to the characteristics of the solution formulation. Fig. 3.11 illustrates the various solution-based deposition methods.

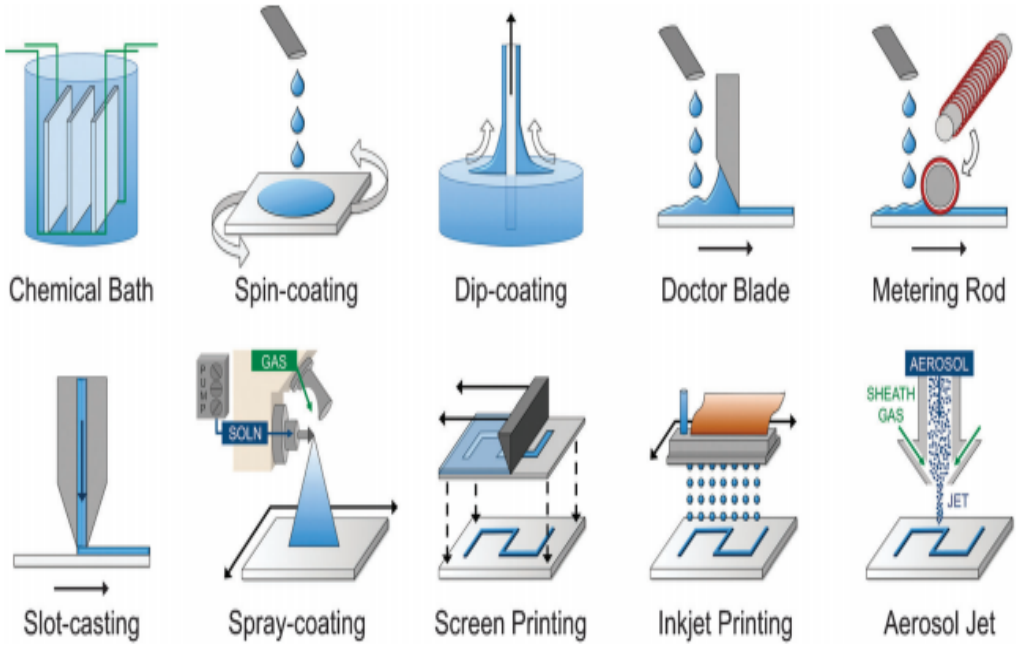

Figure 3.11: Various solution deposition methods [87]

Chapter 4

Sol-Gel Chemistry

4.1 Introduction

Sol-gel chemistry is the preparation of inorganic polymers or ceramics from solution through a transformation from liquid precursors to a colloidal suspension called a 'sol' and finally a network structure called a 'gel' [88]. Initially the term 'sol-gel' was used to describe hydrolysis and condensation processes. However, more recently, sol-gel has been broadly defined as covering the synthesis of solid materials from solution-state precursors. These include metal alkoxides that cross link to form metal-oxane gels, metal ion-chelate complexes or organic polymer gels[89].

Sol-gel processes are useful for producing ZnO thin films in a simple, cost-effective and highly controlled manner. Two sol-gel routes are commonly used which depend on the nature of the molecular precursors: metal alkoxides in organic solvents or metal salts in aqueous solutions [90]. The method used in this thesis is a combination of the two conventional sol-gel routes using a organic metal salt in an alcoholic solvent. This method was first introduced by Spanhel and Anderson in 1991 using ZAD and ethanol [91]. From a chemistry standpoint, the formation of the ZnO films is the result of a complex sequence of interconnected reactions that are at the basis of two fundamental steps regulating the entire sol-gel process, namely hydrolysis of the metal salt precursor and subsequent condensation to form the ZnO network [90, 92].

The solution is then deposited onto a substrate using numerous solution-based deposition techniques. As discussed in 3.4.2, these techniques allow for deposition of films at atmospheric pressure with minimal equipment cost. Techniques include: chemical bath, spin-coating, dip-coating, doctor blade, slot-casting, spray-coating, screen printing, inkjet printing and aerosol

jet. Coating techniques can be classified into two categories: direct growth of the material on the substrate during deposition or liquid coating that requires additional processing to remove solvent and yield the desired phase [87]. Transparent conductors are most commonly deposited by liquid coating methods. Dip-coating is the technique adopted in this thesis which involves the entrainment of a solution layer on a substrate as it is withdrawn from a solution reservoir.

Following deposition, the film undergoes a heat treatment referred to as pre-heat treatment prior to further deposition. During the pre-heating step, evaporation of the solvent and decomposition of organic residues in the film occur leading to what is referred to as a dry-gel or xerogel. Repetition of film deposition and pre-heating is carried out until the desired thickness is achieved. After that, the xerogel undergoes a higher temperature heat treatment, referred to as post-heat treatment, in which the deposited ZnO clusters undergo sintering to produce the final dense ZnO thin film. The entire process is illustrated in Fig. 4.1.

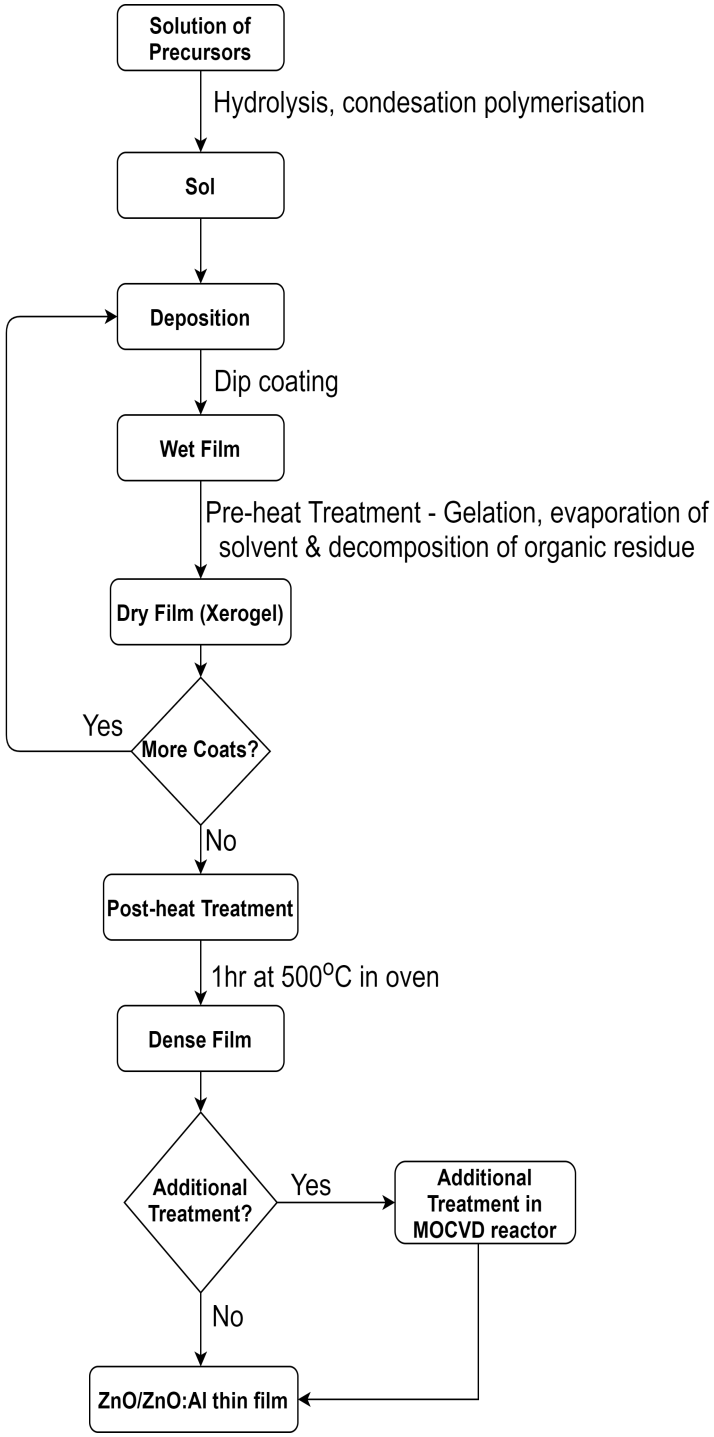

Figure 4.1: Flowchart summarizing ZnO thin film synthesis via sol-gel

4.2 Solution Preparation

The sol-gel process begins with obtaining a colloidal suspension, referred to as the sol, prepared with an appropriate molecular precursor. Typical precursors include hydrated organic zinc salts such as zinc acetate dihydrate (ZAD) or inorganic zinc salts such as zinc nitrate or zinc perchlorate. The metal salt is dissolved in appropriate solvents such as methanol, ethanol, 1-propanol, and 2-methoxyethanol (2-ME). This is typically done in the presence of a chelating and stabilizing ligand such as monoethanolamine (MEA), diethanolamine (DEA), triethanolamine (TEA), triethylamine (TeA) or ethylenediamine (EDA).

The choice of zinc source, solvent and stabilizer for the work presented in this thesis is zinc acetate dihydrate, 1-Butanol, and monoethanolamine respectively. Reasoning for this choice in zinc source, solvent and stabilizer, as well as their role in solution preparation and effect on final thin film properties is provided in 4.2.1, 4.2.2 and 4.2.3 respectively.

In the work presented in this thesis, solution preparation begins by adding MEA to 1-Butanol. Next, ZAD and the respective aluminum source, either AlCl, $Al(NO_3)_3$ or $Al_2(SO_4)_3$, which have been mixed together prior, are added to the mixture of MEA and 1-butanol. The concentration of ZAD was 0.75 mol/L, molar ratio of MEA to ZAD was [MEA/ZAD] = 2 and the molar ratio of Al-source to Zn, [Al^{3+}/Zn2+] was either 0.5 or 1%. The solution was heated on a hotplate at 60°C and stirred vigorously for 1 hr to obtain a translucent sol. The transparency of prepared sols depends on the size of solid phase particles in the colloidal solution which in turn is dependent upon type and rate of reactions which could be varied by changing concentrations of zinc source and additive also known as the stabilizer. As well as changing the type of zinc source and stabilizer. The flowchart for solution preparation is illustrated in Fig. 4.2.

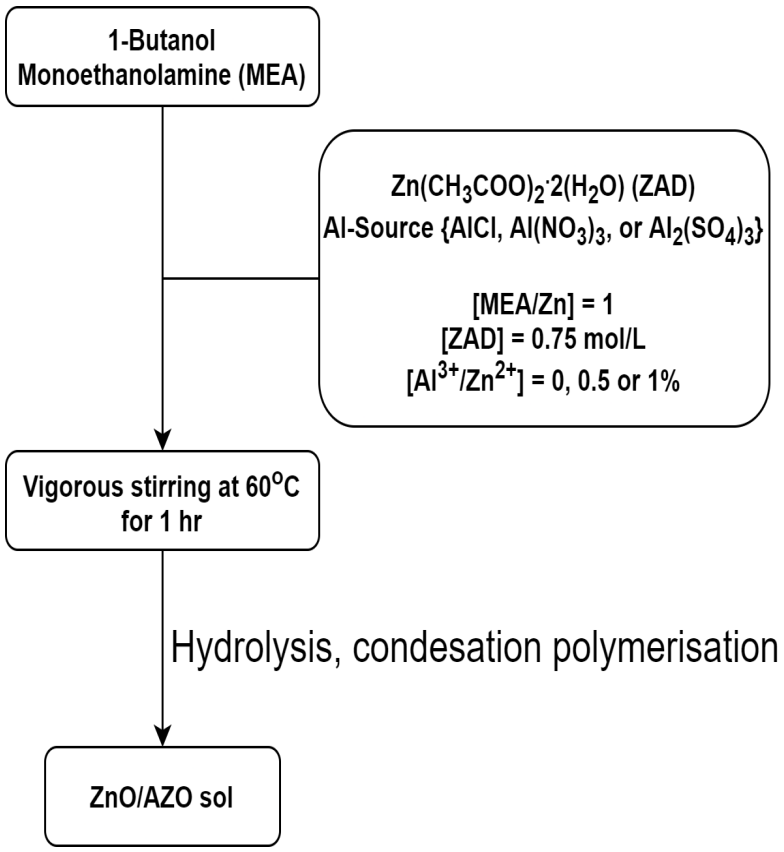

Figure 4.2: Solution preparation flowchart

Establishment of Initial Sol

As mentioned in 4.1, two fundamental steps regulate the entire sol-gel process, namely hydrolysis of the metal salt precursor and subsequent condensation to form the ZnO network. In work presented in this thesis (alcohol solvent, $[H_2O]/[Zn^{2+}]=2$), hydrolysis and condensation of Zn(II) cation are relatively slow, due to the low quantities of water. When ZAD is dissolved in an alcohol, an equilibrium exists between its corresponding ions and the solvated salt, which can be represented by:

$$Zn(CH_3CO_2)_{2(solv)} \rightleftharpoons Zn^{2+}_{(solv)} + 2\,CH_3COO^-_{(solv)} \tag{4.1}$$

Due to presence of water from the di-hydrated salt, acetate anions are in equlibrium with

acetic acid according to:

$$CH_3COO^-_{(solv)} + H_2O \rightleftharpoons CH_3COOH_{(solv)} + OH^-_{(solv)} \tag{4.2}$$

This reaction is the result of the partial dissociation of zinc acetate and the presence of water in the alcohol. Since acetic acid is a weak acid, the equilibrium is shifted toward the products, producing the necessary quantity of hydroxyl anions. The resulting equilibrium comprises the source of OH^- anions for nucleophilic attack that initiates the precursor formation previous to condensation according to:

$$--Zn--_{(solv)} + OH^-_{(solv)} \rightleftharpoons --Zn{-}OH]_{(solv)} \tag{4.3}$$

–Zn–, denotes molecular species of unknown composition, which form upon dissolution of ZAD.

In addition to the nucleophilic OH^- anions, two other nucleophilic species exist in the solution that compete for the Zn^{2+} Lewis acid center. They are the carboxylic anion, CH_3COO^- and the stabilizer, MEA, which contains both an alcohol, -OH and amine, $-NH_2$. This results in a dynamic equilibrium in the solution which can be seen in Fig. 4.3

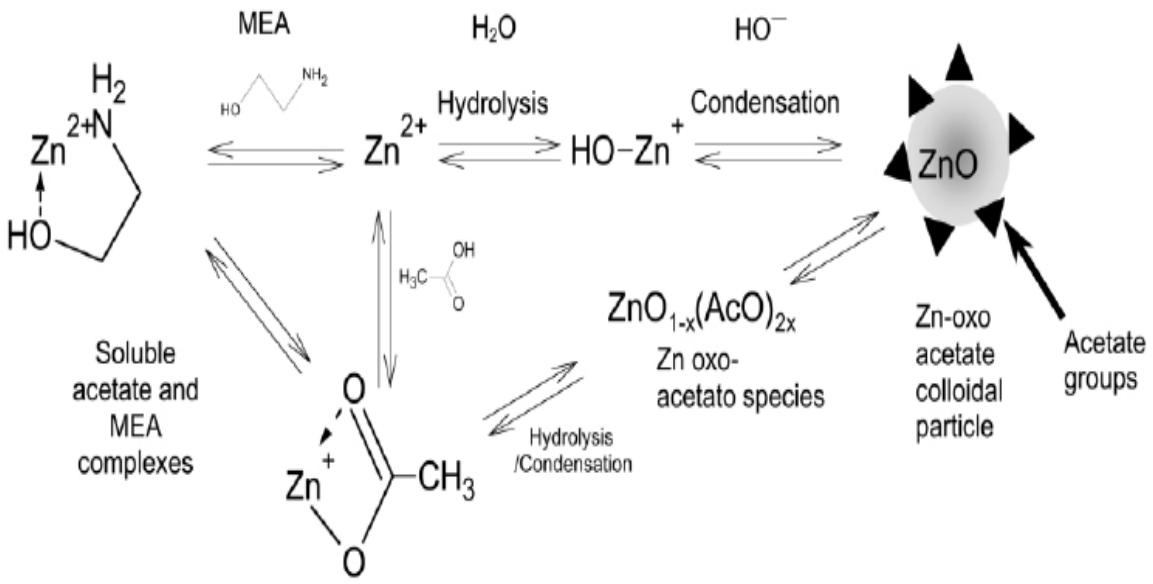

Figure 4.3: Chemical equilibria in initial solution [93]

These nucleophilic species (MEA, OH^-, and CH_3COO^-) compete for the Zn^{2+} Lewis acid center. Attack of an OH^- leads to the formation of small zinc-oxo-acetate oligomers, which are expected to be formed in the initial stage [91], from gradual forced hydrolysis of Zn-MEA or Zn-AcO soluble complexes during vigorous stirring at elevated temperatures, commonly referred to as aging. The progessive condensation of the hydrolyzed moieties gives rise to colloids consisting of stable acetate-capped colloidal nanometric to sub-micronic particles. The condensation processes may occur by the possible mechanism:

$$--\mathrm{Zn}-\mathrm{OH}]_{(\mathrm{solv})} + \mathrm{OH}^-_{(\mathrm{solv})} \longrightarrow --\mathrm{Zn}-\mathrm{O} + \mathrm{H_2O}$$

and/or

$$--\mathrm{Zn}-\mathrm{OH}]_{(\mathrm{solv})} + --\mathrm{Zn}-\mathrm{OH_2}]_{(\mathrm{solv})} \longrightarrow --\mathrm{Zn}-\mathrm{OH}-\mathrm{Zn}-- + \mathrm{H_2O}$$

Spanhel and Anderson [91] and Briois et al [94] proved two complexes form in sols, sheet-like zinc hydroxy double salt (Zn-HDS) and pyramidal zinc-oxy-acetate (basic zinc acetate). Zn-HDS is composed up piled-up Brucite layers with acetate anions and H_2O molecules intercalated between layers for sake of charge balance. Zinc oxy-acetate is a 3-dimensional fractal structure

known as Sierpinski pyramid formed of $[Zn_4O]^{6+}$. Zinc oxy-acetate can readily convert to Zn-HDS in certain conditions concerning water content in sol such as pH level and additives which affect potential of water in the sol. Both complexes exist in sols to varying degrees and are illustrated in Fig. 4.4

Conversion to Zn- HDS has impact on crystalline structure. Zinc oxy-acetate tetrahedra are constructive components of ZnO wurtzite easiliy forming high-aspect-ratio crystals with wurtzite structure. While Zn-HDS results in layered structure that takes more energy to rearrange to form wurtzite structure resulting in lower aspect ratio. Therefore, it is crucial to control water content and hydrolysis rate by controlling pH level and additives to achieve desirable crystalline structure.

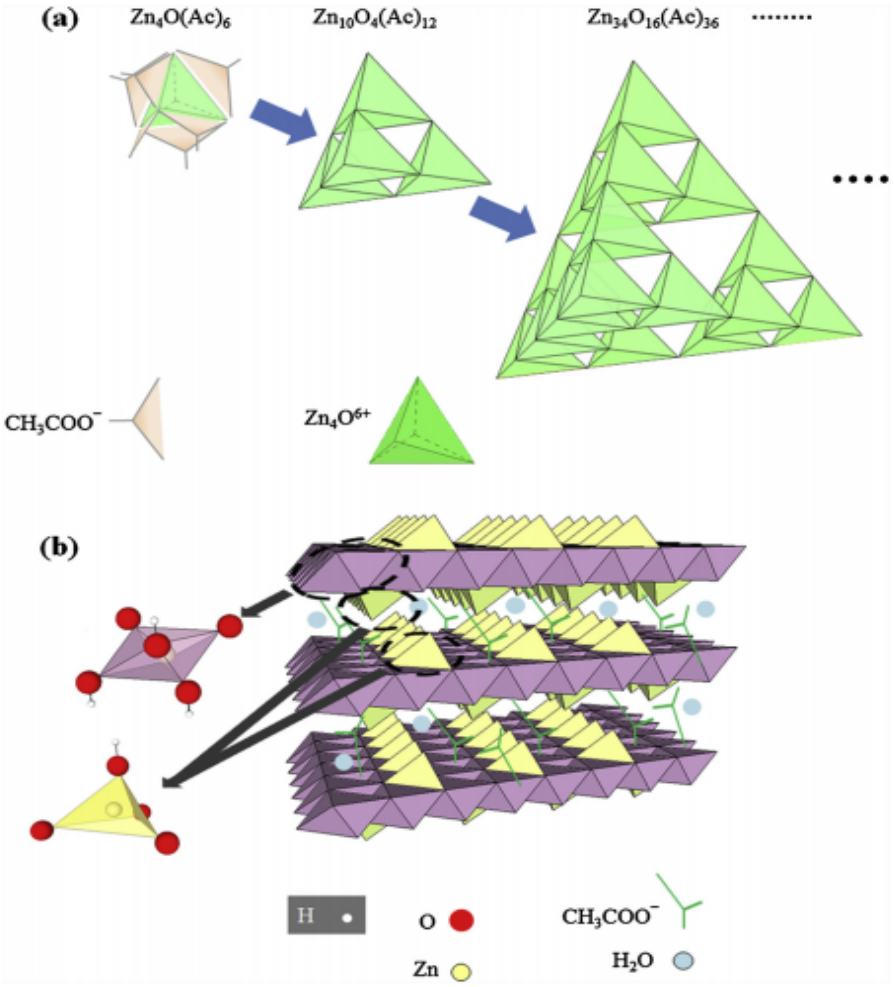

Figure 4.4: Illustration of the two different complexes formed in ZnO sols. a) Zinc oxy-acetate b) Zinc hydroxy double salt [95]

4.2.1 Zinc Precursor

Chemical deposition routes like sol-gel begin with a precursor, the chemical reagent that contains the cation of interest and reacts to form the desired material and phase. Choice of precursor is dependent upon the solvent used, formulation, and desired processing route [87]. Several zinc precursors have been used including: nitrate, chloride, perchlorate, acetylacetonate and alkoxides. Solution routes to ZnO TCOs typically employ metal salts like acetates, chlorides or nitrates as precursors because these compounds are cheap and readily available from commercial suppliers and could be applied to large-scale applications. One drawback of using inorganic salts like nitrate and chloride compared to organic salts like acetate is related to the inclusion or difficult removal of anionic species in the final product [96, 97]. In the case of zinc acetate, the acetate anion, as contaminants of the gel, decompose during pre-heating producing combustion volatile by-products [97]. Also, acetate being a short alkyl chain carboxylate is soluble in polar solvents like alcohols and acetic acid, one of the products of the hydrolysis reaction is also soluble in alcoholic mediums.

A carboxylate is the corresponding metal salt of a carboxylic acid of the form $M(RCOO)_n$ where M is the metal cation and R is the organic substituent. The negative charge of the carboxylate ion is delocalized between the two oxygen atoms in a resonance structure, which stabilizes the ion [87]. It can bind to metal cations in various ways as a mono- or poly-dentate ligand. Bahnemann et al. [98] synthesized transparent colloidal suspensions of ZnO in water, 2-propanol, and acetonitrile using different zinc salts. They reported that the anion in the zinc salt is critical for the preparation of transparent and stable ZnO colloids. The use of zinc perchlorate instead of zinc acetate yielded a turbid suspension; i.e., coagulation of the particles occurs and therefore the acetate anion helps to stabilize the colloidal sol. Supporting results were reported by Znaidi et al [99] in which hydrated zinc salts (acetate, nitrate, perchlorate) were dissolved in ethanol or 2-methoxyethanol in the presence of MEA. Translucent colored colloidal sols or precipitates were obtained after aging depending on the anion and concentration. For nitrate, no sols could be reproducibly obtained. In perchlorate solutions, excess MEA led to formation of sols, after a slow dissolution of the initially formed precipitates. Solutions stemming from zinc acetate and MEA led to reproducible systems, under a variety of experimental conditions. They concluded that acetate plays an important role in sol formation by complexing Zn(II) cations, in

competition with the MEA and formation of stable translucent sols by forced hydrolysis of Zn(II) complexes by water supplied by the hydrated salt.

In the work by Kim et al [100], they found that a molarity of 0.7 M resulted in the highest (002) orientation compared to other concentrations between 0.3 to 1.3 M using ZAD in 1-Propanol and MEA. Similar results were reported by Znaidi et al. [99] in which a concentration of 0.75 mol/L of ZAD in 2-methoxyethanol and MEA resulted in highly c-axis oriented films. Due to the similar dielectric constant of 1-Butanol (17.80 @ 20°C) compared to 2-methoxyethanol (16.90 @ 20°C) and 1-Propanol (20.1 @ 25°C) which primarily determines the solubility of electrolytic salts in the alcohol, a ZAD concentration of 0.75 mol/L was used in this work which resulted in a stable translucent sol after aging.

In the work by Znaidi et al [93], different preferential orientation of ZnO films were related to precursor concentration rather than nature of the precursor (i.e. colloidal vs soluble precursors). Using a dilute sol (<0.2 mol/L) resulted in particulate coating which lead to crystal orientations where the c-axis is parallel to the substrate. However, when using concentrated colloidal sols (>0.2 mol/L), deposition of a continuous film was achieved which lead to normal c-axis orientation with the substrate. Therefore, the contact between particles is a critical issue concerning orientation. It is widely recognized that interaction with the substrate plays an important role in nucleation and during first growth stage [101]. On the other hand, it is well known that in the growth of thicker films, the stronger interaction is between the growing particles. In these conditions, growth processes rather than nucleation, can control orientation. This is also demonstrated in sputtered ZnO, where random nucleation is followed by ordered growth of dense films [102]. In other words, while grain growth of ZnO is along the c-axis, the orientation depends on the type of interactions that dominate.

In summary, organic metal salts, specifically ZAD is an excellent choice as a zinc precursor because of their low cost, abundant availability and relatively easy removal of anionic species which decompose during pre-heating. In addition, the water required for hydrolysis to take place is supplied by the hydrated metal salt. [99] and [98] proved that acetate anion helps to stabilize the sol leading to stable and reproducible sols. A concentration of 0.75 mo/L was chosen based on previous work [100, 99] which showed highest c-axis orientation at those concentrations using alcohol solvents. Concentrated sols result in particle-particle interactions dominating during

growth resulting in improved c-axis orientation.

4.2.2 Solvent

The role of the solvent is to dissolve the metal salt precursors which then undergo hydrolysis and condensation reactions in the liquid medium to obtain a sol and means of being able to deposit the sol using various solution deposition techniques. The choice of solvent is a balance between solubility and deposition requirements. Aqueous solutions are appealing because they are cost-effective and have no detrimental impact on environment but are typically only used when the aim is to produce nanoparticles and quantum dots not films [95]. Instead, organic solvents like alcohol or other mixtures are used often because of increased solubility and ability to tune solution properties for deposition resulting in films. Table 4.1 lists the most commonly used solvents in zinc oxide sol-gel as well the important properties to consider when choosing a solvent. Namely, dielectric constant, viscosity and boiling point. The solvent must present a relatively high dielectric constant in order to dissolve the metal salts. Most alcohols are dipolar, amphiprotic solvents with a dielectric constant that is dependent on the chain length [103]. Hosono et al. [104], performed a comparative study of chemical reactions from ZAD to ZnO using different alcoholic solvents (methanol, ethanol, and 2-methoxyethanol). They found ZAD to be more soluble in methanol than in ethanol or 2-methoxyethanol according to the dielectric constants of these alcohols. Nucleation and coarsening rate increase with increasing chain length (from C2 to C6) and increase with temperature in all alcohols [103]. This is supported by the work done by [104, 105] which found the time required for formation of ZnO increases with chain length.

Table 4.1: Properties of common alcohol solvents used in sol-gel [106, 107]

Alcohol	Dielectric constant (20°C)	Viscosity (cp, 20°C)	Boiling Point (°C)
Methanol	32.35	0.55	64.7
Ethanol	25.00	1.10 (at 25°C)	78.3
1-Propanol	20.81, 20.10 (at 25°C)	2.26	97.2
2-Propanol	18.62	2.86 (at 15°C)	82.2
1-Butanol	17.80	2.95	117.7
2-Butanol	15.80 (at 25°C)	3.00	99.5
2-Methoxyethanol	16.90	1.72	124.6

Viscosity needs to be considered because depending on the solution deposition technique chosen, a solvent with relatively low or high viscosity may be required. For example, the commonly used 2-methoxyethanol has a relatively high viscosity and would be better suited for deposition

methods like screen-printing, spin- and dip-coating. It would not be well suited for deposition methods like spray-coating, inkjet printing and aerosol jet due to risk of clogging up the system. Instead, for such deposition techniques, a lower viscosity alcohol solvent like methanol is used. For dip-coating, the deposition technique used in this work, the viscosity of the alcohol solvent dictates how thick of a coating can be applied at different withdrawal speeds as discussed in 5.1.1.

Lastly, boiling point needs to be considered because the nature of the deposited wet film is highly dependent upon both the precursors and solvents used. Highly volatile, i.e, low boiling point solvents can evaporate too quickly resulting in rough or porous film morphology [87]. This is why 2-methoxyethanol is most commonly used when a dense film is desired. However, it should be noted that 2-methoxyethanol, despite its good physical properties, is toxic to reproduction, being labeled with Risk Phrase R60 (category 2: 'May impair fertility') by the International Programme on Chemical Safety, among others. There is a tradeoff between solvent viscosity and volatility. Solvents with a high molecular weight allow for increased viscosity but also typically require higher temperatures in order to be removed. Depending on the substrate used, like flexible substrates which require low temperature deposition, alcohol solvents with a high boiling point would be a poor choice.

In summary, a solvent with relatively high dielectric constant should be used in order to dissolve the metal salt precursor. The solution deposition technique used will dictate whether to use a solvent with relatively low or high viscosity and in situations where a dense film is desired, a relatively high boiling point solvent should be used. While 2-methoxyethanol has all the desirable physical properties for synthesis of ZnO thin films via dip-coating, it's health hazards can not be avoided. Therefore, for the work presented in this thesis, 1-Butanol was used. Compared to 2-methoxyethanol, 1-Butanol has a higher dielectric constant, slightly lower yet still relatively high boiling point and higher viscosity while being less toxic and having significant miscibility with amines. Significant miscibility with amines is important given the stabilizer used in this work.

4.2.3 Stabilizer

The additive, commonly known as the stabilizer has numerous roles in the synthesis of ZnO via sol-gel such as reacting with the precursor, facilitating formation of complexes, stabilizing the sol, i.e. controlling the rates of reactions and promoting formation of thin films. Alkanolamines

are frequently used in ZnO sol-gel systems with monoethanolamine and diethanolamine being the most prevalent [108, 109]. Other stabilizing additives used are alkali metal hydroxides, carboxylic acids, alkylamines, acetylacetone and polyalcohols [110].

Since in sol-gel, hydrolysis of precursors triggers the reactions of sol formation, a basic or aqueous medium is normally required. As mentioned in 4.2.2, aqueous solutions are generally aimed to produce nanoparticles and quantum dots, and are not suitable for film synthesis. Basic solutions are mostly prepared by adding inorganic bases like NaOH and LiOH. However, they can cause precipitation, avoid film formation and structural contamination of ZnO films [111, 112]. Instead, aliphatic amines like the just mentioned alkanolamines, are used as additives because of their basic nature, significant miscibility with organic solvents like alcohols, stabilizing effect, promotion of precursor dissolution, control of reaction rates and aiding film formation during coating [95]. These types of stabilizers also lower the chance of impurities to contaminate ZnO structure compared to inorganic bases. As well as, possess lower health risks and environmental hazards compared to aromatic amines. The molecular structure of these amines is the main determinant of their chemical and physical properties particularly polarity, reactivity, boiling point and viscosity. These properties, in turn, specify the behavior of each amine in sol-gel process and cause a drastic effect on thin film properties.

Hosseini Vajargah et al [95] performed a comprehensive study concerning comparative effects of various amino-stabilizers on the sol-gel behavior and resulting properties of sol-gel derived ZnO thin films. Monoethanolamine (MEA), Diethanolamine (DEA), Triethanolamine (TEA), Triethylamine (TeA) and Ethylenediamine (EDA) were used as stabilizers. It was found that using MEA, DEA and EDA resulted in transparent sols. The transparency of sols depends on the size of solid phase particles in the colloidal solution which in turn depends on the type and rate of reactions. The better stabilizing behavior in MEA and DEA sols are due to the non-symmetric geometry of the molecules which increases the polarity and basicity that eventually results in catalyzing the dissolution and hydrolysis reactions [113]. MEA-stabilized sols maintained the best stability, maintaining transparency and homogeneity through to the formation of the xerogel. It was observed that MEA-stabilized films were preferentially oriented along the c-axis.

In summary, the function of MEA could be underlined as a complex-forming agent that: (1) controls the rate of reaction by competing with other negatively charged species (OH^- and Ac^-)

which leads to regulated gelation of coated sol in appropriate time; (2) absorbs to positively charged facets of Zn-complexes that promote surface stabilization of complexes and facilitates their coordination and condensation; and (3) evaporates largely by heating in 120°C which diminishes overlap of (a) evaporation, (b) decomposition of organic residue, and (c) crystallization during heat treatment.

4.2.4 n-Type Doping

As mentioned in 3.2.2, group III elements (B, Al, Ga, In) are the most widely used dopants to increase n-type conductivity. The most prominent of the group III elements being aluminum. Indium is avoided due to its high cost and boron doesn't yield as transparent and conductive thin films compared to gallium and aluminum. Gallium appears to be a better candidate compared to aluminum due to its ionic radii (0.062 nm) being closer to Zn^{2+} (0.060 nm) compared to aluminum (0.052 nm) resulting in less distortion of the crystal structure [114]. Gallium is also more stable against oxidation compared to aluminum [115] which would act as electron scattering centers [116].

Despite these apparent advantages, previous experimental results do not show a distinct advantage to using gallium over aluminum. However, one metric where aluminum doped ZnO films outperform gallium doped ZnO films is in terms of crystallinity. Gallium doped ZnO films obtained through sol-gel are often polycrystalline with preferential orientation towards (101) irrespective of solvent, zinc source, stabilizer, pre-heat temperature and deposition method. However, while aluminum doped ZnO films obtained through sol-gel are also typically polycrystalline, they exhibit c-axis preferential orientation. With mindful choice of solvent, zinc source, stabilizer and pre-heat temperature, the c-axis preferential orientation can be further improved to a point where the (002) peak dwarfs the (100) and (101) side peaks. Since obtaining highly crystalline c-axis preferential films is one of the objectives of this work, it was decided to strictly focus on aluminum as the dopant to increase n-type conductivity.

Aluminum has been extensively used in literature with comparable results to Ga at low doping concentrations (0-2 at.%) [117, 118, 119, 120]. At higher doping concentrations (>2 at.%), doping atoms occupy the interstitial positions or form Al and Ga oxides, which entirely distort ZnO crystal structure [121]. In the work presented in this thesis, aluminum was used as the dopant source. Specifically, aluminum nitrate nonahydrate, aluminum chloride hexahydrate and aluminum sulfate

octahydrate to see which produced the best ZnO:Al thin films based on crystallinity, porosity, transparency in the visible range and electrical property. The reason for the choice in these three Al source is because aluminum nitrate nonahydrate is the most common of the three used in literature and was to be used as a baseline. Aluminum chloride hexahydrate was choosen due to having less water present compared to aluminum nitrate nonahydrate. The addition of water from the aluminum sources greatly reduces particle size due to the influence on hydrolysis and condensation reactions during sol preparation [116]. Thus by using aluminum chloride hexahydrate, the hope is to achieve a larger particle size compared to aluminum nitrate nonahydrate. Lastly, aluminum sulfate octahydrate was chosen based on the fact that their are two Al atoms per molecule and therefore would require half the number of aluminum sulfate octahydrate molecules compared to aluminum nitrate nonahydrate and aluminum chloride hexahydrate to achieve the same doping concentration.

4.3 Pre-heat Treatment

Following solution preparation, the sol is ready to be deposited which can be done using numerous solution-based deposition techniques. Pre-heating is then performed immediately following deposition. The purpose of the pre-heating step is to evaporate solvent, stabilizer and decompose residual organics which in this work is acetate yielding the dry film or xerogel. Numerous publications have studied the effect of pre-heating temperature on crystalline quality and have found that the crystallization of ZnO thin films is strongly affected by pre-heating temperature, solvent and post-heating temperature [122, 123, 120].

In the work by Ohyama et al [123], using ZAD, 2-methoxyethanol and MEA, it was found that in the range of 200°C to 500°, an optimal pre-heating temperature of 300°C resulted in the highest degree of c-axis crystal orientation. This is because during the pre-heating stage, it is critical to separate or minimize the overlap of (a) evaporation, (b) decomposition of organic residue and (c) crystallization during further heat treatment. The boiling point of 2-methoxyethanol and MEA are 125°C and 170°C respectively. Therefore a minimum pre-heat temperature as high as 200°C is required for solvent and stabilizer to vaporize completely out of the wet film. Thermal decomposition of zinc acetate is 240°C [124] and the crystallization of ZnO in the films prepared from ZAD-2-methoxyethanol-MEA solutions begins at 200°C to 300°C [125]. Taking theses into account, the evaporation of solvent and stabilizer, decomposition of acetate and crystallization

of zinc oxide may overlap or even occur almost simultaneously when the heating rate and/or temperature is high. Since structural relaxation of the gel film can only take place before the crystallization of ZnO and is induced by solvent and stabilizer evaporation as well as acetate decomposition. A high heat rate will give the film less chance to structurally relax and ultimately result in a more porous film with inferior crystal quality and orientation.

On the other hand, when the heating rate is low, the gel film is given enough time to be structurally relaxed before crystallization, resulting in denser films. In terms of temperatures, high pre-heat temperatures (>300°C), cause evaporation, decomposition to occur abruptly and simultaneously with crystallization, disturbing the unidirectional crystal growth. While low pre-heat temperatures (<300°C) result in incomplete evaporation and decomposition. Then, during the higher temperature post-heat treatment, further evaporation and decomposition will occur simultaneously with crystallization, again, disturbing the unidirectional crystal growth.

These initial findings were further validated by [122, 120]. In [122], using ZAD, isopropanol and monoethanolamine, FTIR and thermogravimetry differential thermal analyser (TG-DTA) supported the findings by [123] and ultimately determined a pre-heat temperature of 275°C to be optimal for achieving a dense film consisting of nano-sized, highly c-axis oriented crystalline particles. Similarly, in [120], using ZAD, 2-methoxyethanol and monoethanolamine, FTIR and TG-DTA results were in agreement with [122]. Again, it was found that a pre-heat temperature of 275°C to be optimal.

In summary, the purpose of the pre-heating step is to evaporate solvent, stabilizer and decompose residual organics (acetate) yielding the dry film or xerogel which then undergoes further heat treatment at higher temperatures to produce nano-crystalline thin films. In order to achieve highly c-axis oriented films, it is critical to separate or minimize the overlap of (a) evaporation, (b) decomposition of organic residue and (c) crystallization during further heat treatment. Numerous publications have already investigated the effect of pre-heating temperature on film quality in terms of crystallinity and film density. From their work, it was found that an optimal pre-heat temperature around 300°C resulted in the best films. Lower pre-heat temperatures resulted in incomplete evaporation and decomposition which then continues simultaneously with crystallization during higher temperature 2nd anneal step. Higher pre-heat temperatures resulted in evaporation, decomposition and crystallization to occur simultaneously.

In both situations, unidirectional crystal growth is disturbed resulting in inferior c-axis orientation. In addition, a slower heat rate allows time for structural relaxation of gel film resulting in a denser film. Based on these findings, a pre-heat temperature of approximately 300°C was initially chosen. However, initial experimental results revealed a temperature of 300°C at the thermocouple mounted inside the custom heater assembly was too high and evaporation, decomposition and crystallization occurred simultaneously yielding a 'cloudy' film. From these initial findings, the temperature was reduced to 200°C at the thermocouple which yielded a transparent film indicating that evaporation, decomposition and crystallization overlap had been reduced to an acceptable degree. Based on these initial experimental results, a temperature of 200°C at the thermocouple was used throughout the work presented in this thesis. While the heat rate could not be controlled, it took approximately 4 minutes for the heating apparatus to reach pre-heating temperature from 25°C.

4.4 Post-heat Treatment

The post-heat treatment is conducted at higher temperatures than during the pre-heating step. The purpose of the 2nd anneal step is to drive off any organic residue that may remain from pre-heating and to produce a film of ZnO. According to XPS data, SIMS analysis by Armelao et al. at 500°C the formation of ZnO was complete. For a great number of systems, the temperature used ranges from 500 - 600 °C. Above this range, loss of orientation in the (002) direction is observed [123, 126]. For the work presented in this thesis, a post-heat treatment temperature of 500°C was used for all samples.

Chapter 5

Fabrication and Characterization Techniques

5.1 Fabrication Technique

5.1.1 Dip Coating

Overview

Dip coating is the process where a liquid film is deposited via precise and controlled withdrawal of a substrate from solution. This is typically done using an instrument referred to as a 'dip coater'. The dip coating process occurs in five stages: immersion, dwelling, withdrawal, drying and curing. During immersion, the substrate is lowered into the solution until it is mostly or fully immersed. Next, a short delay, typically thirty seconds to one minute, occurs before the substrate is withdrawal known as dwelling. Dwelling allows for the substrate to reach thermal equilibrium with the solution. The solution is typically heated above room temperature to allow for improved film uniformity and mitigate evaporation cooling effects which can result in a "hazy" coating.

During the withdrawal stage, interaction of several sets of forces occur which leaves a thin layer of the solution on the surface of the substrate. These forces can be categorized as draining forces or entraining forces. Draining forces are forces that draw the solution away from the substrate and back towards the solution bath such as gravitational forces and surface tension. Entraining forces are forces that work to retain fluid onto the substrate such as fluid friction also known as viscous force. The balance of these forces ultimately determines the thickness of wet

film coated onto the substrate.

Finally, after withdrawal stage, there are the drying and curing stages. During the drying stage, evaporation of solvent occurs at the surface of the deposited wet film. The evaporation first occurs uniformly over the entire surface which turns the wet film into a gel-like film. However, small amounts of solvent become trapped within the gel-like film and further evaporation of the solvent is then determined by diffusion of solvent toward the surface. The last stage is the curing stage and isn't always necessary. However, the curing stage is required in synthesis of ZnO via sol-gel. The curing stage, removes any remaining solvent and decomposes any organic residue in the gel-like film. The curing stage is also referred to as the pre-heat treatment through out this thesis.

While all these stages are essential in the dip coating process, the critical stages for determining the properties of the deposited film are the withdrawal and drying/curing stages.

Film Formation

The formation of the film involves four distinct regions: static meniscus, dynamic meniscus, constant thickness zone and wetting zone. These regions are illustrated in Fig. 5.1a. The static meniscus is where the shape of the meniscus is determined by a balance of the hydrostatic and capillary pressures. The dynamic meniscus occurs at the stagnation point. The stagnation point is where the entraining forces and draining forces are at equilibrium. Above the dynamic meniscus is the constant thickness zone where a thin layer of wet film has been deposited on the substrate at a given thickness (h_0). The final region is where deposition of the wet film began is referred to as the wetting zone.

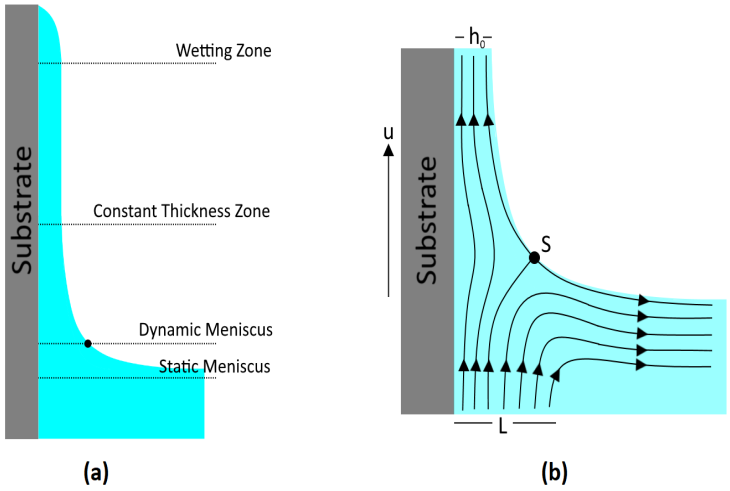

Figure 5.1: Film formation and solution flow in dynamic meniscus

Fig. 5.1b illustrates the flow of the solution in the dynamic meniscus region. The transition from static to dynamic meniscus occurs within the boundry layer, L. Within this layer, the forces from viscous flow impact the way the solution moves. Beyond this layer, the viscous forces become insignificant and as previously mentioned, the shape of the meniscus is determined by a balance of hydrostatic and capillary pressures. The point labelled S is the stagnation point where entraining and draining forces are equal.

As the substrate is withdrawal from the solution bath, the solvent begins to evaporate. As a result, the dilute sol aggregates and begins to form a gel from polymers linking together leading to a wet gel which is turned into a dry gel or *xerogel* after the drying and curing stages. This is illustrated in Fig. 5.2.

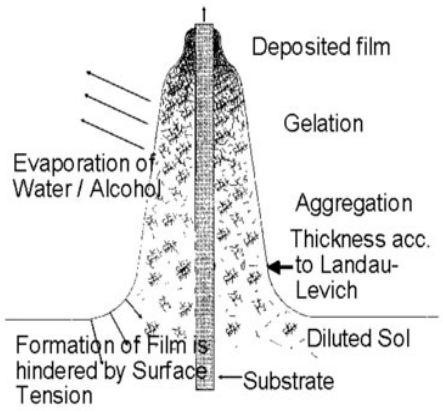

Figure 5.2: Solvent evaporation leading to wet gel via aggregation and gelation [127]

Withdrawal Regime

As mentioned above, during the withdrawal stage an interaction of several sets of forces occur which ultimately determines the thickness of the deposited film. There are three coating regimes defined by which forces dominate the behavior of the coating. The regimes are called viscous flow, draining and capillary regimes. The viscous flow regime occurs at high withdrawal velocities (>10 mm/sec) and viscous solutions in which vicious forces and gravitational attraction dominate. However, in most situations, including the work presented in this thesis, the withdrawal speeds or solution viscosity are not high enough for operation in this regime. As a result, the viscous force is weaker and the balance between entraining and draining forces become dependent upon surface-tension driven movement of the solution.

Under these conditions, withdrawal operation is said to be taking place within the drainage regime. In this regime, surface-tension can not be ignored and the relationship between wet film thickness and withdrawal speed of substrate can be described by the Landau-Levich equation given by Eq.(5.1). Where h_0 is film thickness, η is solution viscosity, ρ is solution density, U_0 is withdrawal speed, γ_{LV} is liquid-vapor surface tension, g is gravitational constant, and c is a constant related to the curvature of the dynamic meniscus.

$$h_0 = c\frac{(\eta U_0)^{\frac{2}{3}}}{\gamma_{LV}^{\frac{1}{6}}(\rho g)^{\frac{1}{2}}} \tag{5.1}$$

The assumption can be made that certain parameters such as viscosity (η), solution density (ρ) and liquid-vapor surface tension (γ_{LV}) remain constant through out the dip coating process. As a result, Eq.(5.1) can be simplified to Eq.(5.2). Where h_f is the final thickness of the film and D represents all the parameters combined, which are assumed to be constant. This reveals that the final film thickness exhibits a power to $\frac{2}{3}$ relationship with withdrawal speed when operating in the drainage regime.

$$h_f = DU_0^{\frac{2}{3}} \tag{5.2}$$

The capillary regime arises at very slow withdrawal speeds. When the withdrawal speed is reduced such that the entraining forces dominate.

5.1.2 Dip Coating Apparatus

Construction

A cost-effective dip coating apparatus was constructed in order to dip substrates into the solution bath. The brains of the apparatus is the 'Blue Pill' development board based on ST Microelectronics' STM32F103C9T6 microcontroller that has an ARM Cortex-M3 core. The CPU operates at 72 MHz, supports I^2C, SPI, UART, CAN, USB communication protocols and contains 64/128 kB and 20 kB of flash memory and SRAM respectively. The board is programmed in Arduino IDE. The code for the dip coater can be found in the appendix.

The microcontroller communicates with a TMC2130 stepper motor driver module. The TMC2130 operates in Step/Direction driver mode. In this mode, the microcontroller generates step and direction signals. The TMC2130 provides a microstep counter and a sine table to convert these signals into the coil currents which controls the position of the motor. The TMC2130 automatically takes care of intelligent current and mode control and delivers feedback on the state of the motor. The stepper motor used is a SureStep stepper motor, STP-MTR-17048. The stepper motor is bipolar with an 83 oz-in holding torque, 1.8° step angle, 200 steps per revolution and NEMA 17 frame. The stepper motor was attached to a lead screw using a flexible aluminum shaft coupler and the lead screws pitch is 8 mm.

All the components were housed in a 3D printed enclosure from Polylactic Acid (PLA), a common material used in extrusion-based 3D printers. A 'platform' was 3D as well in order to attach the substrates to be dipped. The platform contained two linear bearings affixed to the sides of the platform which traveled on smooth rods and a copper nut screw that would raise and lower the platform when the stepper motor rotated the lead screw. An aluminum bar was attached to the platform which allowed for the required vertical travel between solution bath and heater used for pre-heat treatment. At the end of the bar, two small mica squares on opposite sides of the bar were compressed via nut and bolt in order to 'pinch' the substrate and hold it during operation. The mica squares also provided thermal insulation between the substrate and aluminum bar which would travel through the heater during operation and be warm as a result.

The dip coating apparatus features a pushbutton, a two position slide switch which are used to interface with the program and LED indicators to provide feedback on the state of the machine. A limit switch at the top of the apparatus is used for homing the platform upon power up. All the electronics are powered by a laboratory bench power supply by GW INSTEK, GPS-3303. The power supply was set to 26 V for the stepper driver. A LM7805 voltage regulator was used to step down the 26 V used for the motor to 5 V in order to power the microcontroller and stepper motor driver.

A cost-effective heater was constructed in order to perform the pre-heat treatment operation and allow for subsequent deposition operations without having to remove the substrate or require additional interaction with the apparatus. Allowing for 'set it and forget it' operation. The heater was constructed by forming Nichrome wire into a coil and containing it within four walls of mica sheets for better containment of heat. The heater was powered by a Staco Energy variable autotransformer, TYPE 3PN210, providing an output voltage from 0 to 140 V and rated for 3.1 kVA. A power relay by Songle, SLA-12VDC-Sl-C was used to control when the heater would turn on. The relay was provided 12 V from channel 2 of the bench power supply. A npn transistor, pn2222 was used to sink the low side of the relay. The gate of the transistor was controlled by the microcontroller. A k-type thermocouple connected to a PID temperature controller by Inkbird, ITC-106VH, was used to monitor the temperature inside the heater.

Initially, the PID temperature controller was used to try to maintain a constant temperature but that was found to be not feasible. The constructed heater did not have enough thermal mass

and the temperatures would fluctuate quickly and drastically when using the PID temperature controller. Instead, the output voltage of the autotransformer was set to a value that allowed the heater to reach a desired steady state temperature after some heat up time. Steady state temperatures at different output voltages were recorded and heat up times were measured in order to determine what output voltage was required for a desired steady state temperature and how much additional time was required during the pre-heat treatment to account for heat up time. The setup just described is illustrated in Fig. 5.3.

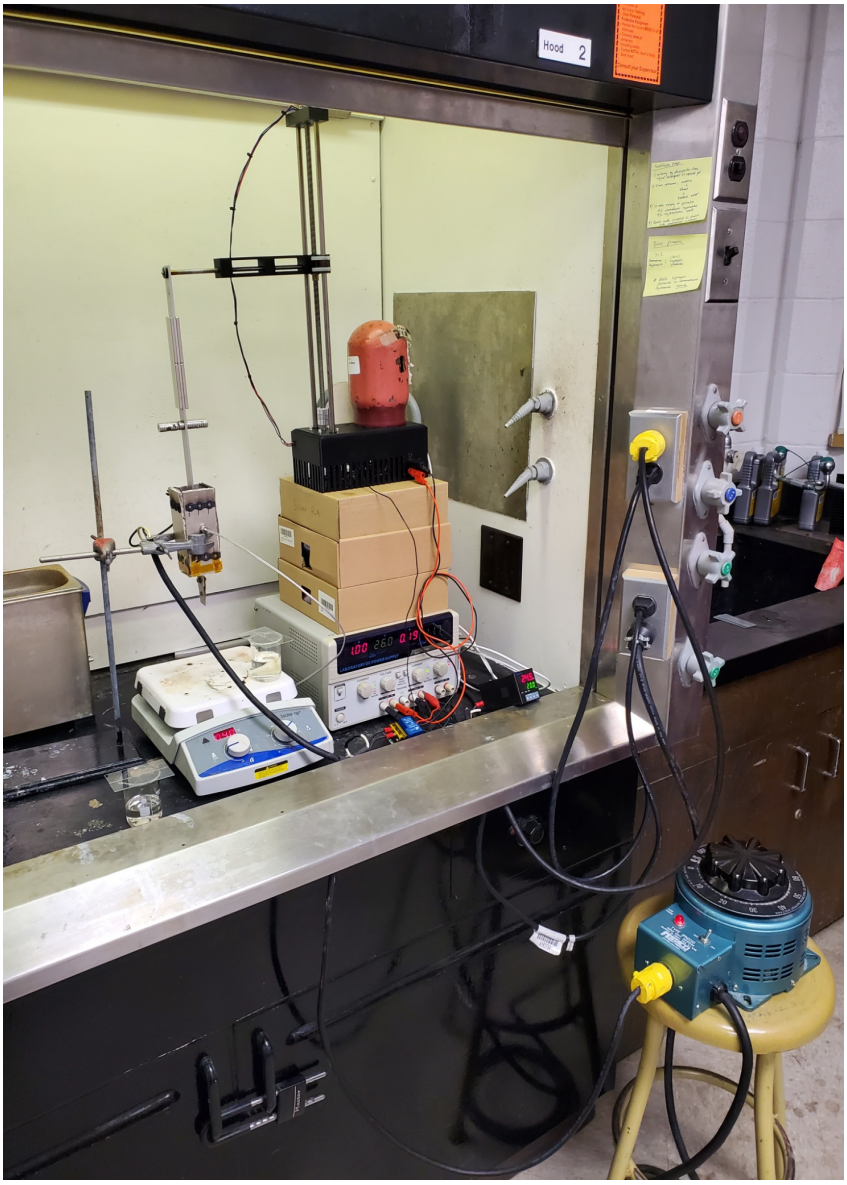

Figure 5.3: Dip coater setup

Operation

Upon power up, the platform would home itself by raising until the limit switch at the top was triggered. Once homed, a desired dip distance must be set in order for the operation to begin. This was done by toggling the slide switch to program mode. Once in program mode, the operator presses the pushbutton in order to lower the platform and holds the pushbutton until the desired dip distance is reached. During this operation, the microcontroller counts how many step pulses were sent to the stepper motor driver in order to reach the desired dip distance. This count is then stored and used to ensure the same dip distance is reached every time the substrate is dipped. Once the platform returns to the top, a green LED illuminates indicating the dip distance has been set and the apparatus is ready to run automatically in run mode. Run mode is selecting by toggling the slide switch to run mode.

In run mode, the platform lowers towards the solution bath until the pre-dip distance. At which point, the platform will slowdown to the desired pre-dip speed and travel at that speed until it reaches the desired dip distance. Once the desired dip distance is reached, the substrates remains stationary for a specified dwell time. After the dwell time, the substrate is withdrawn from the solution bath at the desired dip speed until it reaches the pre-dip distance again. Once reaching the pre-dip distance, the platform accelerates and raises up to the heater at a faster speed. After the substrate has reached the heater, the relay for the heater is turned on and the substrate remains in the heater for the pre-heat treatment duration plus heat up time. After which, the substrate is lowered out of the heater and left stationary for a cool down period and then proceeds to repeat the dipping and heating cycle until the desired number of dips is achieved.

5.2 Materials Characterization Tools

5.2.1 X-ray Diffraction

Theory

X-ray diffraction (XRD) is a powerful nondestructive technique used for the characterization of crystalline materials. It provides information on structures, crystal phases, preferred orientations (texture), and other structural details, such as average grain size, crystallinity, strain and crystal defects. Recall that a crystal consists of a highly ordered arrangement of atoms in a three-dimensional structure. When an x-ray beam strikes a crystal, it causes electrons in its path

to vibrate at the same frequency of the incident x-ray. The vibrating electrons absorb some of the x-ray energy and emitt (scatter) this energy isotropically as x-ray radiation with the same frequency and wavelength. In general, the scattered waves interfere destructively. However, in some directions they interfere constructively. This destructive or constructive interference of the scattered x-ray energy is referred to as diffraction. Fig. 5.4 illustrates the condition for constructive interference to occur.

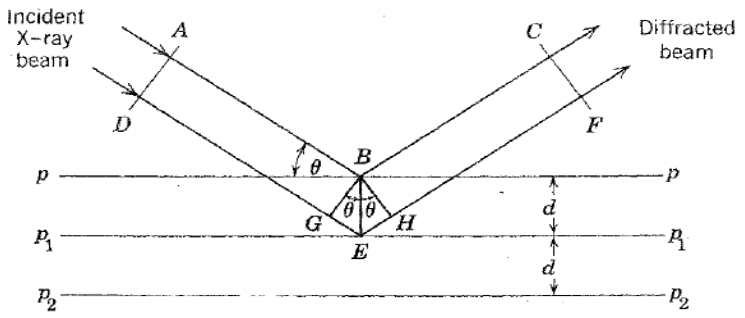

Figure 5.4: Geometry of X-ray diffraction [128]

In Fig. 5.4, lines p, p_1 and p_2 represent atomic planes with spacing d. X-rays that strike the first plane p are reflected at the same angle as the incident angle θ. Similarly, x-rays that strike the second plane p_1 are also reflected at the same angle as the incident angle θ. However, they have a different path length as the x-ray which struck plane p. In order for constructive interefence to occur, the two waves must be in phase. For this to be true, the additional path length, denoted as GEH, must be an integer multiple of the x-ray wavelength. Using trigonometry, we can deduce the GE path length is equal to $dsin\theta$ and EH path length is also equal to $dsin\theta$. This yields the Bragg equation ($2dsin\theta = n\lambda$ = GE + EH) which must be satisfied in order for constructive interference to occur.

X-rays used in XRD are typically generated by striking a pure anode of a particular metal with high-energy electrons in a sealed vacuum tube. The tube is fitted with a tungsten filament as a cathode that provides the source of electrons. When the filament is heated by passing a current through it, electrons are emitted and accelerated to the anode by a potential difference between the anode and cathode known as the accelerating voltage. The accelerated, high-energy electrons impact the anode, displacing a core electron in the anode material. An electron from a lower energy shell 'jumps' to replace the recently displaced core electron, releasing energy in the

form of x-rays that then irradiate the sample. By the right choice of metal anode and energy of accelerated electrons, a known wavelength or group of wavelengths will dominate the x-rays generated. Common metals used for anodes in x-ray generating tubes are copper, chromium, iron, cobalt and molybdenum. Copper x-ray tubes are most commonly used for XRD of inorganic materials. The dominate X-rays generated by copper x-ray tubes are Kα_1, Kα_2 and Kβ_1 with Kα_1 being the one used for XRD due to the fact that it is the most intense because the likelihood of that transition occurring is highest.Kα_1 transitions correspond to an electron transitioning for $2p_{3/2}$ to 1s, Kα_2 transitions correspond to an electron transitioning for $2p_{1/2}$ to 1s, and Kβ_1 transitions correspond to an electron transitioning for $3p_{3/2}$ to 1s. The characteristic wavelength values are 1.54060 Å, 1.54439 Åand 1.39222 Åfor Kα_1, Kα_2, and Kβ_1 respectively.

Measurement Technique

XRD measurements were conducted using Philips PanAlytical X'Pert Pro MPD in θ-2θ mode. In this mode, the x-ray source and detector are kept at the same angle relative to the normal of the sample surface and varied through a range 3° to 50 ° at a scan rate of 0.082065 °/sec. The accelerating voltage of the x-ray generating tube was 45 kV and the current was 40 ma for all samples measured. The Kβ_1 peak was attenuated using nickel foil as a beta filter. The Kα_2 doublet peak was removed using WinPLOTR software.

5.2.2 Scanning Electron Microscopy

Theory

Scanning electron microscopy (SEM) is a surface characterization technique that uses an electron beam focused onto a sample and scanned in a raster pattern to produce an image of a samples surface with resolutions down to 1 nm. The focusing power is a result of the de Broglie wavelength of electrons being significantly lower than that of light, thereby lowering the diffraction limit of the beam spot. It reveals information about the surface topology and chemical composition. In a typical SEM, an electron beam is generated via thermionic emission of a tungsten filament situated in a electron gun (vacuum tube producing narrow, collimated beam of electrons with precise kinetic energies). The electron beam is focused by one or two condesner lenses to a spot size of about 1-5 nm in diameter. The beam then passes through pairs of scanning coils or deflector plates which deflect the beam in the x and y axes. The beam is

deflected in a raster fashion over a square area of the sample surface. Fig. 5.5 illustrates the typical setup in SEM.

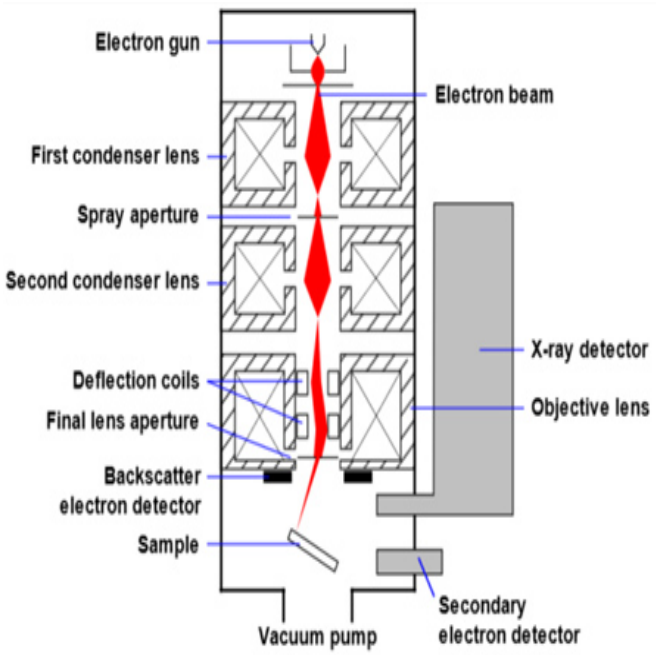

Figure 5.5: Schematic of scanning electron microscopy [129]

Upon impact of the electron beam with the sample, the electrons lose energy by repeated random scattering and absorption within a volume of the specimen known as the interaction volume. The interactive volume extends from 100 nm to 5 μm, depending on the kinetic energy of the electron beam, atomic number and density of the sample. The interaction between electron beam and sample results in numerous detectable signals such as reflection of high-energy electrons via eleastic scattering, emission of secondary electrons via inelastic scattering and emission of electromagnetic radiation in the form of x-rays and visible light. Fig. 5.6 illustrates the signals generated from interaction between electron beam and sample.

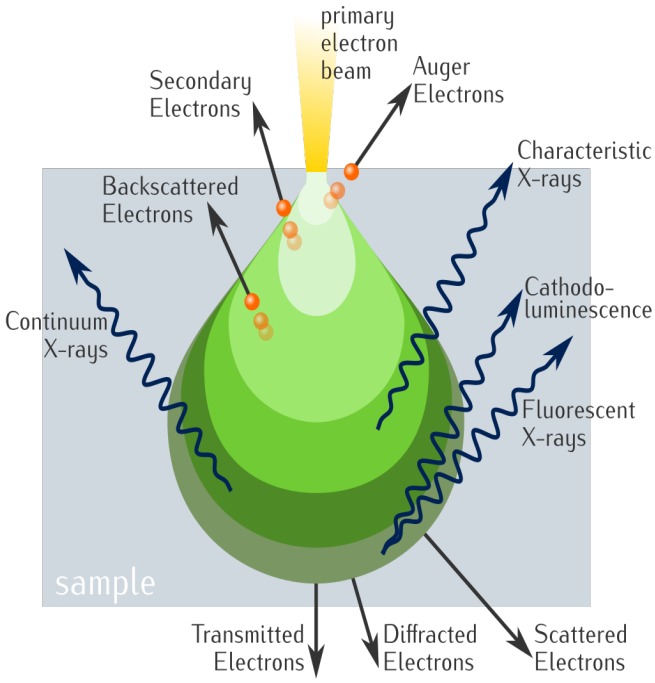

Figure 5.6: Interaction between electron beam and sample in SEM [130]

The most common imaging mode in SEM utilizes secondary electrons. Secondary electrons are ejected from atoms in the sample when an incident electron passes "near" an atom in the sample. Near enough such that the incident electron gives a lower energy electron some of its energy causing a slight energy lose and path change in the incident electron and ionization followed by subsequent ejection of the electron in the atom. This phenomenon is known as inelastic scattering. One incident electron is capable of ionizing several secondary electrons. Due to the low energy (<5 eV) of the secondary electrons, only secondary electrons near the surface (<10 nm) can be detected. Secondary electrons are detected by a Everhart-Thornley detector which consists of a scintillator inside a positively charged Faraday cage. The Faraday cage attracts the secondary electrons which the scintillator converts to light that is subsequently amplified by a photomultiplier. As the electron beam performs a raster scan, a two-dimensional intensity distribution is obtained and converted into a digital image. The contrast in the image being proportional to the number of secondary electrons collected. The incident angle of electron beam on the sample strongly influences the number of secondary electrons emitted. As the angle of incidence increases, more secondary electrons are emitted. Therefore, steep surfaces, edges or any other changes in topography larger than the sampling depth appear brighter than flat surfaces,

resulting in a well-defined image with three-dimensional appearance. The signal from secondary electrons also tends to be highly localized at the point of impact of the electron beam, allowing for image resolutions down below 1 nm.

Another imaging mode in SEM utilizes back-scattered or reflected electrons. Back-scattered electrons occur when an incident electron collides with an atom in the sample which is nearly normal to the incident's path causing the incident electron to change trajectory and be reflected back. This phenomenon is known as elastic scattering. A dedicated backscattered electron detector is positioned above the sample in a ring-like arrangement, concentric with the incident electron beam. Similar to secondary electron imaging, as the electron beam performs a raster scan, a two-dimensional intensity distribution is obtained and converted into a digital image. This technique is useful because larger, heavier atoms scatter electrons more strongly than smaller, lighter atoms. Since the contrast in the obtained images is proportional to the number of electrons scattered, the back-scattered electron technique provides imaging that carries information on the sample's chemical composition, as well as other valuable information on crystallography and topography.

The last technique which will be discussed is energy-dispersive X-ray spectroscopy (EDX). EDX is used to determine which chemical elements are present in the sample, as well as an estimate of the relative abundance. X-rays are emitted by the sample when a vacancy exists in the lower energy shells due to emission of a secondary electron and an electron from a higher energy shell (outer shell) "falls" to occupy or fill that shell. An X-ray is released when the electron transitions from outer to inner shell. The energy of the generated X-ray is equal to the difference in energy levels between the two shells. Since all elements have characteristic and well-known energy levels, one can deduce the chemical composition of the sample by examining the spectrum of x-ray energies detected by an energy-dispersive spectrometer. The relative abundance is calculated as a ratio based on the area under a peak(s) corresponding to a certain element to the total area of all the peaks in the spectrum which correspond to all detected elements.

Measurement Technique

Investigation of samples surface, cross-section, layer thickness and chemical composition were done using Hitachi SU-70 scanning electron microscope under a vacuum of 10^{-4} Torr. The samples

were prepared by obtaining a piece approximately 0.5cm x 0.5cm. This was done using a diamond-tipped scribe in order to score the glass substrate and break a piece of desired size. The samples were then mounted onto a SEM sample holder using conductive carbon tape. Subsequently, the samples were coated in a very thin layer of carbon using DC magnetron sputtering in order to improve image quality. Once coated, the samples were ready for investigation.

5.2.3 Atomic Force Microscopy

Theory

Atomic force microscopy is a non-destructive technique used for topographic imaging of a samples surface and quantifying the surface roughness by calculating the root mean square (RMS) of the scanned area. It provides atomic scale resolution with great cost efficiency and speed with little sample preparation. This is achieved by using a very small cantilever with a fine tip that passes over the surface of the sample in a raster manner. As the cantilever scans over the surface, the deflection of the cantilever is measured by reflecting a laser onto the cantilever and detecting the reflected laser using a photodiode detector. The intensity of the signal by the photodiode detector is proportional to the displacement of the cantilever. Deflection of the cantilever occurs due to forces between the tip and the sample in accordance with Hooke's law. A topographical image of the samples surface is constructed from the measurement of cantilever deflection over the area that tip raster scanned. Depending on the type of mode used, these forces can be mechanical contact forces, van der Waals forces, capillary forces, electrostatic forces, etc. Fig. 5.7 illustrates the typical setup of AFM. The diameter of the cantilever tip ultimately dictates the resolution of the image attainable via AFM.

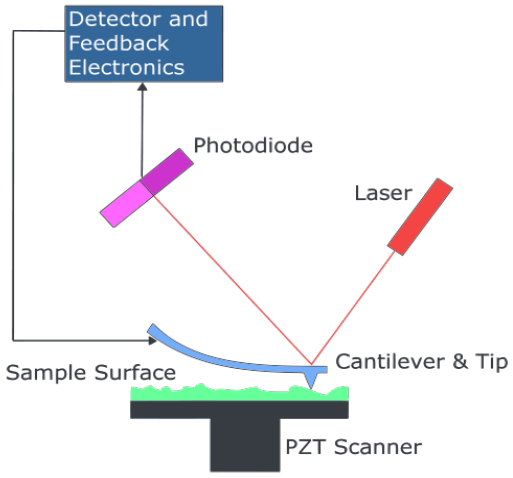

Figure 5.7: Typical AFM setup [131]

There are three types of operating modes in AFM that correspond to how the tip interacts with the sample: contact, non-contact and tapping mode. These are illustrated in Fig. 5.8.

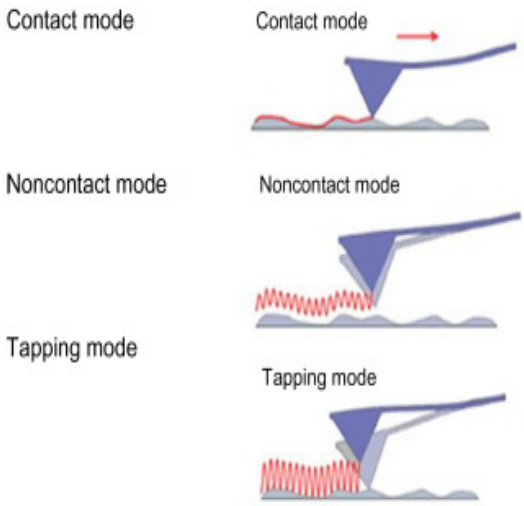

Figure 5.8: Operating modes in AFM [132]

In contact mode, as the name implies, the cantilever tip makes contact with the sample surface. Contours of the surface are measured either using the deflection of the cantilever directly or, more commonly, using the feedback signal required to keep the cantilever at a position such that it experiences a constant deflection force throughout the scan. Cantilevers with a low stiffness i.e. having low spring constant, k, are required for this type of mode. Since the cantilever tip is

making contact with the sample surface, depending on the sample, accelerated wearing of the tip and possible damage to the surface are to be expected.

In non-contact mode, the cantilever tip does not make contact with the sample surface. Instead, the cantilever is situated above the sample and the cantilever is excited at or near its resonate frequency by a piezoelectric transducer. Van der Waals forces, which are strongest from 1nm to 10 nm above the sample surface, act to dampen the oscillation of the cantilever. The dampening of oscillation combined with a feedback loop system corrects the distance between tip and sample surface to maintain either a constant oscillation amplitude or frequency by adjusting the distance between tip and sample surface. Measuring the tip-to-sample distance at each data point allows the AFM software to construct a topographic image of the sample surface. Non-contact mode has it's advantage over contact mode because it doesn't suffer from tip or sample degradation effects. However, non-contact does have the drawback of being influenced by any adsorbed fluid lying on the surface of the sample while in contact mode, the tip is able to penetrate the liquid layer to image the underlying surface.

In tapping mode, similar to non-contact mode, the cantilever tip is excited at or near its resonate frequency by a piezoelectric transducer. However, unlike non-contact mode, the oscillation amplitude of the cantilever is such that the tip makes brief contact with the sample surface, hence the term tapping mode. Similar to non-contact mode, when the tip is close enough to the surface, van der Waals forces, dipole-dipole interactions and electrostatic forces cause the amplitude of oscillation to decrease as it gets closer to the sample surface. The feedback loop monitors the oscillation amplitude and adjusts the cantilever height in order to maintain a constant oscillation amplitude. A tapping AFM image is produced by imaging the forces of the intermittent contacts of the tip with the sample surface. Tapping mode is the most frequently used AFM mode. It has the advantage of being able to penetrate any liquid layer on the sample surface like in contact mode while slowing the degradation of the tip and sample surface compared to contact mode.

Measurement Technique

Surface topographic images were obtained using an AFM Nanosurf Easyscan 2 atomic force microscope operating in tapping mode. The cantilever used was a Multi75E-G silicon probe with Cr/Pt conductive coating. The resonant frequency is 75 kHz with a force constant of 3 N/m. The

dimensions of the cantilever are 225 μm length, 28 μm width and 3 μm thick. The cantilever tip has a height of 17 μm and a tip radius of 25 nm.

5.2.4 Ultraviolet-Visible Spectroscopy (Reflection, Transmission and Absorption)

Theory

Optical measurements are one of the most common and important measurements when it comes to investigation the properties of thin films for TCO applications. In UV-vis spectroscopy, electromagnetic radiation of a narrow spectral bandwidth varied in the range of 190 nm to 1100 nm is passed through a sample and a detector on the other side collects the transmitted radiation. In this spectrum, the energy of a photon is sufficient enough to be absorbed by the sample and excite an electron from valence band to the conduction band. By varying the range of incident radiation, an absorption spectrum is obtained. From that, one can infer properties of the thin film including optical transparency, optical bandgap, film thickness, free carrier concentration, etc.

The typical setup of UV-vis spectroscopy is illustrated in Fig. 5.9. It consists of a broad spectrum light source, monochromator in order to extract only a narrow spectral bandwidth and a detector to measure the transmitted light. The light source is typically some sort of high-intensity discharge lamp and the detector is typically a semiconductor diode detector.

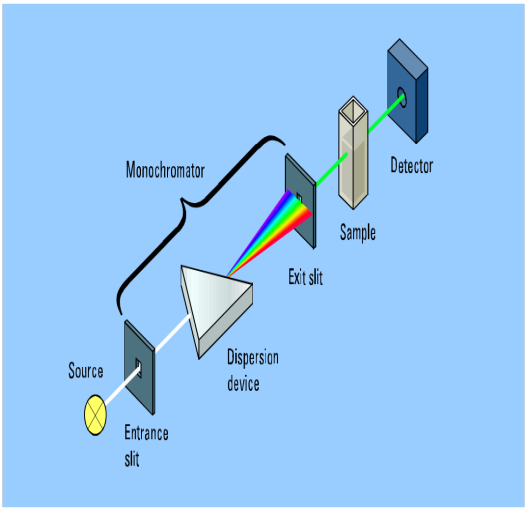

Figure 5.9: Typical UV-Vis setup [133]

The obtained absorption spectrum is the logarithmic ratio of transmitted radiant flux to incident radiant flux, referred to as absorbance (A) given by Eq.(5.3). Where transmitted and

incident radiant flux are ϕ_t and ϕ_t respectively.

$$A = -log(T) = log(\frac{\phi_t}{\phi_i}) \tag{5.3}$$

Measurement Technique

Optical transmission and absorption measurements were conducting using a Varian Cary 50 UV-Vis spectrophotometer with a measurement range of 190 - 1100 nm. It features a Czerny-Turner 0.25 m monochromator achieving a spectral bandwidth of 1.5 nm, a high-intensity xenon flash lamp as a light source and two silicon diode detectors.

5.2.5 Van der Pauw and Hall Measurements

Theory

Characterization of electrical properties including sheet resistance, majority carrier type, majority carrier concentration and majority carrier mobility are done using Van der Pauw technique and Hall effect measurements. The Van der Pauw method is a powerful technique that allows for measurement of a samples resistivity. The power of the technique lies in it's ability to measure resistivity of a sample of arbitrary shape as well as providing an average resistivity for anisotropic materials. This is not possible when using the traditional four-point probe method. Hall measurements provide details on the doping type (n-type or p-type), sheet carrier density and mobility of the majority carriers.

In the Van der Pauw method, four probes are positioned as close as possible to the boundary of the sample. A DC current is passed through two adjacent contacts while a DC voltage is measured across the other two contacts. Typical contact placement and measurement technique is illustrated in Fig. 5.10. A series of voltage measurements are taken by injecting current in both directions through all possible adjacent contact combinations yielding a total of 8 measurements. Resistances are calculated by dividing the measured voltage drops by the known injected current. Based on contact geometry, four of these resistances correspond to vertical resistances and the other correspond to horizontal resistances. These values are then averaged to obtain a average vertical resistance (R_v) and average horizontal resistance (R_h) which can be solved numerically for sheet resistance (R_s) using Eq.(5.4).

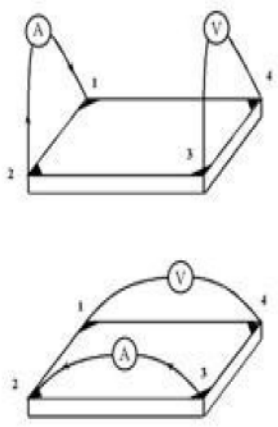

Figure 5.10: Typical Van der Pauw setup [134]

$$e^{\frac{\pi R_v}{R_s}} + e^{\frac{\pi R_h}{R_s}} = 1 \tag{5.4}$$

Hall effect measurements are based on Lorentz force law. According to Lorentz force law, if a moving charge, typically an electron, is traveling at a certain velocity in the presence of a perpendicular magnetic field, the charge will experience a force due to the magnetic field. This force, referred to as Lorentz force or electromagnetic force is perpendicular to both the direction of travel and magnetic field. The magnitude of the Lorentz force is proportional to the strength of the magnetic field and the velocity of the charge. Lorentz force law is expressed in Eq.(5.5). Where q is elemental electric charge (1.602 x 10^{-19}), E is the electric field the charge is subjected to in order to accelerate it, v is velocity of charge and B is magnetic field.

$$\vec{F} = q\vec{E} + q\vec{v} \times \vec{B} \tag{5.5}$$

For measurements, the probe setup remains the same however the sample is now positioned in a uniform magnetic field perpendicular to the samples surface. When a current is injected into the sample, the moving electrons will experience an additional force from the magnetic field in accordance with Lorentz force law. The charges will drift to one side of the sample resulting in a separation of charge concentrations in the sample which can be measured in the form of a potential difference known as the Hall voltage. Current is injected and collected through two

opposite contacts while the Hall voltage is measured across the other two opposite contacts. The direction of current is then reversed and Hall voltage is measured again. This is then repeated by injecting and collecting current through the contacts that were previously measuring the Hall voltage while measuring the Hall voltage across the contacts that previously had current injected and collected through. These four Hall voltage measurements are then repeated for magnetic field in the opposite direction for a total of 8 Hall voltage measurements. The overall Hall voltage is then calculated from these 8 Hall voltage measurements. From the overall Hall voltage, the majority carrier type, sheet carrier density and carrier mobility can be calculated.

For most setups, including the one used in this thesis, a positive Hall voltage indicates the material is P-type with the majority carriers being holes and a negative Hall voltage indicates the material is N-type with the majority carriers being electrons. The sheet density of majority carriers (η_S) can be calculated by Eq.(5.6) and the majority carrier mobility (μ_m) can be calculated by Eq.(5.7). Where I is the injected current in amperes and B is the magnetic field in Gauss.

$$\eta_s = \frac{IB}{q|V_H|} \tag{5.6}$$

$$\mu_m = \frac{1}{q\eta_s R_s} \tag{5.7}$$

Measurement Technique

The Van der Paus technique was used to determine the sheet resistance. Hall effect measurements conducted to determine majority carrier type, sheet density and mobility. Measurements were done using Ecopia HMS-3000 Hall measurement system at room temperature. Depending on the resistivity of the sample, a injection current of 1 mA or 1 μA was used. A 1 Tesla (10^4 G) permanent magnet was used for Hall measurements. The sheet resistance was solved numerically via MATLAB.

Chapter 6

Experiments and Results

6.1 Experiments

6.1.1 Experiment 1 - Withdrawal Speed

The first experiment was to determine an optimal withdrawal speed based on crystallinity, porosity and percent transmission over the visible range. Crystallinity is desired for a number of reasons. Firstly, by having a highly oriented crystalline structure, the electrical transport is greatly improved because of increased carrier mobility and limiting grain boundary effects due to improved orientation of crystallites. It is known from chapter 4, that solvent evaporation and organic decomposition will result in pores in the deposited thin film. Finding a withdrawal speed that will deposit a layer thickness that will allow for solvent evaporation and organic decomposition without disturbing the film will result in a denser film with reduced stress or cracks. Lastly, in order to achieve a high FOM, the deposited thin films must exhibit a high degree of transparency. By having a denser film, less light will be scattered, resulting in higher transparency and an improved FOM. Qualitatively speaking, the goal of experiment 1 was optimizing the withdrawal speed to obtain a highly c-axis orientated crystalline film with a porosity less than 15%, RMS surface roughness of 20 nm and transparency $\geq$80% over the visible spectrum.

6.1.2 Experiment 2 - Aluminum Source

Once an optimal withdrawal speed is found, a proper aluminum source must be selected. In experiment 2, three different aluminum sources are used and compared in order to find an optimal aluminum source based on crystallinity, porosity and percent transmission over the visible range. The three aluminum sources used in this work are AlCl, $Al(NO_3)_3$ and $Al_2(SO_4)_3$. All Al sources

had a molar ratio, [Al]/[Zn] = 0.5%. Based on intial findings, it was determined to also try a molar ratio, [Al]/[Zn] = 1% for AlCl. The goal of experiment 2 was to find an optimal aluminum source in the sense that high c-axis oriented crystallinity would be maintained, porosity would be no more than 15% and percent transmission over the visible range to be ≥80%.

6.1.3 Experiment 3 - Additional Treatment

In order to future improve on electrical conductivity, further annealing or treatments in a reduced oxygen partial pressure environment were conducted. As mentioned in chapter 3, the intrinsic defects which contribute to n-type conductivity are oxygen vacancies and zinc interstitials. By performing additional annealing in a reduce oxygen environment, the goal is to increase the conductivity of the thin films by introducing more carriers by creating such defects. Additional treatment was conducted on ZnO and ZnO:Al thin films which showed the best results based on the criteria mentioned in 6.1.2. Three types of additional treatments were conducted: annealing in vacuum, i.e., vacuum growth chamber evacuated, annealing in N_2 at a pressure of 1150 mTorr and annealing under a RF generated N_2 plasma at 1150 mTorr. A pressure of 1150 mTorr was choosen for the RF generated N_2 plasma based on optical emission spectroscopy (OES) measurements. The results are given in Fig. 6.1 where the optical emission peaks for atomic nitrogen are highlighted. The chamber pressure was varied between 300 and 1600 mTorr. The area under the peaks corresponding to atomic nitrogen were calculated using the trapezoidal rule to estimate the area. The atomic nitrogen peak areas for the range of chamber pressures are given in Fig. 6.2. As can be seen from Fig. 6.2, a chamber pressure of 1150 mTorr resulted in the highest atomic nitrogen peaks. N_2 annealing was also done at 1150 mTorr to do a direct comparison between simply annealing in an N_2 environment or if an RF generated N_2 plasma would yield better results. Results again are being based on crystallinity, porosity, percent transmission in the visible range and electrical conductivity. All treatments were conducted at a temperature of 500^{o}C for a duration of 1 hour.

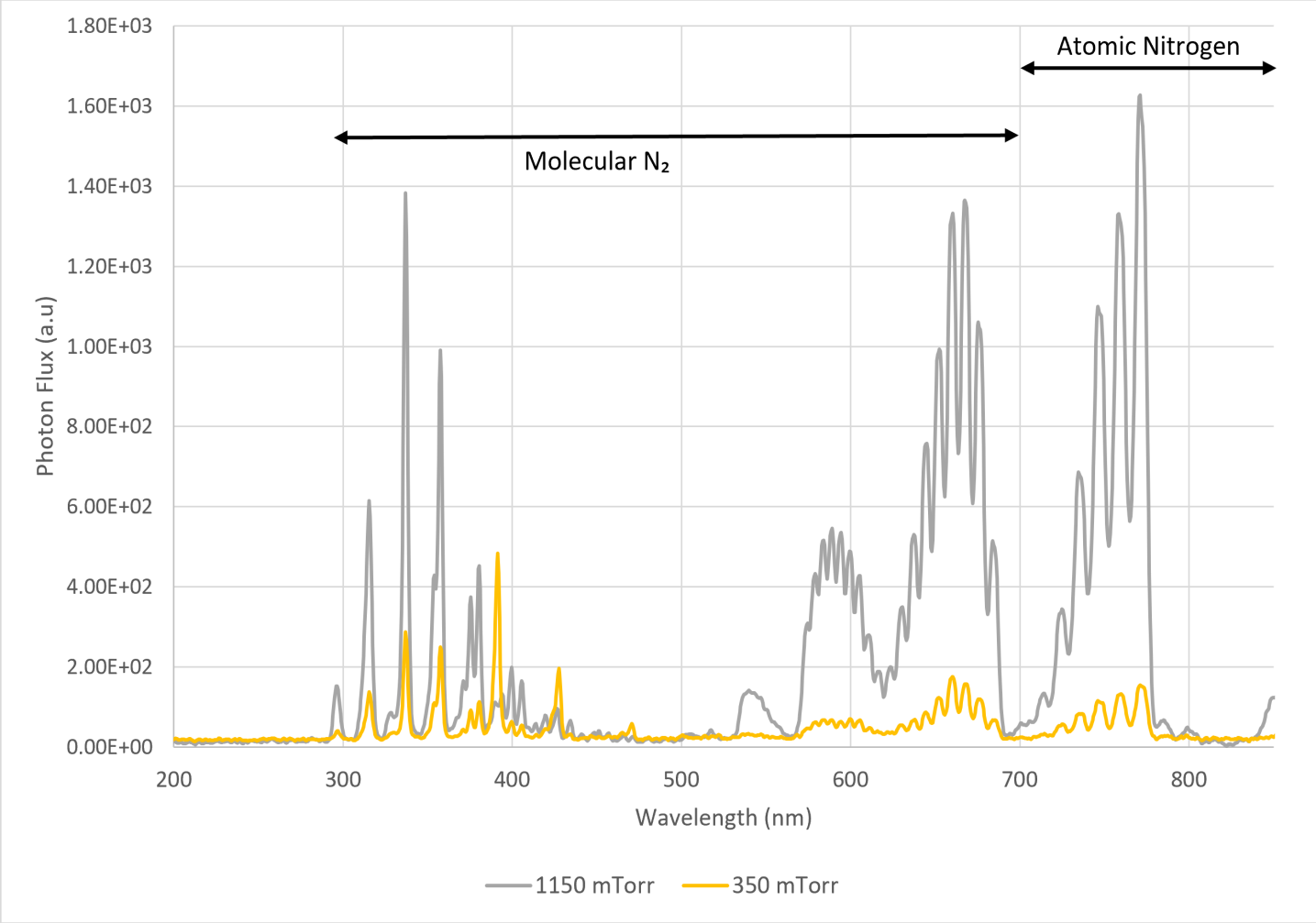

Figure 6.1: Sample OES spectra for chamber pressures of 350 and 1150 mTorr.

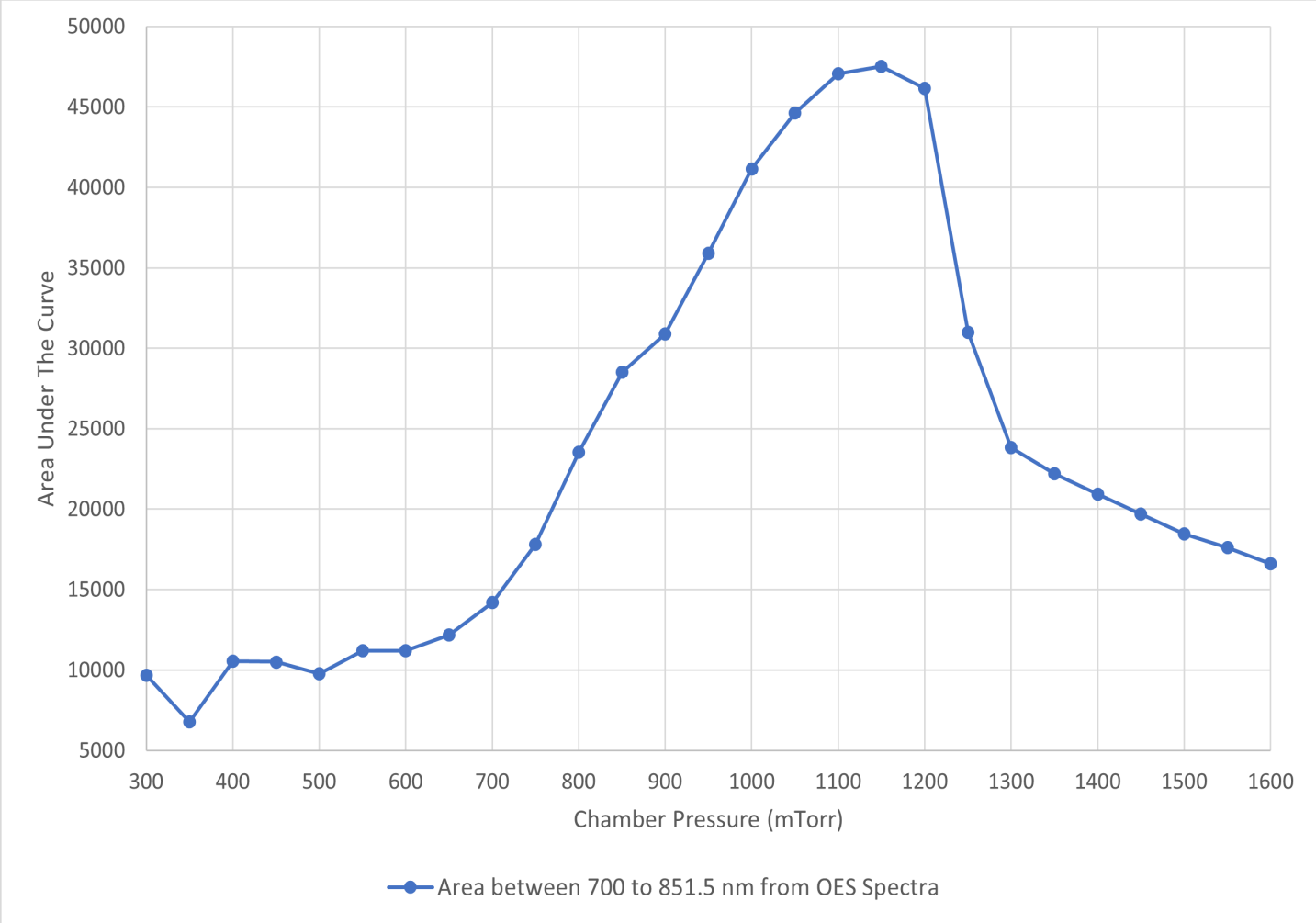

Figure 6.2: Area between 700 to 851.5 nm corresponding to atomic nitrogen optical emission peaks

6.2 Results

6.2.1 Withdrawal Speed Compare

This section contains the results of the withdrawal speed comparison. The XRD spectra are given. SEM images of deposited ZnO thin films are given as well as the trend for percent porosity with increase in withdrawal speed. In addition to SEM images, AFM images are also presented and the trend of RMS surface roughness with increase in withdrawal speed. Lastly, transmission spectra from UV-Vis measurements as well as the trend for percent transmission with increase in withdrawal speed.

Structural Analysis

Fig. 6.3 illustrates the XRD crystallographic peak trends with withdrawal speed. Only a range between 30 and 40 2θ is shown as this is where the prominent peaks for ZnO are located. The peaks are labeled accordingly in Fig. 6.3. AS can be seen in Fig. 6.3, all films exhibit a highly preferential c-axis orientation. The intensity of the (002) ZnO peak increases from the slowest withdrawal speed of 0.625 cm/min to a maximum peak intensity at 2.5 cm/min. After which, further increase in withdrawal speed results in a decrease in (002) ZnO peak intensity to a minimum at 10 cm/min. Further increase in withdrawal speed to 17.5 cm/min results in an increase in withdrawal speed. However, the maximum peak intensity at 17.5 cm/min is still less than at 2.5 cm/min. In addition, (100) and (101) orientations of ZnO begin to appear at 10 cm/min and increase in intensity with increase in withdrawal speed.

Morphological Analysis

Fig. 6.4 illustrates SEM images of the surface and respective cross-section of the deposited ZnO thin films at 2.5 and 15 cm/min, in order to reduce the number of images while still illustrating the trend of porosity with increased withdrawal speed. Fig. 6.5 illustrates the image processing done in ImageJ to estimate the percent porosity of the films at different withdrawal speeds. Fig. 6.6 illustrates the trend of percent porosity with increase in withdrawal speed. Fig. 6.7 illustrates AFM images of the surface of the deposited ZnO thin films at 2.5, 10 and 15 cm/min, in order to reduce the number of images while still illustrating the trend of surface roughness with increased withdrawal speed. Fig. 6.8 illustrates the trend of RMS surface roughness with increase in withdrawal speed.

From Fig. 6.4, it is clear that a slower withdrawal speed of 2.5 cm/min, a denser film is obtained compared to a faster withdrawal speed of 15 cm/min. At 15 cm/min, the deposited ZnO film appears to consist of a porous network of particles while at 2.5 cm/min, it appears that the particles are more closely packed together resulting in a denser film after sintering. Larger area SEM images of the surfaces at various withdrawal speeds were also taken to estimate porosity. Fig. 6.5 illustrates a sample of the image processing done on films deposited at 2.5 and 15 cm/min. Using ImageJ, the percent area of the pores in the images was estimated based on the dark areas in the image. From Fig. 6.6, it is apparent that the percent porosity or percent area of pores in

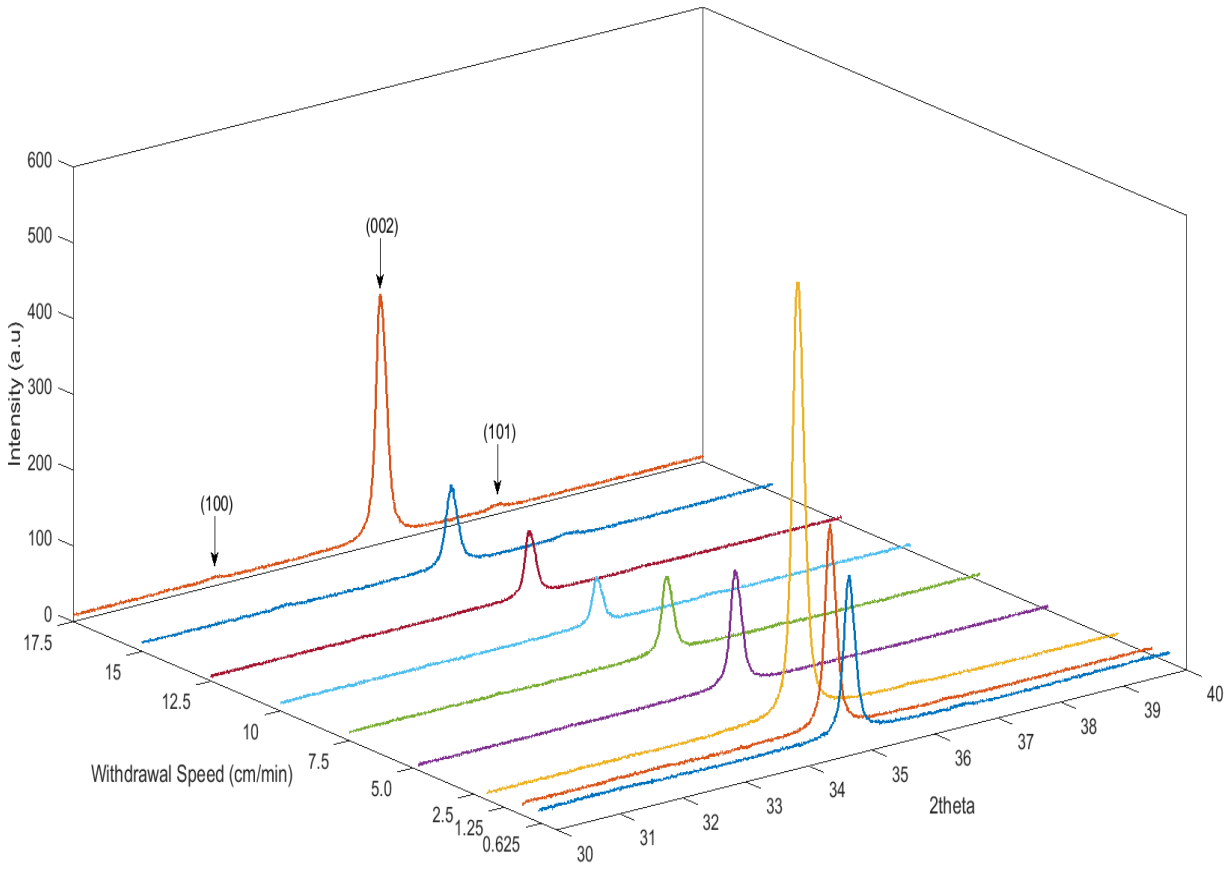

Figure 6.3: Withdrawal speed compare XRD plot

image increases with increase in withdrawal speed. A minimum percent porosity of 7.9% was achieved at 0.0625 cm/min and increased in a somewhat linear manner to a maximum percent porosity of 14.1% at 17.5 cm/min

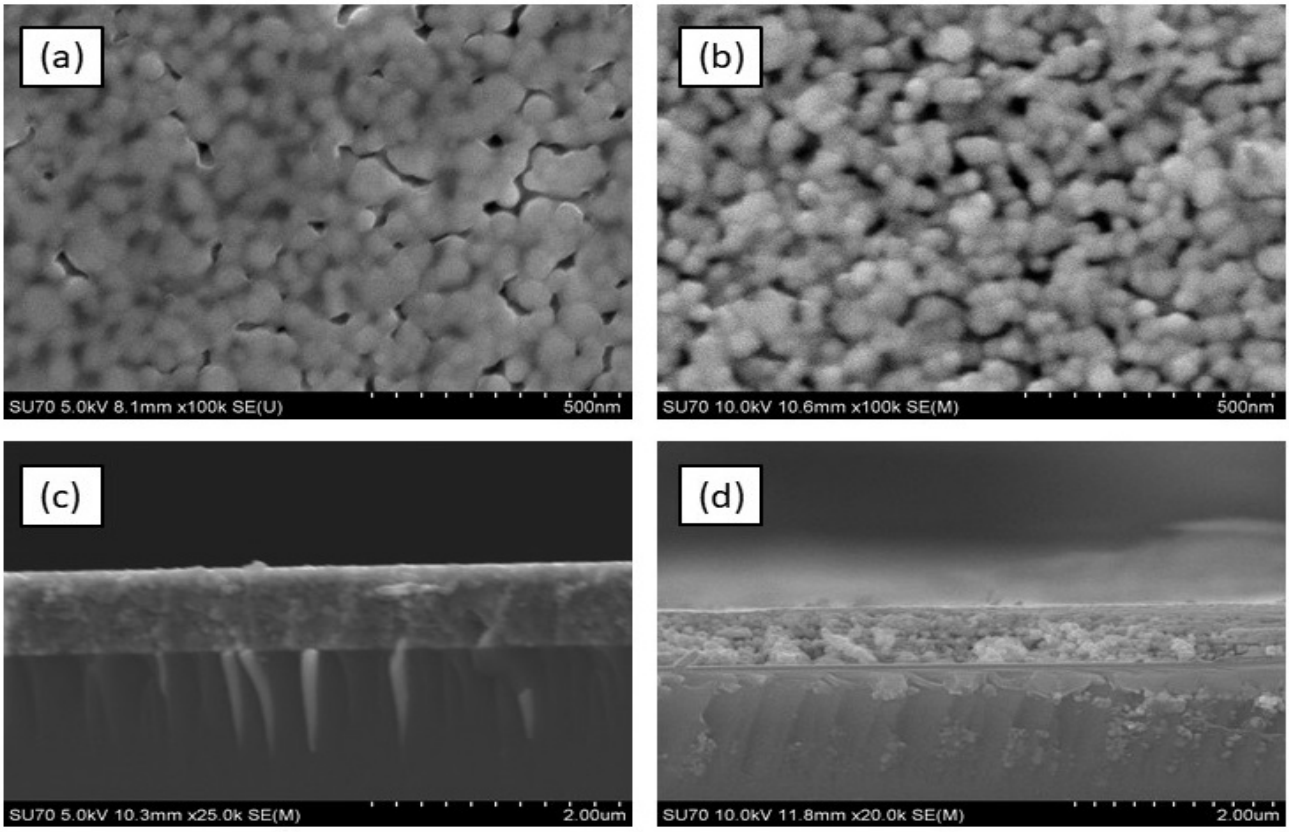

Figure 6.4: Sample SEM images of the surface and respective cross-section of the ZnO thin films prepared at different withdrawal speeds (a) 2.5 cm/min (b) 15 cm/min (c) 2.5 cm/min (d) 15 cm/min

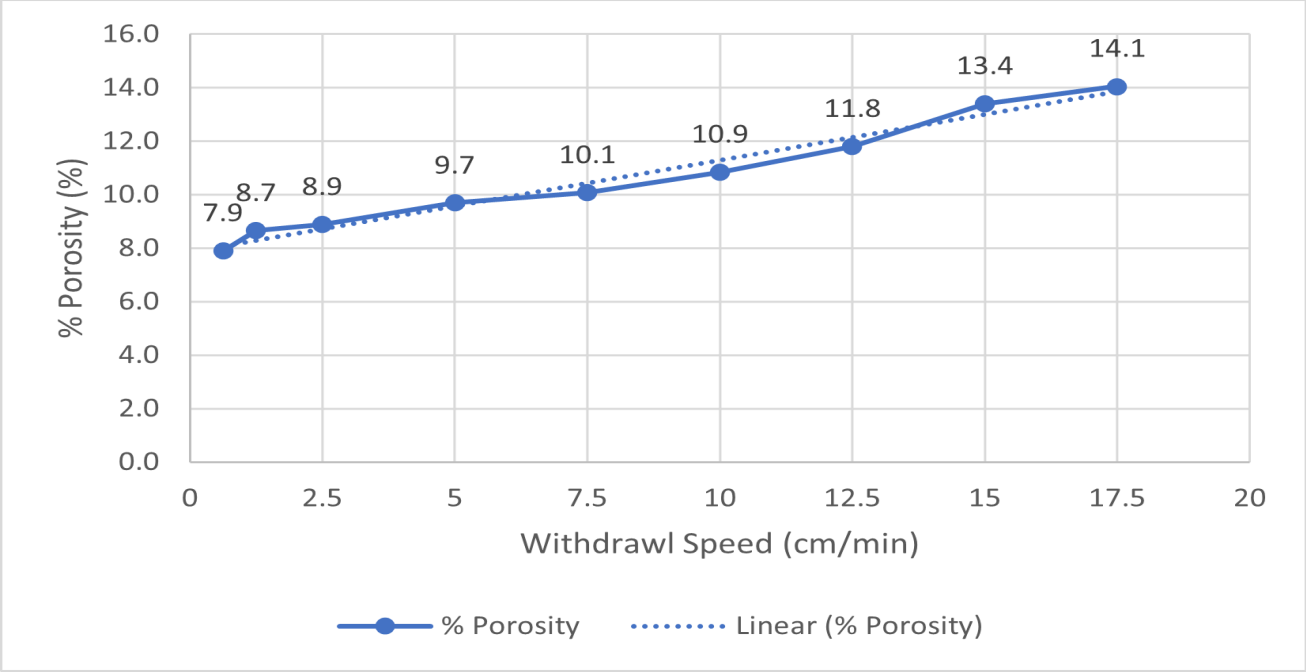

Figure 6.6: Percent Porosity vs withdrawal speed trend

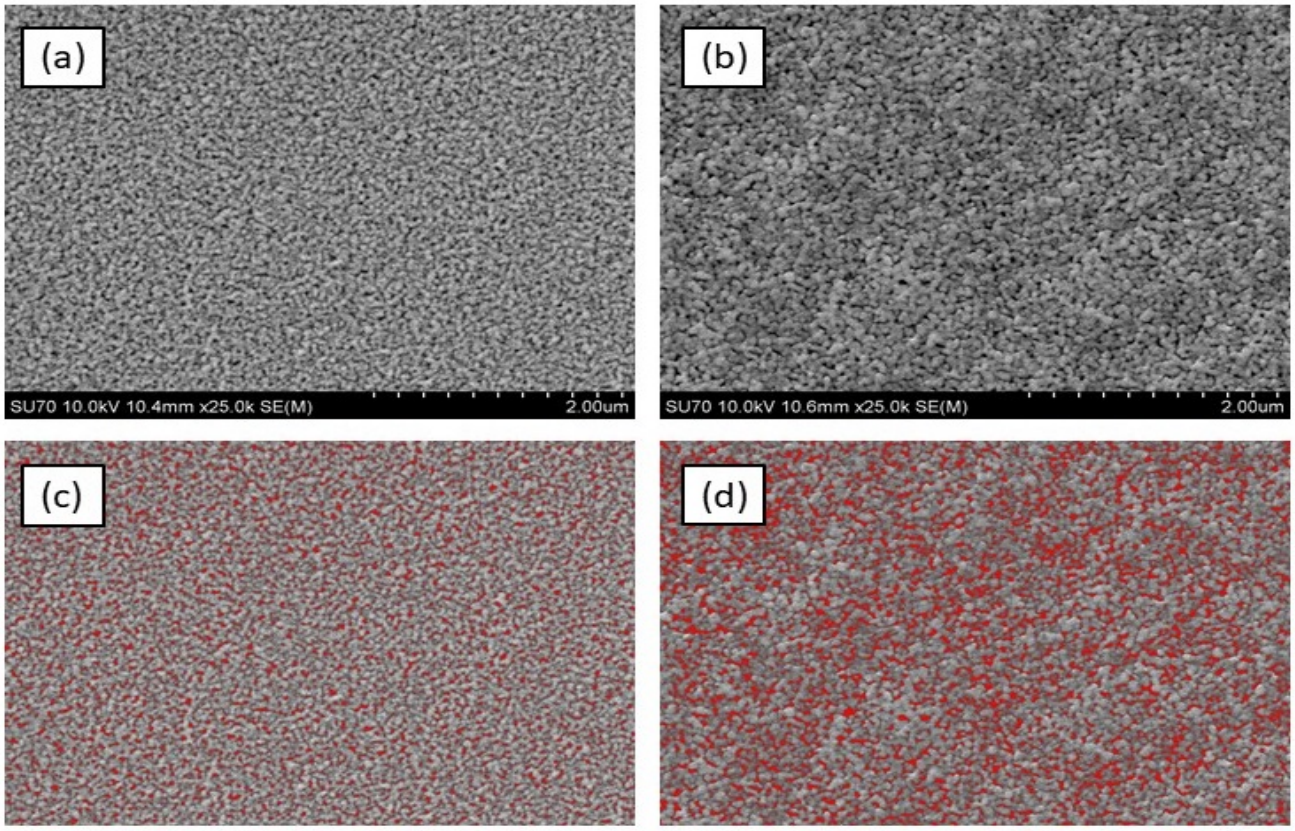

Figure 6.5: Sample SEM images of the surface of the ZnO thin films prepared at different withdrawal speed and images of respective withdrawal speeds after image processing to estimate porosity with pores highlighted in red (a) 2.5 cm/min (b) 15 cm/min (c) 2.5 cm/min (d) 15 cm/min

Fig. 6.7 shows large area scans of the surface of the deposited ZnO films at 2.5, 10 and 15 cm/min. The images reveal a smooth surface at a relatively slow withdrawal speed of 2.5 cm/min. As the withdrawal speed increases, the surface appears to become more rough with worm-like surface features beginning to appear at 15 cm/min. Gwyddion, a software for data visualization and analysis from scanning probe microscopy images was used to calculate the RMS surface roughness of the films at various withdrawal speeds. From Fig. 6.8, which shows the trend of calculated RMS surface roughness with withdrawal speed, the RMS surface roughness is at a minimum of 8.05 nm at 0.625 cm/min and increases some what linearly to a maximum of 29.54 nm at 17.5 cm/min.

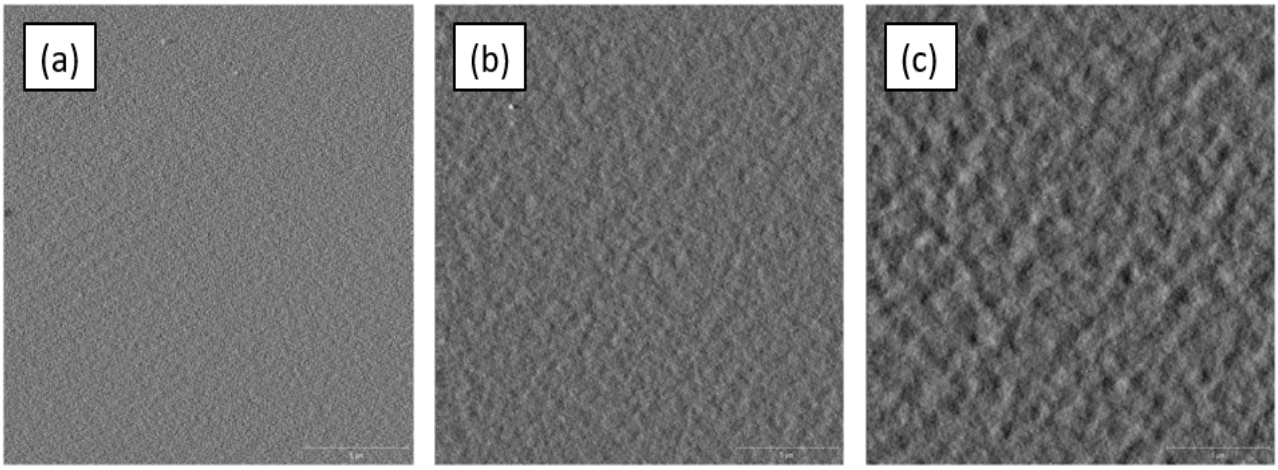

Figure 6.7: Sample AFM images of surface at various withdrawal speeds. a) 2.5 cm/min b) 10 cm/min c) 15 cm/min

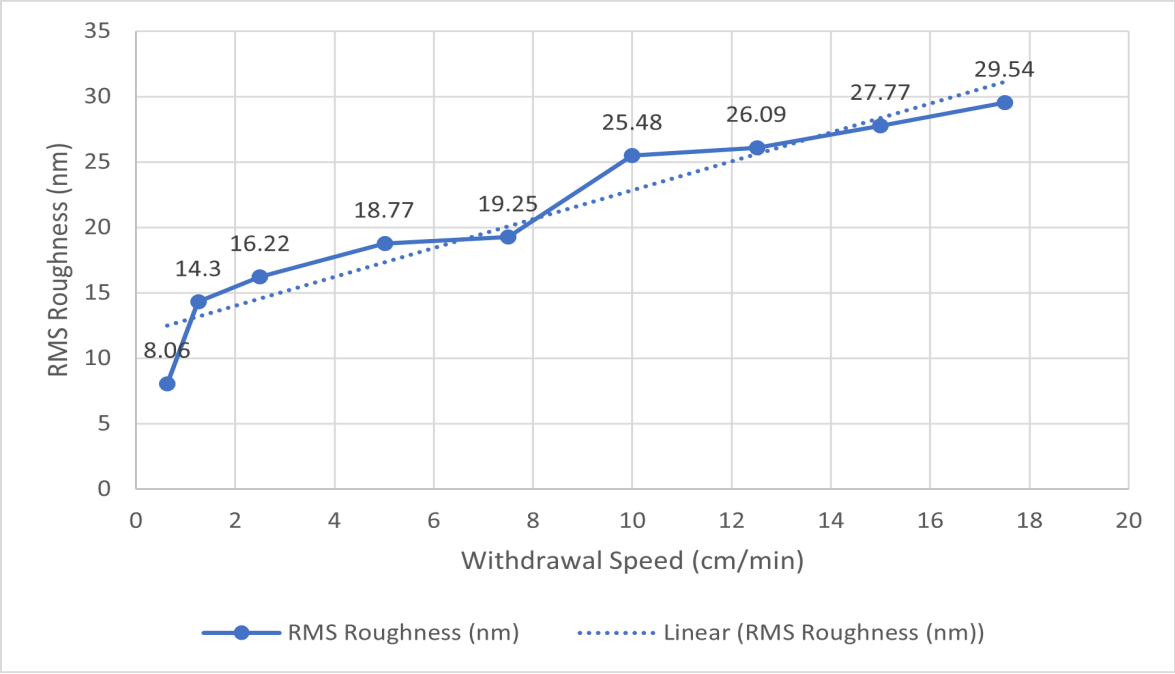

Figure 6.8: RMS surface roughness vs withdrawal speed trend

Optical Analysis

Fig. 6.9 and Fig. 6.10 shows the transmissivity of the ZnO thin films between 0.0625 to 5 cm/min and 7.5 to 17.5 cm/min respectively. Fig. 6.11 illustrates the trend of percent transmission in the visible range (380-750 nm) with increase in withdrawal speed. At slower withdrawal speeds of 0.625 to 5 cm/min, the deposited ZnO films show a consistent and high transmissivity (¿80%) in the visible range. As the withdrawal speed increases from 7.5 to 17.5 cm/min, the transmissivity in the visible range is reduced with thin film interference due to the ZnO-glass-ZnO stack affecting transmissivity. Fig. 6.11 shows the trend of percent transmission over the visible range for the deposited films at various withdrawal speeds. Percent transmission was calculated by averaging the transmissivity over the visible range (380 to 750 nm). From Fig. 6.11, it shows that percent transmission is strongest with a percent transmission of 87% at the slowest withdrawal of 0.0625 and decreases somewhat linearly as withdrawal speed is increasesd to a minimum percent transmission of 68% at 17.5 cm/min. Withdrawal speeds between 0.0625 to 7.5 cm/min all exhibit a high transmissivity (>80%) in the visible range.

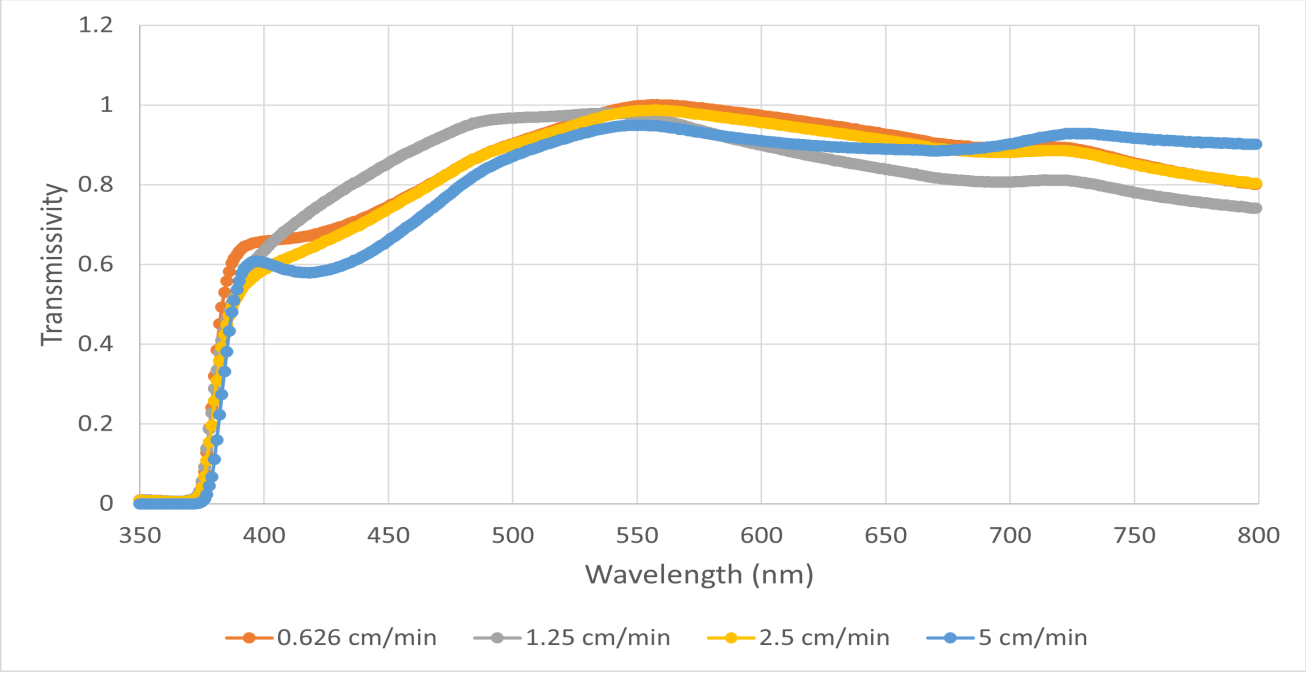

Figure 6.9: Transmission spectrum of withdrawal speeds from 0.625 to 5 cm/min

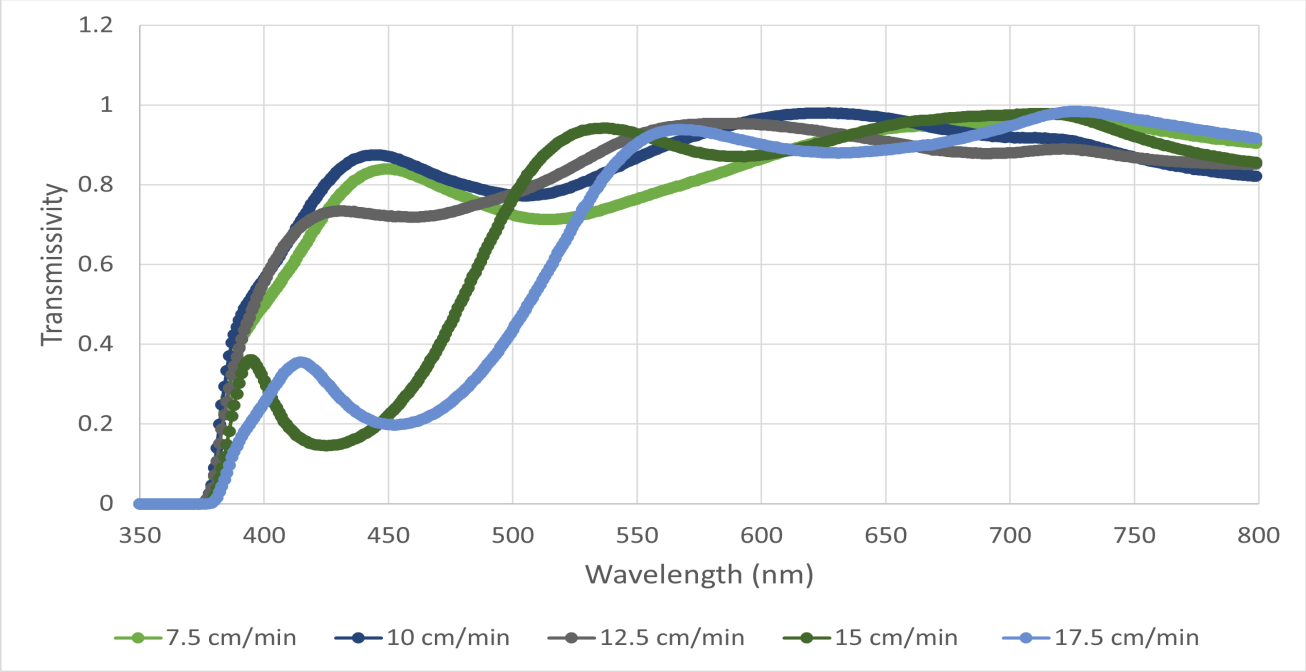

Figure 6.10: Transmission spectrum of withdrawal speeds from 7.5 to 17.5 cm/min

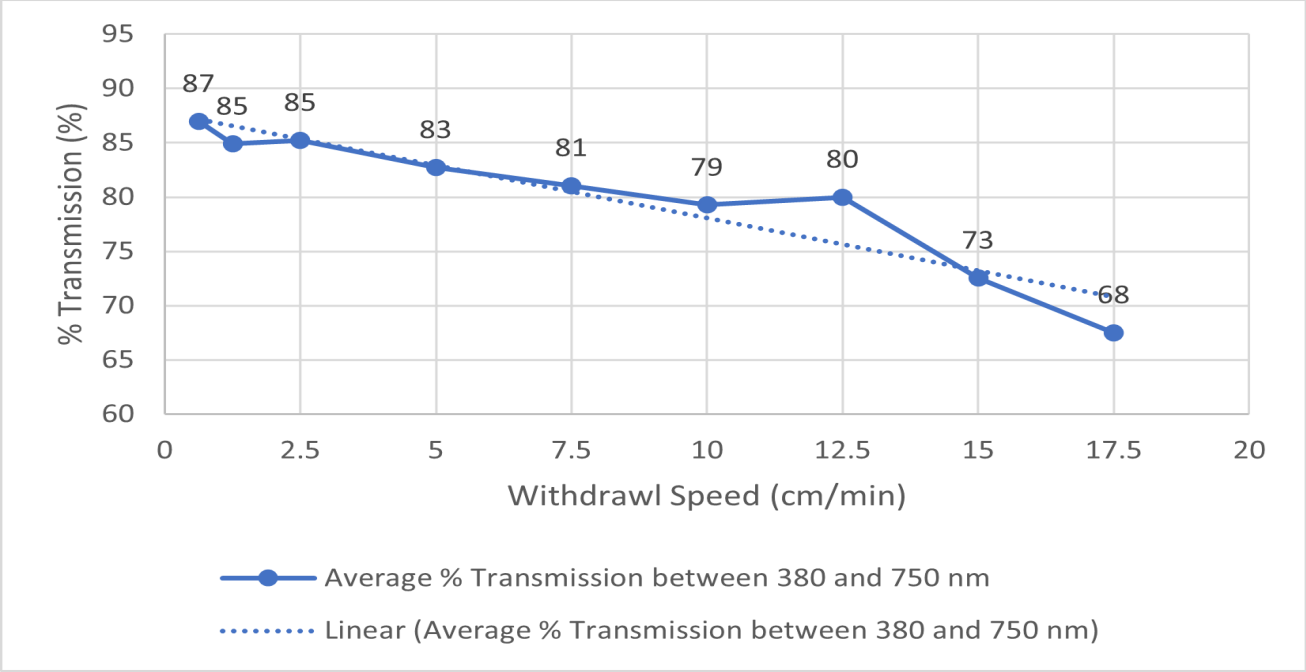

Figure 6.11: Trend of average transmission vs withdrawal speed

Summary

XRD results showed that a withdrawal speed of 2.5 cm/min is optimal for achieving highly preferential c-axis orientation. While it is seen that all withdrawal speeds exhibits preferential c-axis orientation, the highest (002) intensity was achieved at 2.5 cm/min. In addition, faster withdrawal speeds, beginning at 10 cm/min, reveal other crystal orientations of ZnO, namely (100) and (101) becoming more prominent as withdrawal speed is increased further.

SEM and AFM results showed that porosity and surface roughness increase with increase in withdrawal speed. The trends of porosity and surface roughness with increase in withdrawal speed both exhibit a somewhat linear relationship. At 2.5 cm/min, the percent porosity only increases by 1% from 7.9% at 0.0625 cm/min to 8.9% and surface roughness increases by 10.16 nm from 8.06 nm at 0.0625 cm/min to 18.22 nm. At slower withdrawal speeds, the deposited films appear to consist of closely packed particles resulting in a relatively dense film. While at faster withdrawal speeds, the films appear to consist of particles stacked on top of one another resulting in a porous network of particles.

UV-Vis results showed that films at slower withdrawal speeds up to 7.5 cm/min exhibit high transparancy (>80%) in the visible range (380 to 750 nm). Percent transmission in the visible range decreased somewhat linearly with increase in withdrawal speed. At 2.5 cm/min, the films exhibited 85% transparancy in the visible range. Based on these results, it was decided a withdrawal speed of 2.5 cm/min would be used for experiment 2 where aluminum source comparisons were conducted.

6.2.2 Aluminum Source

This section contains the results of comparing various aluminum sources. XRD spectra are given. SEM images of the surfaces of the aluminum doped ZnO thin films are given as well as the percent porosity of the films estimated using ImageJ. Lastly, transmission spectra from UV-Vis measurements as well as the percent transmission between 380 and 750 nm for different aluminum sources. Energy band gap estimates from Tauc plots for the various aluminum sources are also given.

Structural Analysis

Fig. 6.12 illustrates the XRD crystallographic peaks for different aluminum sources used for doping. Only a range between 30 and 40 2θ is shown as this is where the prominent peaks for ZnO are located. The peaks are labeled accordingly in Fig. 6.12. From Fig. 6.12, it can be seen that doping with 0.5% AlCl maintained the highest (002) ZnO peak compared to the undoped ZnO film. Further increase in AlCl doping to 1% reveals a decrease in (002) peak while a peak at approximately 37^o appears corresponding to aluminum oxide in (110) orientation indicating formation of aluminum oxide clusters. 0.5% $Al(NO_3)_3$ exhibited the weakest (002) ZnO peak of all the aluminum sources used. However, still maintained preferential c-axis orientation with no other orientations of ZnO becoming apparent. 0.5% $Al_2(SO_4)_3$ shows a (002) ZnO peak with comparable intensity to 0.5% AlCl. However, like in the scenario with 1% AlCl, a aluminum oxide peak corresponding to (110) orientation is present. In addition to a (110) aluminum oxide peak, a peak at approximately 34^o is present corresponding to aluminite in (240) orientation.

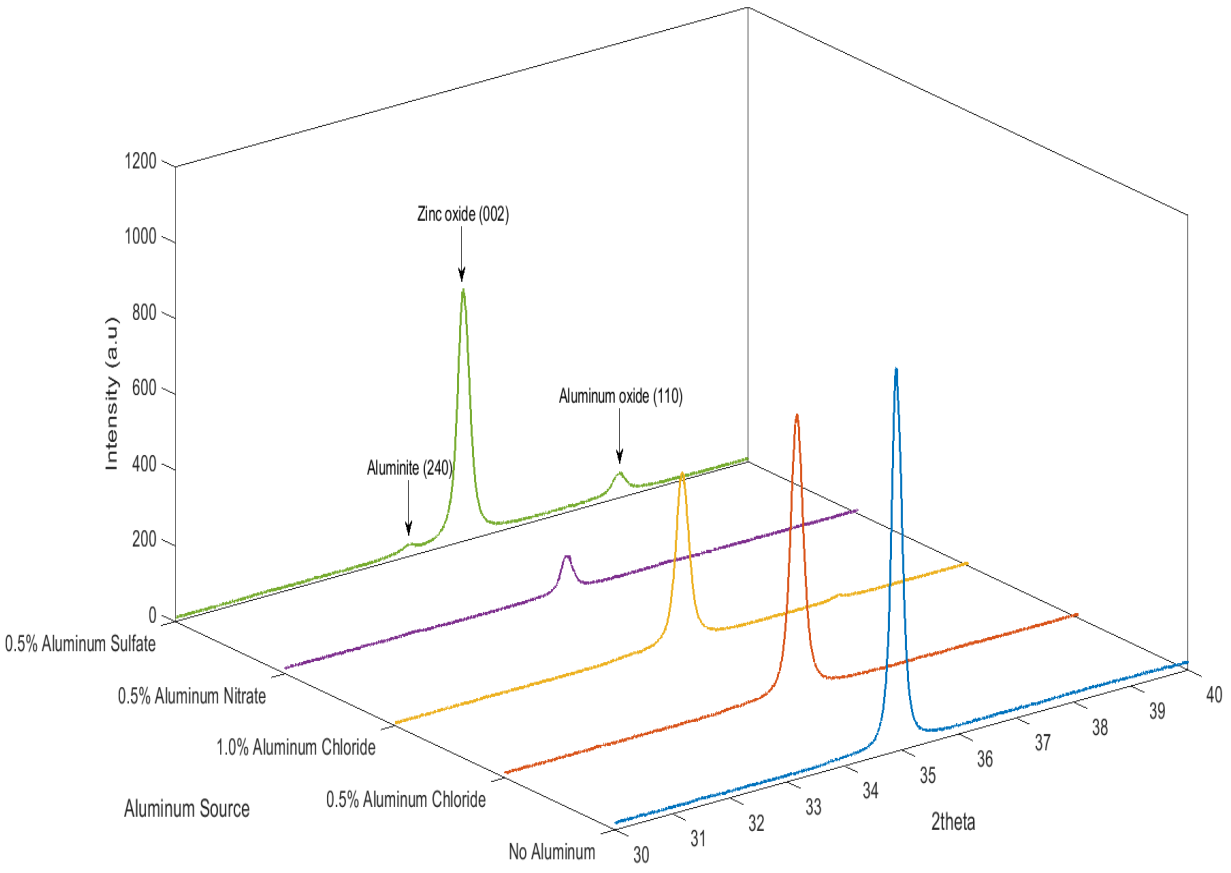

Figure 6.12: Aluminum source compare XRD plot

Morphological Analysis

Fig. 6.13 illustrates the SEM images of the surface of the aluminum doped ZnO thin films using various aluminum sources. Fig. 6.14 shows the estimated percent porosity using ImageJ for the different aluminum sources. From Fig. 6.14, it can be seen that the lowest porosity was achieved with 0.5% $Al(NO_3)_3$. The porosity was estimated to be slightly lower at 8.8% compared to 8.9% for the undoped ZnO films. However, due to the subjective nature of choosing which shade of pixels are considered as pores, this can not be definite. 0.5% AlCl shows a calculated percent porosity of 9.0% which increased to 11.1% with increased AlCl concentration of 1%. 0.5% $Al_2(SO_4)_3$ exhibited a percent porosity of 9.5%.

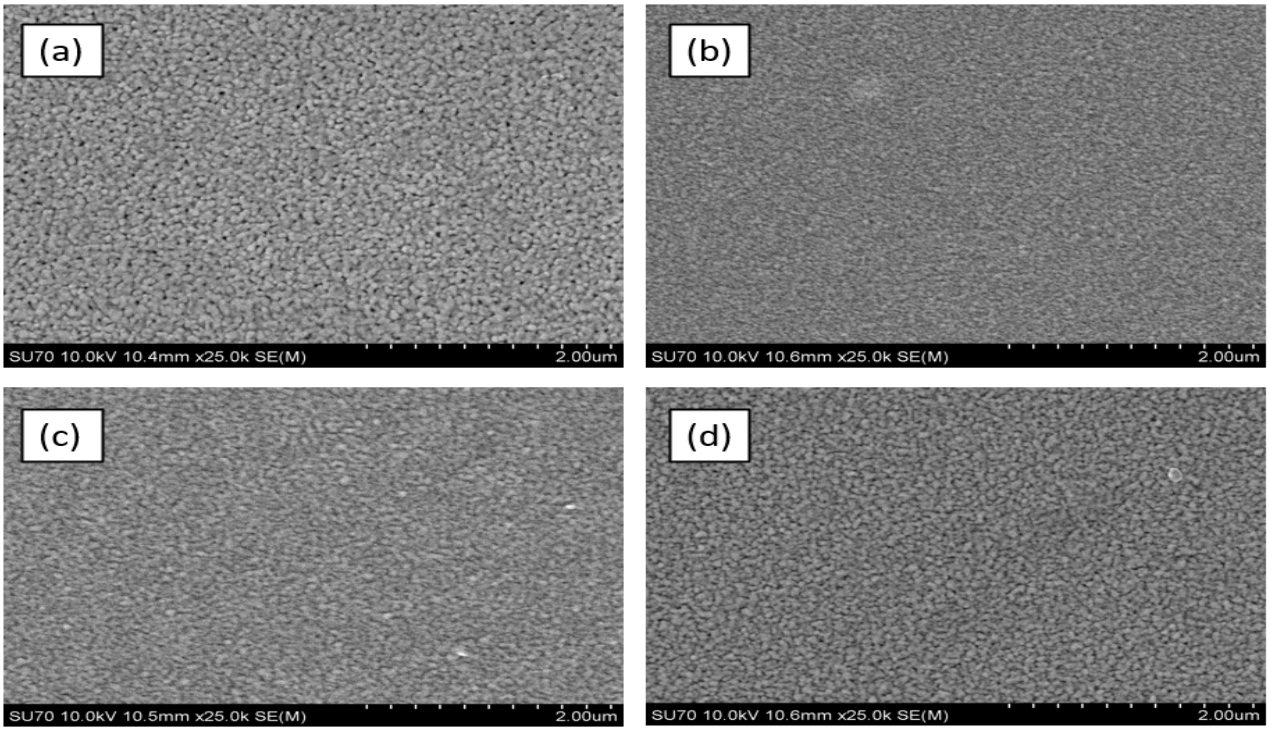

Figure 6.13: SEM images of the surface of ZnO thin films prepared with different aluminum sources and concentrations (a) 0.5% AlCl (b) 1% AlCl (c) 0.5% $Al(NO_3)_3$ (d) 0.5% $Al_2(SO_4)_3$

Optical Analysis

Fig. 6.15 shows the UV-Vis transmission spectra for different aluminum sources. The average percent transmission between 380 and 750 nm has been tabulated in Table 6.1. The band gap has been estimated using the Tauc plot method and is illustrated in Fig. 6.16. All of the aluminum doped ZnO thin films exhibit a transparency >75% in the visible range (380 to 750 nm). 0.5% AlCl doped film had the closest transparency (84.79%) to the undoped ZnO film (85.43%) with transparency decreasing to 82.64% with increased AlCl concentration to 1%. Films doped with 0.5% $Al(NO_3)_3$ and 0.5% $Al_2(SO_4)_3$ showed a transparency of 80.08% and 78.17% respectively. In regards to estimated band gaps using Tauc plots, the undoped ZnO film has a band gap of approximately 3.323 eV. In the AlCl doped samples, the band gap was 3.314 eV and 3.332 eV for 0.5% and 1% AlCl doped samples respectively. For 0.5% $Al(NO_3)_3$ doped sample, the band gap was estimated to be 3.368 eV and for the 0.5% $Al_2(SO_4)_3$ doped sample, the band gap was 3.34 eV.

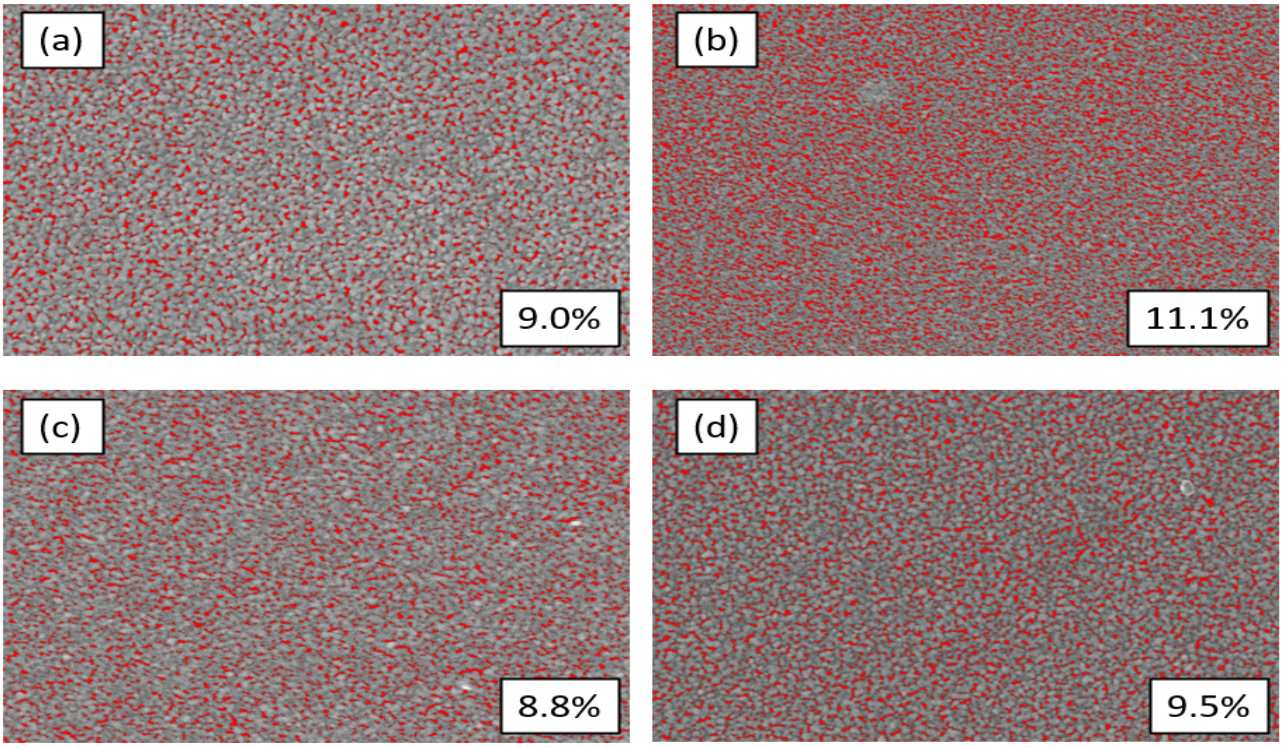

Figure 6.14: SEM images of the surface of ZnO thin films prepared with different aluminum sources and concentrations after imagine processing to estimate porosity with pores highlighted in red. The percent porosity is given in the bottom right hand corner of each respective image (a) 0.5% AlCl (b) 1% AlCl (c) 0.5% $Al(NO_3)_3$ (d) 0.5% $Al_2(SO_4)_3$

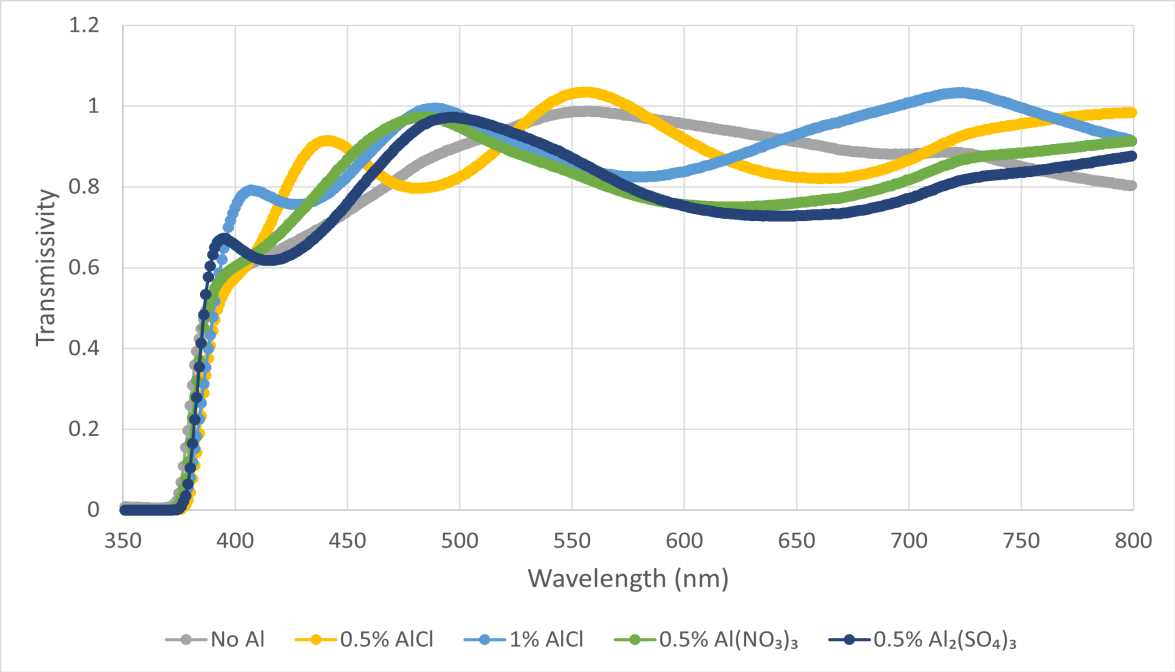

Figure 6.15: Transmission spectrum of different aluminum sources and concentrations

Table 6.1: Average percent transmission of different aluminum sources and concentrations between 380 and 750 nm

No Al	0.5% AlCl	1% AlCl	0.5% $Al(NO_3)_3$	0.5% $Al_2(SO_4)_3$
85.43%	84.79%	82.64%	80.08%	78.17%

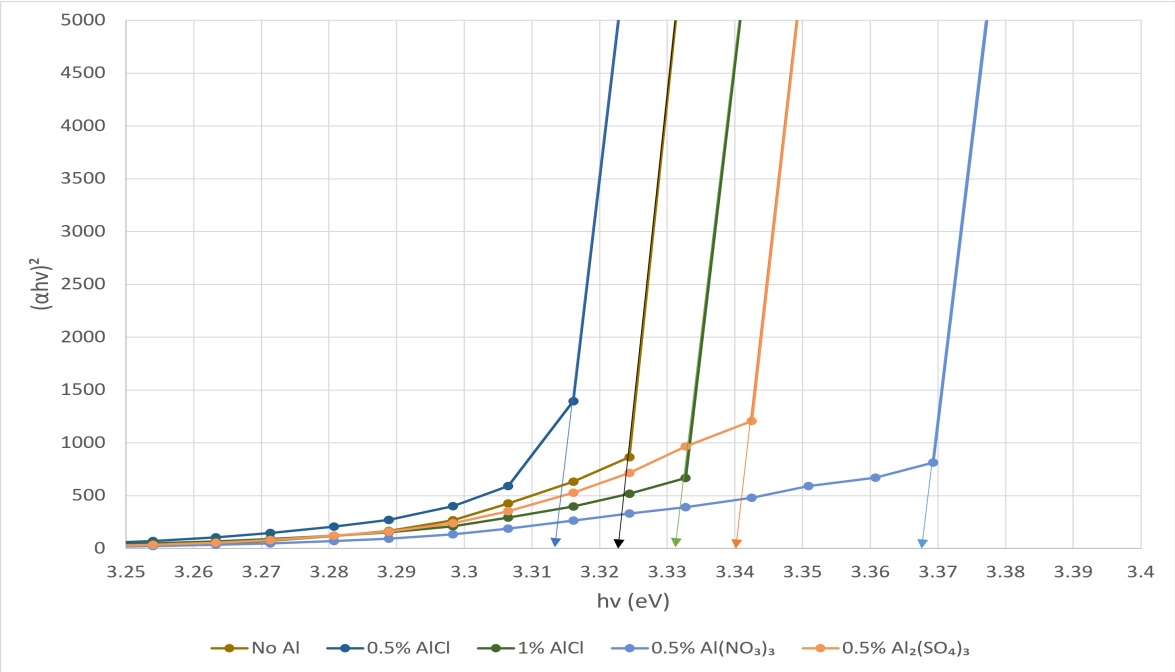

Figure 6.16: Tauc plot of different aluminum sources with arrows indicating band gap

Summary

Based on XRD results, samples doped with 0.5% AlCl exhibited the best qualities. The (002) ZnO peak was the most intense compared to the other aluminum sources used indicating highly c-axis oriented crystallites. Increasing the AlCl concentration to 1% resulted in aluminum oxide in (110) orientation indicating the additonal Al did not substitute Zn lattice sites but instead formed aluminum oxide. Samples with 0.5% $Al(NO_3)_3$ showed the weakest (002) ZnO peak, however was c-axis preferential. 0.5% $Al_2(SO_4)_3$ exhibited the worst results with not only showing aluminum oxide in (110) orientation but also aluminite in (240) orientation. Regarding SEM results, all samples exhibited comparable porosity to the undoped films and porosity increasing

with increase in AlCl concentration. The transparency or percent transmission in the visible range of all the samples were >75%. The 0.5% AlCl doped sample had the closest transparency to the undoped ZnO film. Regarding band gap estimates, the undoped ZnO sample had a band gap of 3.323 eV. When doped with 0.5% AlCl, the band gap decreased to 3.314 eV. Increasing the AlCl concentration to 1% resulted in a band gap increase to 3.332 eV. For $Al(NO_3)_3$ and 0.5% $Al_2(SO_4)_3$ doped films, the band gap was estimated to 3.368 eV and 3.34 eV respectively. Based on these results and the fact that the sample doped with 0.5% AlCl exhibited the highest c-axis oriented crystallinity, similar porosity and transparency compared to the undoped ZnO sample. It was decided that for experiment 3, where additional treatments were going to be conducted, only the 0.5% AlCl doped sample along with the undoped ZnO sample would be used.

6.2.3 Additional Treatment

This section contains the results of comparing various additional treatments conducting on 0.5% AlCl doped and undoped ZnO thin films. Based on crystallinity, porosity and percent transmission (transparency) results from 6.2.2, addional treatments were conducted on ZnO films with no aluminum doping and 0.5% Al using AlCl. XRD spectra are given. SEM images of the surfaces of the treated thin films are given as well as the percent porosity of the films estimated using ImageJ. Transmission spectra from UV-Vis measurements as well as the percent transmission between 380 and 750 nm for different treatments. Energy band gap estimates from Tauc plots for the various treatments are also given. Lastly, the electrical properties from Hall measurements is given. As mentioned in 6.1.3, the treatments were conducted at 500^oC and for a period of 1 hour. Treatments consisted of either annealing in a vacuum environment, in an N_2 environment at 1150 mTorr or in the presence of an RF generated N_2 plasma.

Structural Analysis

Figs. 6.17 - 6.19 illustrate the XRD spectra of the treated samples. In Fig. 6.17, the (002) ZnO intensity decreases after all the different treatments on the undoped film. For the samples annealing in vacuum and N_2, there is only a minor decrease in peak intensity. For the sample annealing in N_2 plasma, the (002) peak intensity is greatly reduced. Similarly, in Fig. 6.18, (002) ZnO intensity decreases after all the different treatments on the films doped with 0.5% AlCl. The sample annealed in N_2 exhibited the least decrease in (002) peak intensity. Interestingly, the

N_2 plasma did not have as large of an effect on the peak intensity on the AlCl doped sample compared to the undoped sample. Fig. 6.19 shows that when untreated, the AlCl doped sample has the (002) peak shifted to a higher angle. After additional treatments, the peak shifts to a lower angle, lining up with the undoped ZnO (002) peak.

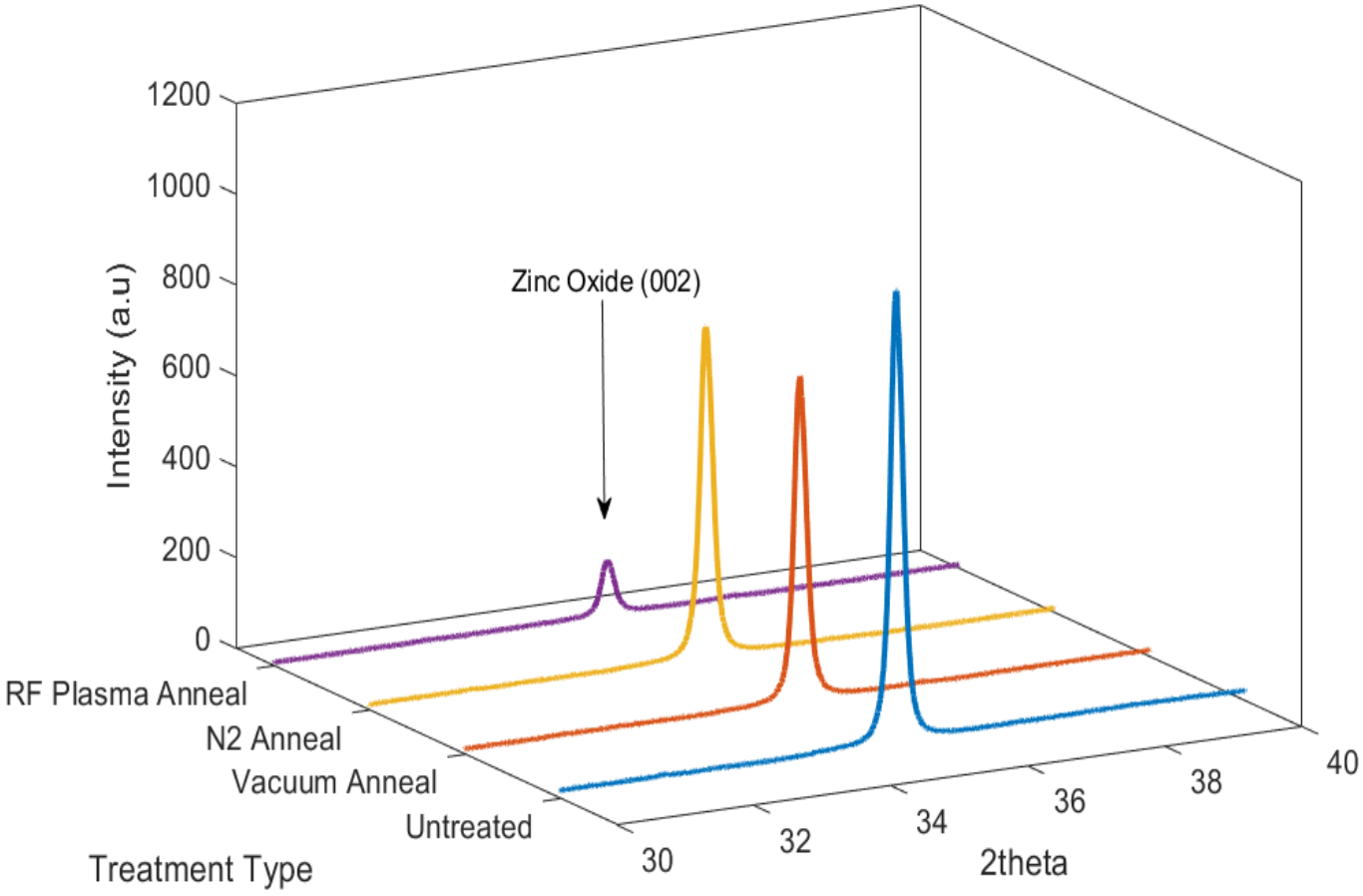

Figure 6.17: Treatment compare no Al doping XRD plot

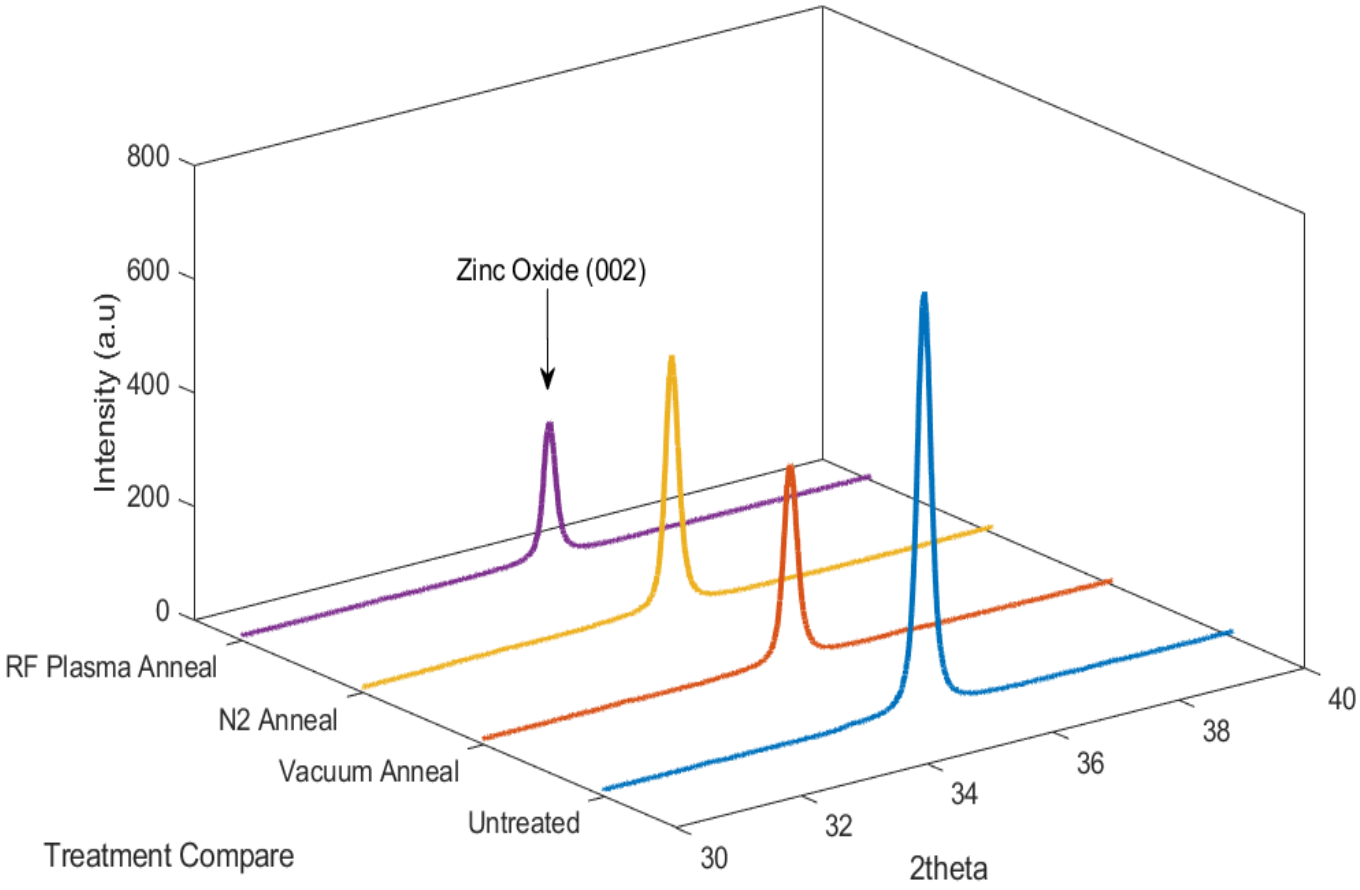

Figure 6.18: Treatment compare using 0.5% AlCl XRD plot

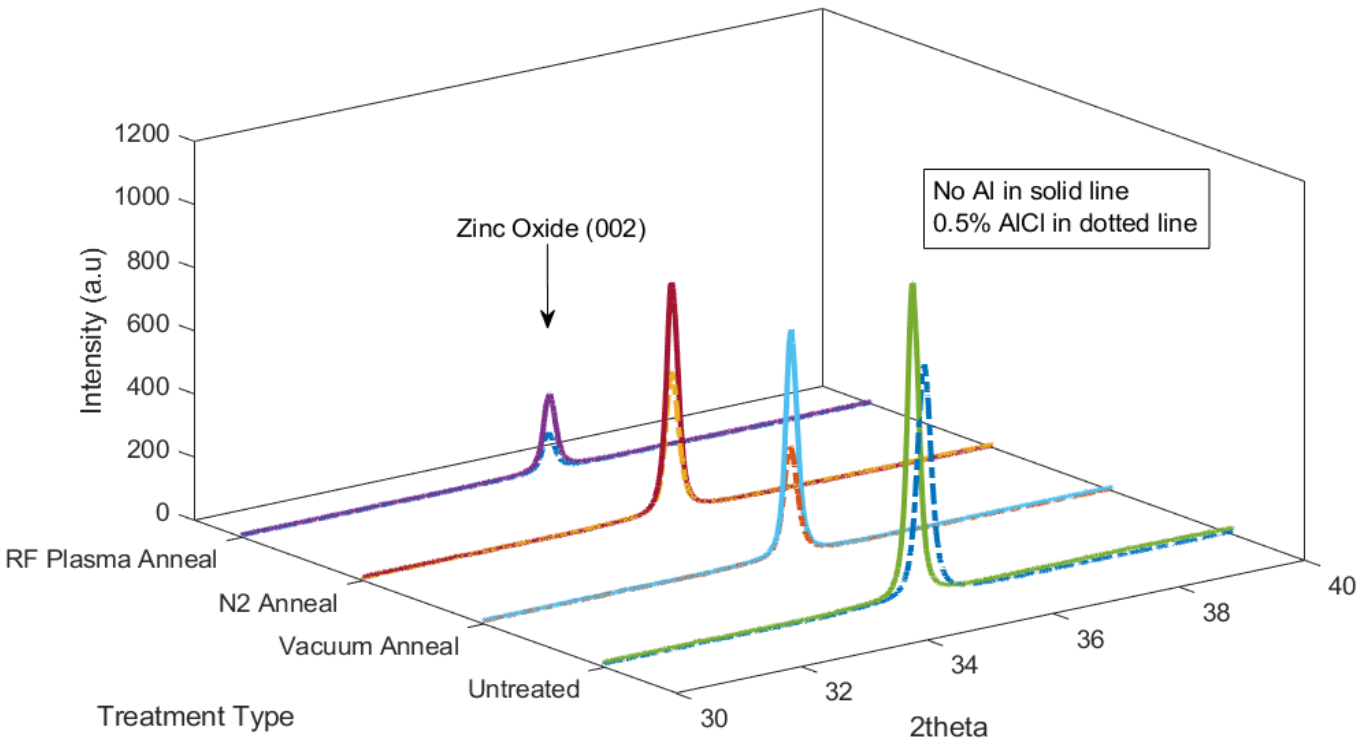

Figure 6.19: Combined treatment compare XRD plot

Morphological Analysis

Fig. 6.20 and Fig. 6.22 show large area SEM images of the surfaces of treated undoped and 0.5% AlCl doped samples respectively. Fig. 6.21 and Fig. 6.23 show the porosity estimates using ImageJ of treated undoped and 0.5% AlCl doped samples respectively. Both annealing in vacuum environment as well as in N_2 result in reduced porosity for both undoped and doped samples. For undoped ZnO, annealing in vacuum reduced porosity to 6.8% and annealing in N_2 reduced the porosity to 5.6%. For the AlCl doped ZnO, annealing in vacuum reduced the porosity to 6% and annealing in N_2, the porosity was reduced to 6.1%. In the case of annealing in N_2 plasma, the porosity for the undoped sample increased to 7.5%. While for the AlCl doped sample, the porosity was further reduced to 4.2%.

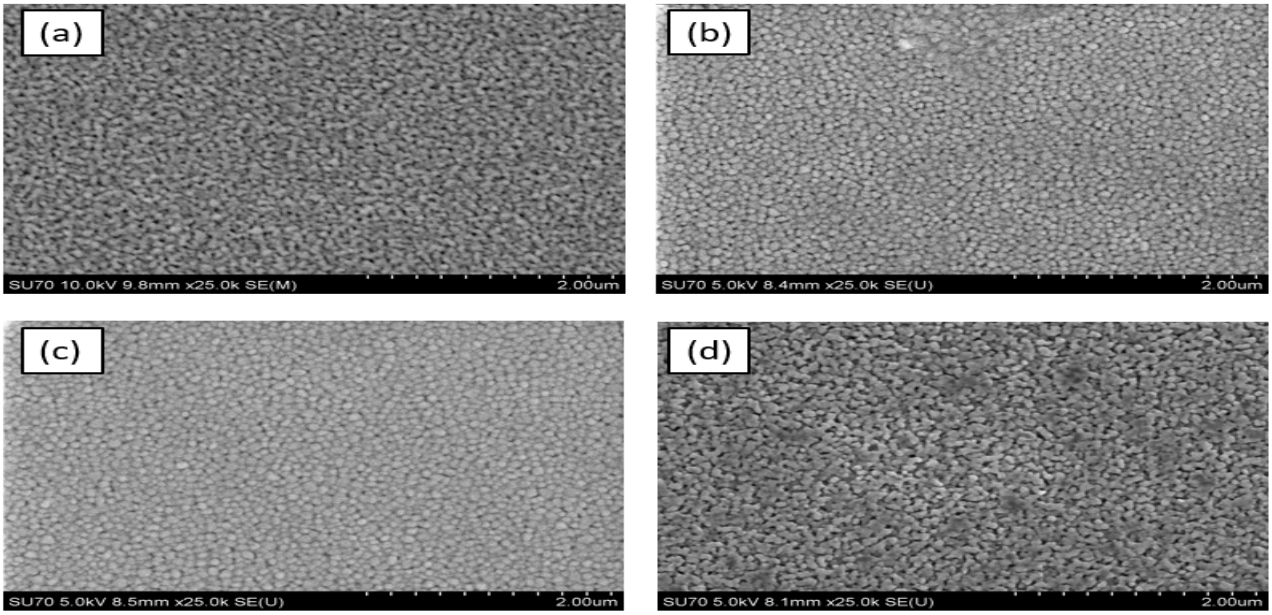

Figure 6.20: SEM images of surface of samples with no aluminum doping after various treatments. a) no treatment b) 1hr vacuum anneal c) 1hr N_2 anneal d) 1hr N_2 RF plasma anneal

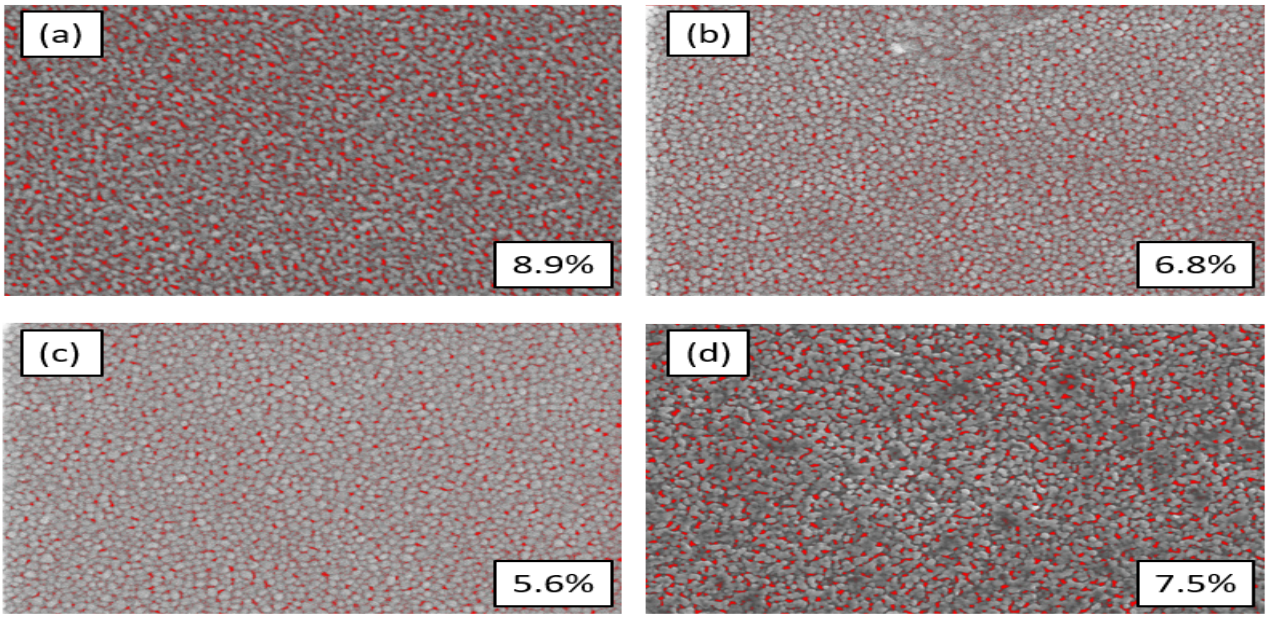

Figure 6.21: Percent porosity of SEM images of surface of samples with no aluminum doping after various treatments with percent porosity indicated in respective image. a) no treatment b) 1hr vacuum anneal c) 1hr N_2 anneal d) 1hr N_2 RF plasma anneal

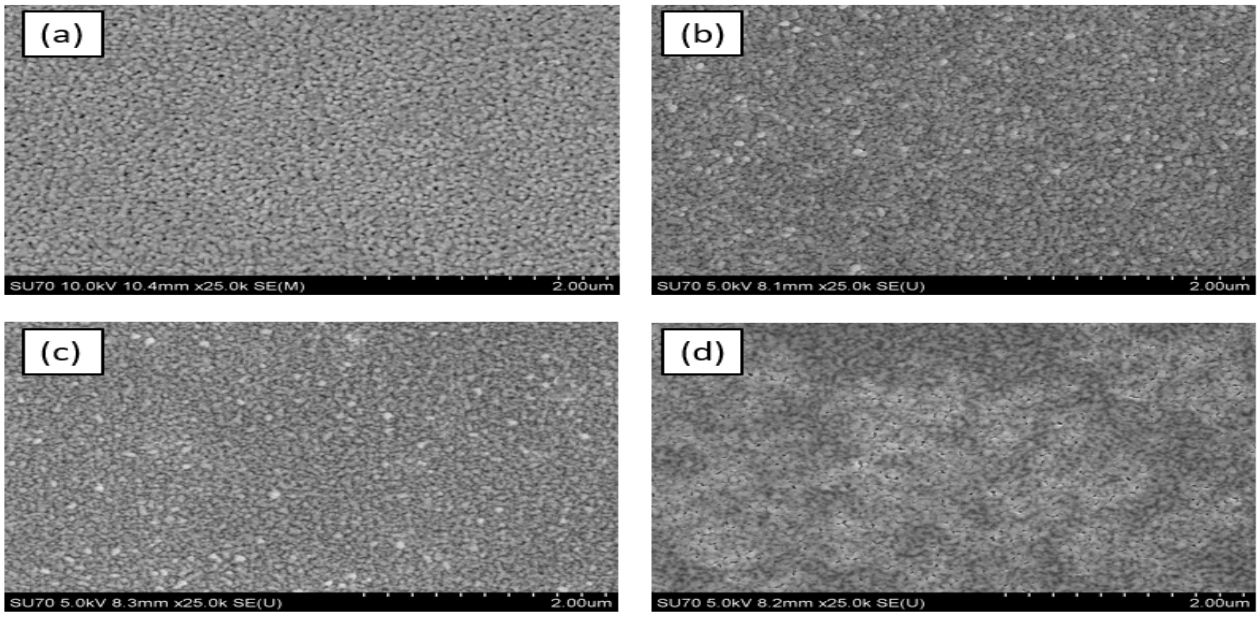

Figure 6.22: SEM images of surface of samples with 0.5% AlCl doping after various treatments. a) no treatment b) 1hr vacuum anneal c) 1hr N_2 anneal d) 1hr N_2 RF plasma anneal

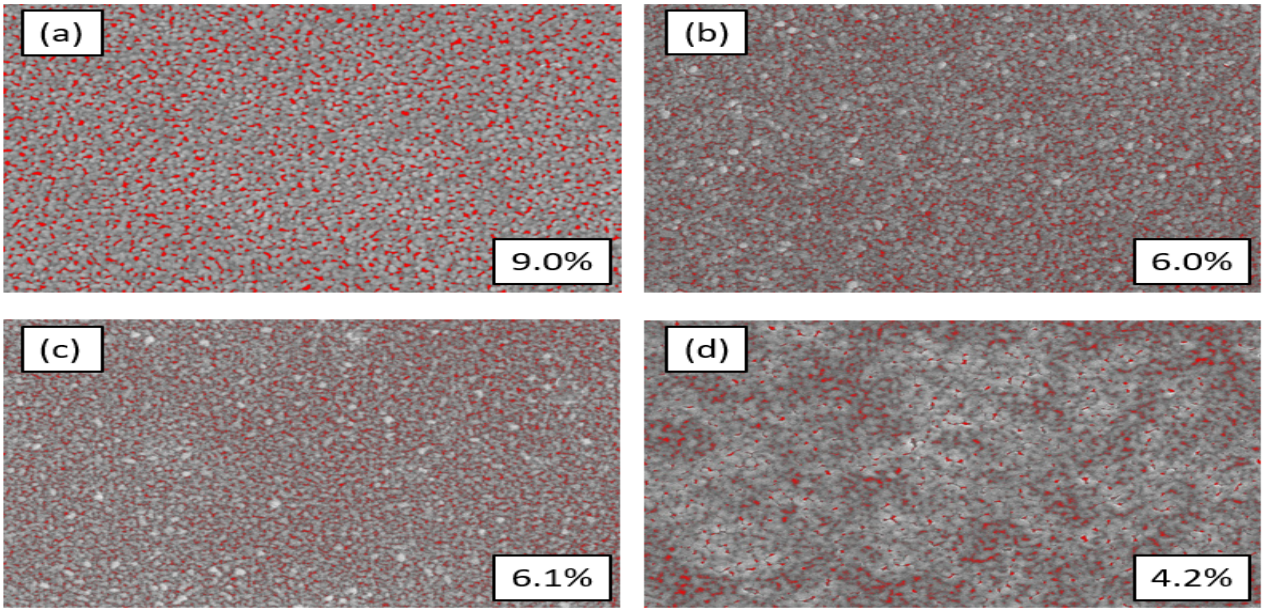

Figure 6.23: Percent porosity of SEM images of surface of samples with 0.5% AlCl doping after various treatments with % porosity indicated in respective image. a) no treatment b) 1hr vacuum anneal c) 1hr N_2 anneal d) 1hr N_2 RF plasma anneal

Optical Analysis

Figs. 6.24 - 6.25 shows the UV-Vis transmission spectra for different aluminum sources after various treatments. The average percent transmission for all spectra between 380 and 750 nm has been tabulated in Table 6.2. The band gap for different aluminum sources after various treatments has been estimated using the Tauc plot method and is illustrated in Figs. 6.26 - 6.27. For the undoped ZnO, the transparency over the visible range was reduced to around 79% regardless of treatment type. In regards to 0.5% AlCl doped samples, the vacuum and N_2 annealed samples saw an increase in transparency with a maximum of 85.53% for the sample annealed in N_2. While for the sample treated in N_2 plasma, there was a reduction in transparency to 83.45%. Regarding Tauc plots and band gap estimates, the band gap for the undoped ZnO samples saw an increase in band gap energy for treatment done in vacuum and N_2. However, the band gap was reduced to below the untreated ZnO band gap for the sample treated in N_2 plasma. The sample treated in vacuum saw the largest band gap of 3.358 eV. For the samples doped with AlCl, the band gap increased for all treatment methods compared to the untreated sample. The sample treated in N_2 saw the largest band gap of 3.341 eV.

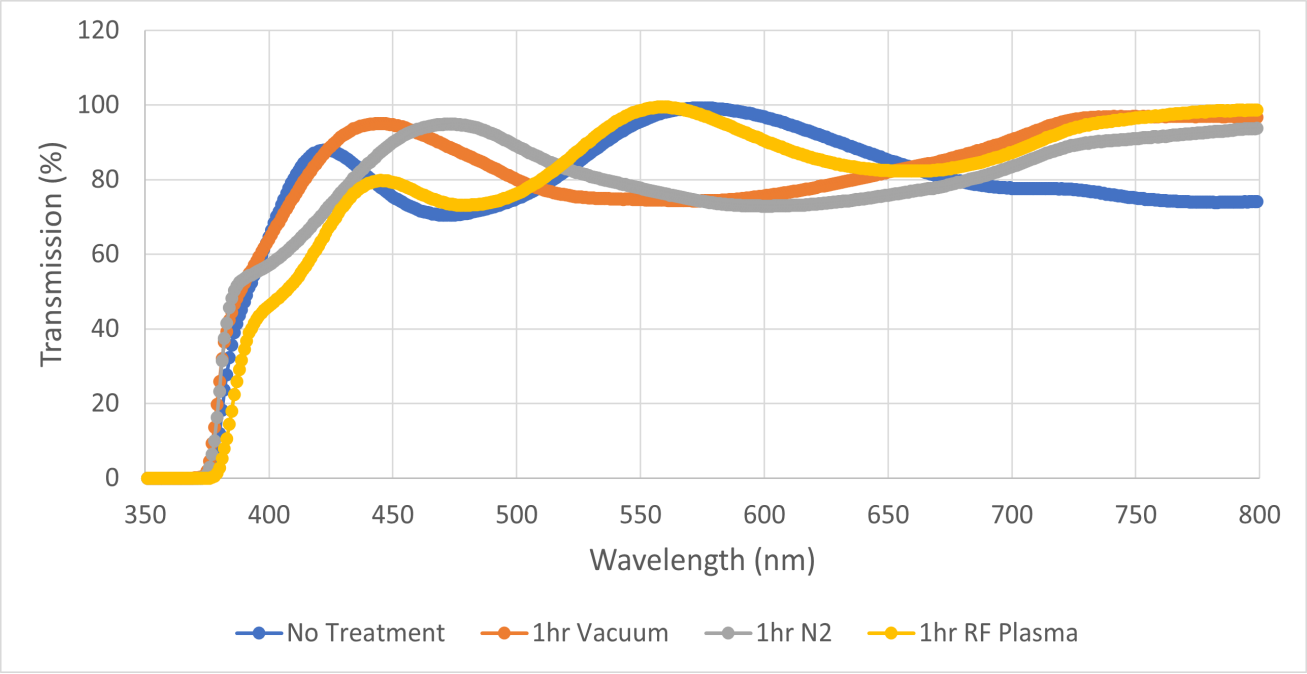

Figure 6.24: Transmission spectrum of different treatments with no Al

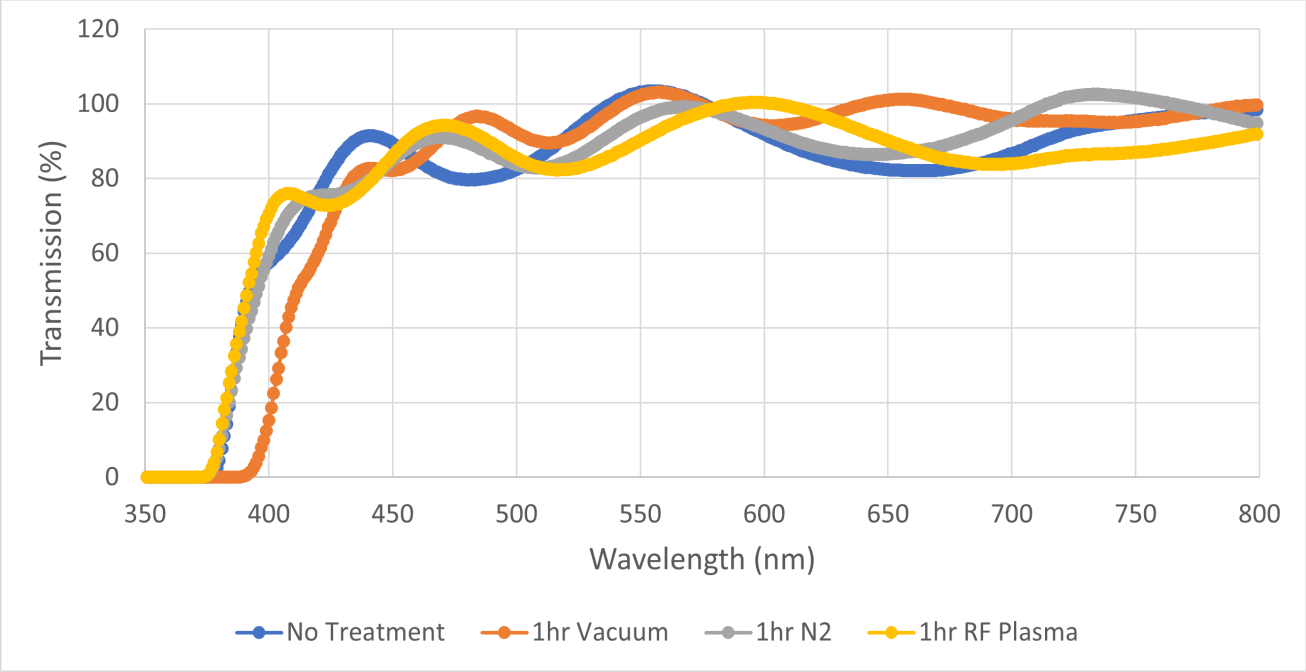

Figure 6.25: Transmission spectrum of different treatments with 0.5% AlCl

Table 6.2: Average percent transmission of different aluminum sources and concentrations after various treatments between 380 and 750 nm

Al Source	No treatment	1hr Vacuum Anneal	1hr N_2 Anneal	1hr RF Plasma
No Al	85.43%	79.44%	79.00%	79.06%
0.5% AlCl	84.79%	85.06%	85.53%	83.45%

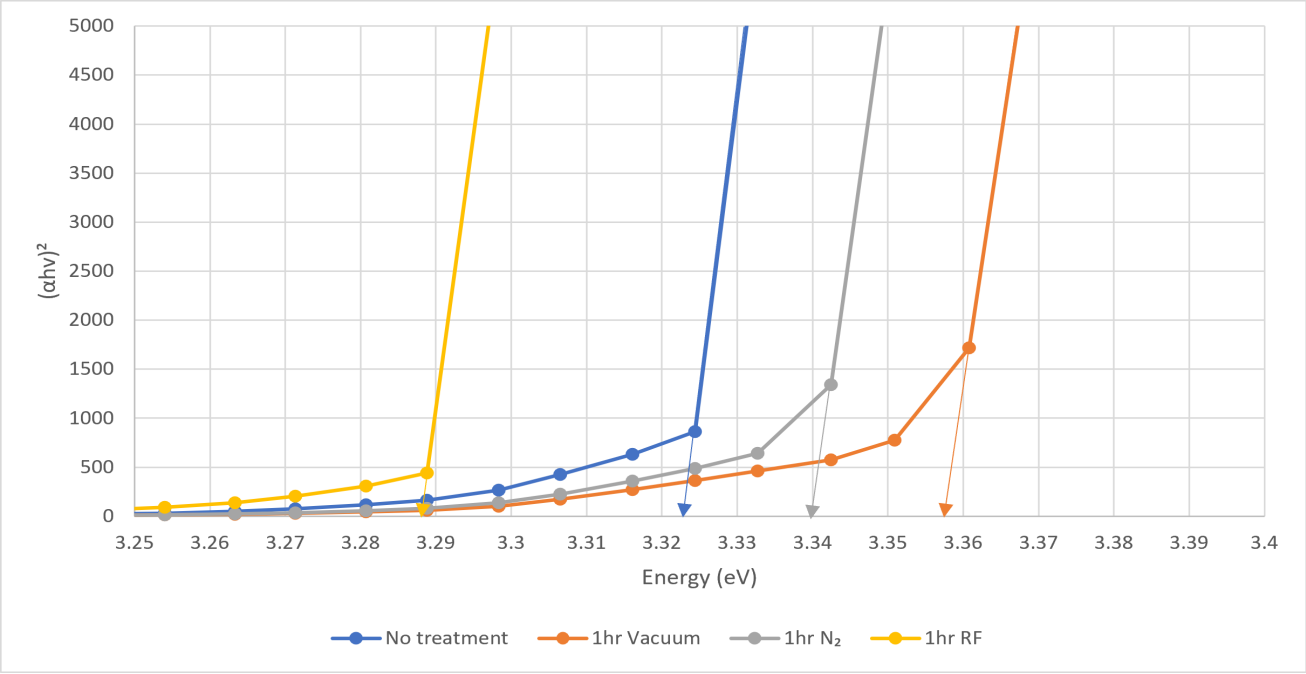

Figure 6.26: Tauc plot of different treatments done with no Al doping with arrows indicating band gap

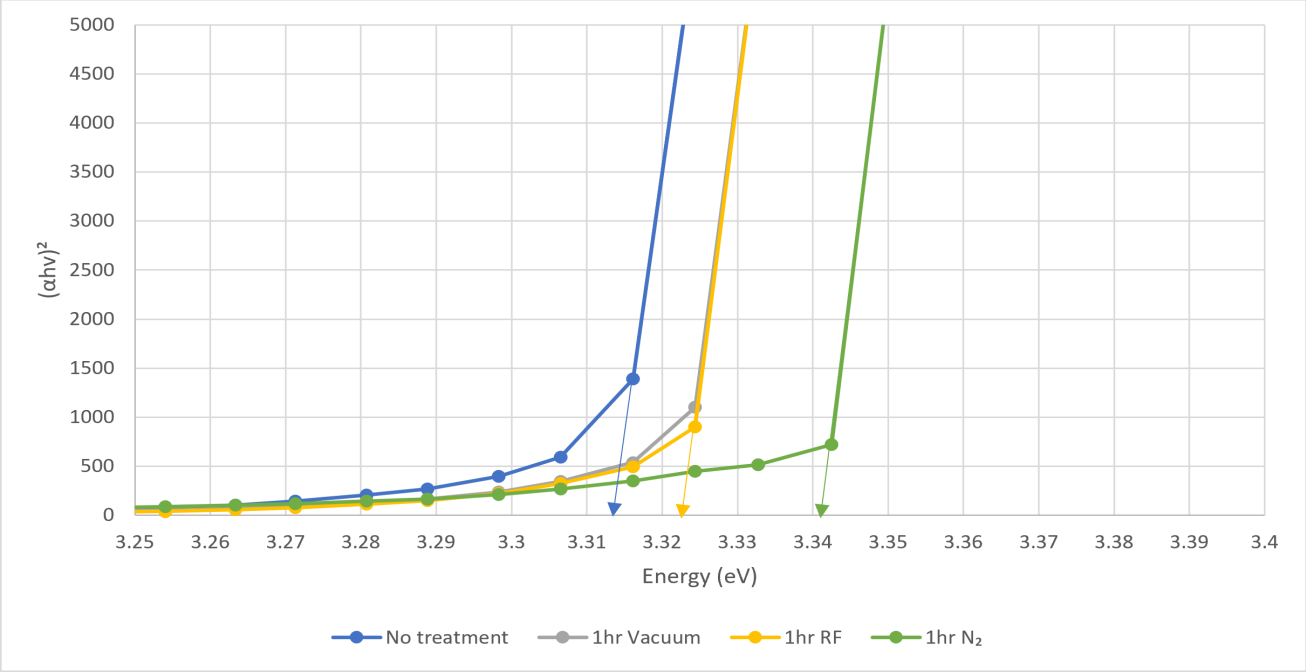

Figure 6.27: Tauc plot of different treatments done with 0.5% AlCl doping with arrows indicating band gap

Electrical Analysis

The hall data for the doped and undoped ZnO samples after the various treatments are tabulated in Table 6.4 and Table 6.3 respectively. For the undoped ZnO, the sample treated in N_2 has the lowest sheet resistance. All treatments show a increase in sheet density by one order of magnitude compared to the untreated sample. The N_2 treated sample has the highest mobility and is the reason for the lowest sheet resistance of all the undoped samples. In regards to the AlCl doped samples, the untreated sample shows both a order of magnitude increase in mobility and sheet density. After treatment, the sheet density was further increased by an order of magnitude to 10^{14}. The carrier mobility was highest for the sample annealed in N_2 resulting in the lowest sheet resistance of the samples treated.

Table 6.3: Hall effect data for no aluminum doping

	No Treatment	Vacuum Anneal	N_2 Anneal	RF Plasma Anneal
Sheet Resistance, R_s ($\Omega/\square$)	386000	42300	30783.33	142950
Sheet Density, n_s (cm^{-1})	3.20 x10^{12}	4.24 x10^{13}	2.93 x10^{13}	1.17 x10^{13}
Carrier Mobility, μ_m ($cm^2V^{-1}s^{-1}$)	5.05	3.48	6.91	3.74

Table 6.4: Hall effect data for 0.5% AlCl doping

	No Treatment	Vacuum Anneal	N_2 Anneal	RF Plasma Anneal
Sheet Resistance, R_s ($\Omega/\square$)	4828.33	367	225.67	526.17
Sheet Density, n_s (cm^{-1})	7.05 x10^{13}	7.69 x10^{14}	9.81 x10^{14}	7.95 x10^{14}
Carrier Mobility, μ_m ($cm^2V^{-1}s^{-1}$)	18.35	22.1	28.21	14.93

Figure of Merit

The FoM of the undoped and 0.5% AlCl doped films obtained after experiment 3 were calculated using the equations discussed in 2.5. They are tabulated below. A larger number indicates better performance as a TCO. As can be seen from the tables below, the 0.5% AlCl doped films after N_2 annealing have the highest FoM of all the samples prepared.

Table 6.5: Haacke FoM, Eq.(2.7)

	No Treatment	Vacuum Anneal	N_2 Anneal	RF Plasma Anneal
No Al	5.36 x10^{-7}	2.37 x10^{-6}	3.08 x10^{-6}	6.67 x10^{-7}
0.5% AlCl	3.98 x10^{-5}	5.40 x10^{-4}	9.28 x10^{-4}	3.11 x10^{-4}

Table 6.6: Jain-Kulshreshtha FoM, Eq.(2.8)

	No Treatment	Vacuum Anneal	N_2 Anneal	RF Plasma Anneal
No Al	1.65 x10^{-5}	1.03 x10^{-4}	1.38 x10^{-4}	2.98 x10^{-5}
0.5% AlCl	1.26 x10^{-3}	1.68 x10^{-2}	2.84 x10^{-2}	1.05 x10^{-2}

Table 6.7: Gruner-Coleman FoM, Eq.(2.9)

	No Treatment	Vacuum Anneal	N_2 Anneal	RF Plasma Anneal
No Al	5.96 x10^{-3}	3.65 x10^{-2}	4.90 x10^{-2}	1.06 x10^{-2}
0.5% AlCl	4.54 x10^{-1}	6.10	10.3	3.78

Chapter 7

Conclusions

A systematic approach was taken to determine the optimal parameters to obtain sol-gel derived thin films with a high FoM for TCO applications. Extensive literature review was conducted in order to understand the chemistry behind sol-gel synthesized thin films. This included understanding the role of solvent, precursor and stabilizer in the reactions leading to a stable sol solution and the effect each has on the final thin film properties. Literature review on the types and concentrations of solvent, precursor and stabilizer was done to determine which types and concentrations would lead to thin films of favorable properties for TCO applications. In addition, literature review of post deposition processing was done to determine their effect on the final thin film properties and which parameters would yield favorable results. Due to the novelty of the solvent used in this work, experiments were first required to find an optimal withdrawal speed of the glass substrates from the sol in order to yield smooth, dense thin films of high crystallinity with preferential c-axis orientation, exhibiting high transparency in the visible range. Next, experiments on numerous aluminum sources and concentrations were conducting in order to substitute Zn atoms with Al to increase n-type carriers while not resulting in phase separation and still producing a smooth, dense thin films of high crystallinity with preferential c-axis orientation, exhibiting high transparency in the visible range. Lastly, a series of additional treatments were conducting on the aluminum doped films to improve the electrical conductivity of the synthesized thin films. In the end, it was found that using n-butanol as a solvent is an excellent alternative to the commonly used 2-methoxyethanol. Using zinc acetate di-hydrate as the zinc precursor at a concentration of 0.75M, monoethanolamine as the stabilizer at a concentration of [MEA]/[Zn] = 1

yielded a stable, reproducible sol. Based on extensive literature review on the effects of preheating and sintering temperatures and durations on the final film properties, it was determined that a preheating temperature of 200^{o}C for 10 minutes and a final sintering temperature of 500^{o}C for one hour would be optimal for ensuring highly preferential c-axis oriented crystalline thin films and supported by results in this work.

Deposition of the sol at various withdrawal speeds revealed an optimal withdrawal speed of 2.5 cm/min resulting in a smooth, dense thin film of high crystallinity with preferential c-axis orientation, exhibiting high transparency in the visible range. From all the aluminum sources tested, AlCl at an atomic percentage of 0.5% was the best at maintaining a high degree of cystallinity without resulting in phase separation or other ZnO crystal orientations arising. Further treatment by annealing the AlCl doped ZnO thin films in a N_2 environment yielded a a smooth, dense thin film of high crystallinity with preferential c-axis orientation, exhibiting high transparency in the visible range with a high FoM for TCO applications. The highest FoM obtained in this work, after additional treatment in N_2 using 0.5% AlCl and deposited at 2.5 cm/min is compared to the FoM from other work focused on obtaining highly transparent and conductive sol-gel derived ZnO:Al films.

Table 7.1: FoM Compare

Work	Haacke FoM	Jain-Kulshreshtha FoM	Gruner-Coleman FoM
This Thesis	9.28 x10^{-4}	2.84 x10^{-2}	10.3
Salam et al. [117]	1.52 x10^{-4}	4.74 x10^{-3}	1.72
Nateq and Ceccato [120]	1.72 x10^{-4}	7.70 x10^{-3}	2.75
Zhao et al. [135]	7.58 x10^{-4}	2.06 x10^{-2}	7.58

Chapter 8

Additional Contributions

In addition to the work presented in this thesis. A paper titled 'Structure of Bandgap Determination on InN Grown bu RP-MOCVD' by Nagorski et al is in the process of being published. As well as a poster presentation titled 'Experimental Study of Lithium Metal in Nitrogen Environment' at the Canadian Semiconductor Science and Technology Conference (CSSTC) held in 2019 at the University of Saskatoon, Canada.

Bibliography

[1] Y. He, X. Wang, Y. Gao, Y. Hou, and Q. Wan, "Oxide-based thin film transistors for flexible electronics," *Journal of Semiconductors*, vol. 39, p. 011005, Jan. 2018.

[2] Ü. Özgür, Y. I. Alivov, C. Liu, A. Teke, M. A. Reshchikov, S. Doğan, V. Avrutin, S.-J. Cho, and H. Morkoç, "A comprehensive review of ZnO materials and devices," *Journal of Applied Physics*, vol. 98, p. 041301, Aug. 2005.

[3] A. Varanytsia, L. Weng, T. Lin, J. Yang, and L. Chien, "High-Performance and Low-Cost Aluminum Zinc Oxide and Gallium Zinc Oxide Electrodes for Liquid Crystal Displays," *Journal of Display Technology*, vol. 12, pp. 1033–1039, Oct. 2016.

[4] E. Fortunato, A. Gonçalves, A. Pimentel, P. Barquinha, G. Gonçalves, L. Pereira, I. Ferreira, and R. Martins, "Zinc oxide, a multifunctional material: From material to device applications," *Applied Physics A*, vol. 96, pp. 197–205, July 2009.

[5] D. S. Ginley and J. D. Perkins, "Transparent Conductors," in *Handbook of Transparent Conductors* (D. S. Ginley, ed.), pp. 1–25, Boston, MA: Springer US, 2011.

[6] "Photovoltaic (PV) Market Size, Share, Growth and Forecasts, 2019-2026." https://www.alliedmarketresearch.com/photovoltaic-market.

[7] T. Minami, "Transparent conducting oxide semiconductors for transparent electrodes," *Semiconductor Science and Technology*, vol. 20, pp. S35–S44, Apr. 2005.

[8] R. E. Hummel, *Electronic Properties of Materials*. New York: Springer-Verlag, fourth ed., 2011.

[9] H. Hosono and K. Ueda, "Transparent Conductive Oxides," in *Springer Handbook of Electronic and Photonic Materials* (S. Kasap and P. Capper, eds.), Springer Handbooks, pp. 1–1, Cham: Springer International Publishing, 2017.

[10] R. G. Gordon, "Criteria for Choosing Transparent Conductors," *MRS Bulletin*, vol. 25, pp. 52–57, Aug. 2000.

[11] G. Haacke, "New figure of merit for transparent conductors," *Journal of Applied Physics*, vol. 47, pp. 4086–4089, Sept. 1976.

[12] V. K. Jain and A. P. Kulshreshtha, "Indium-Tin-Oxide transparent conducting coatings on silicon solar cells and their "figure of merit"," *Solar Energy Materials*, vol. 4, pp. 151–158, Jan. 1981.

[13] L. Hu, D. S. Hecht, and G. Grüner, "Percolation in Transparent and Conducting Carbon Nanotube Networks," *Nano Letters*, vol. 4, pp. 2513–2517, Dec. 2004.

[14] S. De and J. N. Coleman, "Are There Fundamental Limitations on the Sheet Resistance and Transmittance of Thin Graphene Films?," *ACS Nano*, vol. 4, pp. 2713–2720, May 2010.

[15] S. B. Sepulveda-Mora and S. G. Cloutier, "Figures of Merit for High-Performance Transparent Electrodes Using Dip-Coated Silver Nanowire Networks," *Journal of Nanomaterials*, vol. 2012, p. e286104, Sept. 2012.

[16] K. Ellmer, "Transparent Conductive Zinc Oxide and Its Derivatives," in *Handbook of Transparent Conductors* (D. S. Ginley, ed.), pp. 193–263, Boston, MA: Springer US, 2011.

[17] J. Zemann, "Crystal structures, 2nd edition. Vol. 1 by R. W. G. Wyckoff," *Acta Crystallographica*, vol. 18, no. 1, pp. 139–139, 1965.

[18] C. Klingshirn, "Review Article: ZnO: From basics towards applications," *physica status solidi (b)*, vol. 244, no. 9, pp. 3019–3019, 2007.

[19] "Zinc Oxide: Fundamentals, Materials and Device Technology — Wiley." https://www.wiley.com/en-ca/Zinc+Oxide%3A+Fundamentals%2C+Materials+and+Device+Technolog
p-9783527408139.

[20] Bor75, "English: Hexagonal lattice cell. View from the front," 22 January 2013, 17:23:23.

[21] "Wurtzite_polyhedra.png (1417×1417)." https://upload.wikimedia.org/wikipedia/commons/8/8e/Wurtzi

[22] R. Kumar, O. Al-Dossary, G. Kumar, and A. Umar, "Zinc Oxide Nanostructures for NO2 Gas–Sensor Applications: A Review," *Nano-Micro Letters*, vol. 7, pp. 97–120, Apr. 2015.

[23] A. N. Mariano and R. E. Hanneman, "Crystallographic Polarity of ZnO Crystals," *Journal of Applied Physics*, vol. 34, pp. 384–388, Feb. 1963.

[24] Z. L. Wang, "Zinc oxide nanostructures: Growth, properties and applications," *Journal of Physics: Condensed Matter*, vol. 16, pp. R829–R858, June 2004.

[25] S. G. Leonardi, "Two-Dimensional Zinc Oxide Nanostructures for Gas Sensor Applications," *Chemosensors*, vol. 5, p. 17, June 2017.

[26] D. Vogel, P. Krüger, and J. Pollmann, "Self-interaction and relaxation-corrected pseudopotentials for II-VI semiconductors," *Physical Review B*, vol. 54, pp. 5495–5511, Aug. 1996.

[27] P. Schröer, P. Krüger, and J. Pollmann, "First-principles calculation of the electronic structure of the wurtzite semiconductors ZnO and ZnS," *Physical Review B*, vol. 47, pp. 6971–6980, Mar. 1993.

[28] M. Usuda, N. Hamada, T. Kotani, and M. van Schilfgaarde, "All-electron GW calculation based on the LAPW method: Application to wurtzite ZnO," *Physical Review B*, vol. 66, p. 125101, Sept. 2002.

[29] P. Erhart, K. Albe, and A. Klein, "First-principles study of intrinsic point defects in ZnO: Role of band structure, volume relaxation, and finite-size effects," *Physical Review B*, vol. 73, p. 205203, May 2006.

[30] W. Setyawan and S. Curtarolo, "High-throughput electronic band structure calculations: Challenges and tools," *Computational Materials Science*, vol. 49, pp. 299–312, Aug. 2010.

[31] O. Fritsch, "Elektrisches und optisches Verhalten von Halbleitern. X Elektrische Messungen an Zinkoxyd," *Annalen der Physik*, vol. 414, no. 4, pp. 375–401, 1935.

[32] I. Gur, N. A. Fromer, M. L. Geier, and A. P. Alivisatos, "Air-stable all-inorganic nanocrystal solar cells processed from solution," *Science (New York, N.Y.)*, vol. 310, pp. 462–465, Oct. 2005.

[33] A. F. Kohan, G. Ceder, D. Morgan, and C. G. Van de Walle, "First-principles study of native point defects in ZnO," *Physical Review B*, vol. 61, pp. 15019–15027, June 2000.

[34] S. B. Zhang, S.-H. Wei, and A. Zunger, "Intrinsic n-type versus p-type doping asymmetry and the defect physics of ZnO," *Physical Review B*, vol. 63, p. 075205, Jan. 2001.

[35] F. Oba, S. R. Nishitani, S. Isotani, H. Adachi, and I. Tanaka, "Energetics of native defects in ZnO," *Journal of Applied Physics*, vol. 90, pp. 824–828, June 2001.

[36] H. Overhof and J.-M. Spaeth, "Defect identification in the ${\mathrm{As}}_{\mathrm{Ga}}$ family in GaAs," *Physical Review B*, vol. 72, p. 115205, Sept. 2005.

[37] S. B. Zhang and J. E. Northrup, "Chemical potential dependence of defect formation energies in GaAs: Application to Ga self-diffusion," *Physical Review Letters*, vol. 67, pp. 2339–2342, Oct. 1991.

[38] W. Walukiewicz, "Intrinsic limitations to the doping of wide-gap semiconductors," *Physica B: Condensed Matter*, vol. 302-303, pp. 123–134, Jan. 2001.

[39] K. Ellmer, A. Klein, and B. Rech, eds., *Transparent Conductive Zinc Oxide: Basics and Applications in Thin Film Solar Cells*. Springer Series in Materials Science, Berlin Heidelberg: Springer-Verlag, 2008.

[40] D. C. Look, J. W. Hemsky, and J. R. Sizelove, "Residual Native Shallow Donor in ZnO," *Physical Review Letters*, vol. 82, pp. 2552–2555, Mar. 1999.

[41] P. Erhart and K. Albe, "First-principles study of migration mechanisms and diffusion of oxygen in zinc oxide," *Physical Review B*, vol. 73, p. 115207, Mar. 2006.

[42] P. Erhart and K. Albe, "Diffusion of zinc vacancies and interstitials in zinc oxide," *Applied Physics Letters*, vol. 88, p. 201918, May 2006.

[43] U. Ozgur, D. Hofstetter, and H. Morkoc, "ZnO Devices and Applications: A Review of Current Status and Future Prospects," *Proceedings of the IEEE*, vol. 98, pp. 1255–1268, July 2010.

[44] G. Heiland, E. Mollwo, and F. Stöckmann, "Electronic Processes in Zinc Oxide," in *Solid State Physics* (F. Seitz and D. Turnbull, eds.), vol. 8, pp. 191–323, Academic Press, Jan. 1959.

[45] A. R. Hutson, "Hall Effect Studies of Doped Zinc Oxide Single Crystals," *Physical Review*, vol. 108, pp. 222–230, Oct. 1957.

[46] C. G. Van de Walle, "Hydrogen as a Cause of Doping in Zinc Oxide," *Physical Review Letters*, vol. 85, pp. 1012–1015, July 2000.

[47] N. H. Nickel and E. Terukov, eds., *Zinc Oxide - A Material for Micro- and Optoelectronic Applications: Proceedings of the NATO Advanced Research Workshop on Zinc Oxide as a Material for Micro- and Optoelectronic Applications, Held in St. Petersburg, Russia, from 23 to 25 June 2004.* NATO Science Series II: Mathematics, Physics and Chemistry, Springer Netherlands, 2005.

[48] T. Minami, H. Sato, H. Nanto, and S. Takata, "Group III Impurity Doped Zinc Oxide Thin Films Prepared by RF Magnetron Sputtering," *Japanese Journal of Applied Physics*, vol. 24, p. L781, Oct. 1985.

[49] J. Y. W. Seto, "The electrical properties of polycrystalline silicon films," *Journal of Applied Physics*, vol. 46, pp. 5247–5254, Dec. 1975.

[50] H. Hosono, D. C. Paine, and D. Ginley, eds., *Handbook of Transparent Conductors.* Springer US, 2011.

[51] J. Mistrik, S. Kasap, H. E. Ruda, C. Koughia, and J. Singh, "Optical Properties of Electronic Materials: Fundamentals and Characterization," in *Springer Handbook of Electronic and Photonic Materials* (S. Kasap and P. Capper, eds.), Springer Handbooks, pp. 1–1, Cham: Springer International Publishing, 2017.

[52] S. O. Kasap, *Principles of Electronic Materials and Devices.* McGraw-Hill, 2006.

[53] A. Mang, K. Reimann, and S. Rübenacke, "Band gaps, crystal-field splitting, spin-orbit coupling, and exciton binding energies in ZnO under hydrostatic pressure," *Solid State Communications*, vol. 94, pp. 251–254, Apr. 1995.

[54] D. C. Reynolds, D. C. Look, B. Jogai, C. W. Litton, G. Cantwell, and W. C. Harsch, "Valence-band ordering in ZnO," *Physical Review B*, vol. 60, pp. 2340–2344, July 1999.

[55] D. Look, "Recent Advances in ZnO Materials and Devices," *Materials Science and Engineering B-Solid State Materials for Advanced Technology*, vol. 80, pp. 383–387, Jan. 2001.

[56] D. M. Bagnall, Y. F. Chen, Z. Zhu, T. Yao, S. Koyama, M. Y. Shen, and T. Goto, "Optically pumped lasing of ZnO at room temperature," *Applied Physics Letters*, vol. 70, pp. 2230–2232, Apr. 1997.

[57] D. C. Reynolds, D. C. Look, and B. Jogai, "Optically pumped ultraviolet lasing from ZnO," *Solid State Communications*, vol. 99, pp. 873–875, Sept. 1996.

[58] Y. Segawa, A. Ohtomo, M. Kawasaki, H. Koinuma, Z. K. Tang, P. Yu, and G. K. L. Wong, "Growth of ZnO Thin Film by Laser MBE: Lasing of Exciton at Room Temperature," *physica status solidi (b)*, vol. 202, no. 2, pp. 669–672, 1997.

[59] P. Zu, Z. K. Tang, G. K. L. Wong, M. Kawasaki, A. Ohtomo, H. Koinuma, and Y. Segawa, "Ultraviolet spontaneous and stimulated emissions from ZnO microcrystallite thin films at room temperature," *Solid State Communications*, vol. 103, pp. 459–463, Aug. 1997.

[60] Z. K. Tang, G. K. L. Wong, P. Yu, M. Kawasaki, A. Ohtomo, H. Koinuma, and Y. Segawa, "Room-temperature ultraviolet laser emission from self-assembled ZnO microcrystallite thin films," *Applied Physics Letters*, vol. 72, pp. 3270–3272, June 1998.

[61] "Zinc Oxide: Fundamentals, Materials and Device Technology — Wiley." https://www.wiley.com/en-us/Zinc+Oxide%3A+Fundamentals%2C+Materials+and+Device+Technolog
p-9783527408139.

[62] R. Dingle, "Luminescent Transitions Associated With Divalent Copper Impurities and the Green Emission from Semiconducting Zinc Oxide," *Physical Review Letters*, vol. 23, pp. 579–581, Sept. 1969.

[63] Y. I. Alivov, M. V. Chukichev, and V. A. Nikitenko, "Green luminescence band of zinc oxide films copper-doped by thermal diffusion," *Semiconductors*, vol. 38, pp. 31–35, Jan. 2004.

[64] B. Guo, Z. R. Qiu, and K. S. Wong, "Intensity dependence and transient dynamics of donor–acceptor pair recombination in ZnO thin films grown on (001) silicon," *Applied Physics Letters*, vol. 82, pp. 2290–2292, Apr. 2003.

[65] F. H. Leiter, H. R. Alves, A. Hofstaetter, D. M. Hofmann, and B. K. Meyer, "The Oxygen Vacancy as the Origin of a Green Emission in Undoped ZnO," *physica status solidi (b)*, vol. 226, no. 1, pp. R4–R5, 2001.

[66] M. Liu, A. H. Kitai, and P. Mascher, "Point defects and luminescence centres in zinc oxide and zinc oxide doped with manganese," *Journal of Luminescence*, vol. 54, pp. 35–42, Aug. 1992.

[67] W. Shan, W. Walukiewicz, J. W. Ager, K. M. Yu, H. B. Yuan, H. P. Xin, G. Cantwell, and J. J. Song, "Nature of room-temperature photoluminescence in ZnO," *Applied Physics Letters*, vol. 86, p. 191911, May 2005.

[68] P. A. Rodnyi and I. V. Khodyuk, "Optical and luminescence properties of zinc oxide (Review)," *Optics and Spectroscopy*, vol. 111, pp. 776–785, Nov. 2011.

[69] D. C. Reynolds, D. C. Look, and B. Jogai, "Fine structure on the green band in ZnO," *Journal of Applied Physics*, vol. 89, pp. 6189–6191, June 2001.

[70] A. Kołodziejczak-Radzimska and T. Jesionowski, "Zinc Oxide—From Synthesis to Application: A Review," *Materials*, vol. 7, pp. 2833–2881, Apr. 2014.

[71] H.-L. Liu, H.-L. Yang, B.-C. Lin, W. Zhang, L. Tian, H.-S. Zhang, and Z.-G. Xi, "Toxic effect comparison of three typical sterilization nanoparticles on oxidative stress and immune inflammation response in rats," *Toxicology Research*, vol. 4, pp. 486–493, Feb. 2015.

[72] A. Sirelkhatim, S. Mahmud, A. Seeni, N. H. M. Kaus, L. C. Ann, S. K. M. Bakhori, H. Hasan, and D. Mohamad, "Review on Zinc Oxide Nanoparticles: Antibacterial Activity and Toxicity Mechanism," *Nano-Micro Letters*, vol. 7, no. 3, pp. 219–242, 2015.

[73] A. H. Kitai, "Oxide phosphor and dielectric thin films for electroluminescent devices," *Thin Solid Films*, vol. 445, pp. 367–376, Dec. 2003.

[74] F. Rahman, "Zinc oxide light-emitting diodes: A review," *Optical Engineering*, vol. 58, p. 010901, Jan. 2019.

[75] B. D. Boruah, "Zinc oxide ultraviolet photodetectors: Rapid progress from conventional to self-powered photodetectors," *Nanoscale Advances*, vol. 1, no. 6, pp. 2059–2085, 2019.

[76] M. Willander, O. Nur, Q. X. Zhao, L. L. Yang, M. Lorenz, B. Q. Cao, J. Z. Pérez, C. Czekalla, G. Zimmermann, M. Grundmann, A. Bakin, A. Behrends, M. Al-Suleiman, A. El-Shaer, A. C. Mofor, B. Postels, A. Waag, N. Boukos, A. Travlos, H. S. Kwack, J. Guinard, and D. L. S. Dang, "Zinc oxide nanorod based photonic devices: Recent progress in growth, light emitting diodes and lasers," *Nanotechnology*, vol. 20, p. 332001, July 2009.

[77] L. M. Dorozhkin and I. A. Rozanov, "Acoustic Wave Chemical Sensors for Gases," *Journal of Analytical Chemistry*, vol. 56, pp. 399–416, May 2001.

[78] A. Mahmood and A. Naeem, "Sol-Gel-Derived Doped ZnO Thin Films: Processing, Properties, and Applications," *Recent Applications in Sol-Gel Synthesis*, July 2017.

[79] T. Senthil and S. Anandhan, "Structure–property relationship of sol–gel electrospun ZnO nanofibers developed for ammonia gas sensing," *Journal of Colloid and Interface Science*, vol. 432, pp. 285–296, Oct. 2014.

[80] M. Hjiri, L. El Mir, S. G. Leonardi, N. Donato, and G. Neri, "CO and NO2 Selective Monitoring by ZnO-Based Sensors," *Nanomaterials*, vol. 3, pp. 357–369, July 2013.

[81] "Highly Sensitive and Selective Ethanol Sensor Fabricated with In-Doped 3DOM ZnO — ACS Applied Materials & Interfaces." https://pubs.acs.org/doi/abs/10.1021/acsami.6b00339.

[82] A. P. Rambu, N. Iftimie, V. Nica, M. Dobromir, and S. Tascu, "Efficient methane detection by Co doping of ZnO thin films," *Superlattices and Microstructures*, vol. Complete, no. 78, pp. 61–70, 2015.

[83] Q. Ren, Y.-Q. Cao, D. Arulraj, C. Liu, D. Wu, W.-M. Li, and A.-D. Li, "Review—Resistive-Type Hydrogen Sensors Based on Zinc Oxide Nanostructures," *Journal of The Electrochemical Society*, vol. 167, p. 067528, Apr. 2020.

[84] R. Dhahri, M. Hjiri, L. El Mir, H. Alamri, A. Bonavita, D. Iannazzo, S. G. Leonardi, and G. Neri, "CO sensing characteristics of In-doped ZnO semiconductor nanoparticles," *Journal of Science: Advanced Materials and Devices*, vol. 2, pp. 34–40, Mar. 2017.

[85] A. Janotti and C. G. V. de Walle, "Fundamentals of zinc oxide as a semiconductor," *Reports on Progress in Physics*, vol. 72, p. 126501, Oct. 2009.

[86] D. M. Mattox, "Chapter 1 - Introduction," in *Handbook of Physical Vapor Deposition (PVD) Processing (Second Edition)* (D. M. Mattox, ed.), pp. 1–24, Boston: William Andrew Publishing, Jan. 2010.

[87] R. M. Pasquarelli, D. S. Ginley, and R. O'Hayre, "Solution processing of transparent conductors: From flask to film," *Chemical Society Reviews*, vol. 40, pp. 5406–5441, Oct. 2011.

[88] "Sol-Gel Science - 1st Edition." https://www.elsevier.com/books/sol-gel-science/brinker/978-0-08-057103-4.

[89] A. E. Danks, S. R. Hall, and Z. Schnepp, "The evolution of 'sol–gel' chemistry as a technique for materials synthesis," *Materials Horizons*, vol. 3, pp. 91–112, Feb. 2016.

[90] J. Livage, "Sol-gel processes," *Current Opinion in Solid State and Materials Science*, vol. 2, pp. 132–138, Apr. 1997.

[91] L. Spanhel and M. A. Anderson, "Semiconductor clusters in the sol-gel process: Quantized aggregation, gelation, and crystal growth in concentrated zinc oxide colloids," *Journal of the American Chemical Society*, vol. 113, pp. 2826–2833, Apr. 1991.

[92] L. Spanhel, "Colloidal ZnO nanostructures and functional coatings: A survey," *Journal of Sol-Gel Science and Technology*, vol. 39, pp. 7–24, July 2006.

[93] L. Znaidi, G. J. A. A. Soler Illia, S. Benyahia, C. Sanchez, and A. V. Kanaev, "Oriented ZnO thin films synthesis by sol–gel process for laser application," *Thin Solid Films*, vol. 428, pp. 257–262, Mar. 2003.

[94] V. Briois, C. Giorgetti, F. Baudelet, S. Blanchandin, M. S. Tokumoto, S. H. Pulcinelli, and C. V. Santilli, "Dynamical Study of ZnO Nanocrystal and Zn-HDS Layered Basic Zinc Acetate Formation from Sol-Gel Route," *The Journal of Physical Chemistry C*, vol. 111, pp. 3253–3258, Mar. 2007.

[95] P. Hosseini Vajargah, H. Abdizadeh, R. Ebrahimifard, and M. R. Golobostanfard, "Sol–gel derived ZnO thin films: Effect of amino-additives," *Applied Surface Science*, vol. 285, pp. 732–743, Nov. 2013.

[96] M. Guglielmi and G. Carturan, "Precursors for sol-gel preparations," *Journal of Non-Crystalline Solids*, vol. 100, pp. 16–30, Mar. 1988.

[97] L. Armelao, M. Fabrizio, S. Gialanella, and F. Zordan, "Sol–gel synthesis and characterisation of ZnO-based nanosystems," *Thin Solid Films*, vol. 394, pp. 89–95, Aug. 2001.

[98] D. W. Bahnemann, C. Kormann, and M. R. Hoffmann, "Preparation and characterization of quantum size zinc oxide: A detailed spectroscopic study," *The Journal of Physical Chemistry*, vol. 91, pp. 3789–3798, July 1987.

[99] L. Znaidi, G. S. Illia, R. L. Guennic, C. Sanchez, and A. Kanaev, "Elaboration of ZnO Thin Films with Preferential Orientation by a Soft Chemistry Route," *Journal of Sol-Gel Science and Technology*, vol. 26, pp. 817–821, Jan. 2003.

[100] I. Kim, Y. Kim, G. Nam, D. Kim, M. Park, H. Kim, W. Lee, J.-Y. Leem, J. S. Kim, and J. S. Kim, "Effect of different sol concentrations on the properties of nanocrystalline ZnO thin films grown on FTO substrates by sol-gel spin-coating," *Journal of the Korean Physical Society*, vol. 65, pp. 480–486, Aug. 2014.

[101] F. C. M. van de Pol, F. R. Blom, and T. J. A. Popma, "R.F. planar magnetron sputtered ZnO films I: Structural properties," *Thin solid films*, vol. 204, no. 2, pp. 349–364, 1991.

[102] I. Petrov, V. Orlinov, and A. Misiuk, "Highly oriented ZnO films obtained by d.c. reactive sputtering of a zinc target," *Thin Solid Films*, vol. 120, pp. 55–67, Oct. 1984.

[103] Z. Hu, G. Oskam, and P. C. Searson, "Influence of solvent on the growth of ZnO nanoparticles," *Journal of Colloid and Interface Science*, vol. 263, pp. 454–460, July 2003.

[104] E. Hosono, S. Fujihara, T. Kimura, and H. Imai, "Growth of layered basic zinc acetate in methanolic solutions and its pyrolytic transformation into porous zinc oxide films," *Journal of Colloid and Interface Science*, vol. 272, pp. 391–398, Apr. 2004.

[105] Z. Hu, J. F. Herrera Santos, G. Oskam, and P. C. Searson, "Influence of the reactant concentrations on the synthesis of ZnO nanoparticles," *Journal of Colloid and Interface Science*, vol. 288, pp. 313–316, Aug. 2005.

[106] n. Hu, n. Payzant, and n. Byers, "Sol-Gel and Ultrafine Particle Formation via Dielectric Tuning of Inorganic Salt-Alcohol-Water Solutions," *Journal of Colloid and Interface Science*, vol. 222, pp. 20–36, Feb. 2000.

[107] "Physical Properties of Solvents," p. 1.

[108] Y. Ohya, T. Ogata, T. Ban, and Y. Takahashi, "Microstructure of Sol-Gel ZnO Thin Films Fabricated Using Ethanolamine and Hydroxyketone Modifiers," *Journal of the Ceramic Society of Japan*, vol. 113, no. 1315, pp. 220–225, 2005.

[109] K. Thongsuriwong, P. Amornpitoksuk, and S. Suwanboon, "The effect of aminoalcohols (MEA, DEA and TEA) on morphological control of nanocrystalline ZnO powders and its optical properties," *Journal of Physics and Chemistry of Solids*, vol. 71, pp. 730–734, May 2010.

[110] L. Znaidi, "Sol–gel-deposited ZnO thin films: A review," *Materials Science and Engineering: B*, vol. 174, pp. 18–30, Oct. 2010.

[111] A. P. A. Oliveira, J.-F. Hochepied, F. Grillon, and M.-H. Berger, "Controlled Precipitation of Zinc Oxide Particles at Room Temperature," *Chemistry of Materials*, vol. 15, pp. 3202–3207, Aug. 2003.

[112] R. A. McBride, J. M. Kelly, and D. E. McCormack, "Growth of well-defined ZnO microparticles by hydroxide ion hydrolysis of zinc salts," *Journal of Materials Chemistry*, vol. 13, pp. 1196–1201, Apr. 2003.

[113] M. Treblow, "Organic chemistry (Morrison, Robert T.; Boyd, Robert Neilson)," *Journal of Chemical Education*, vol. 44, p. 182, Mar. 1967.

[114] I. Winer, G. E. Shter, M. Mann-Lahav, and G. S. Grader, "Effect of solvents and stabilizers on sol–gel deposition of Ga-doped zinc oxide TCO films," *Journal of Materials Research*, vol. 26, pp. 1309–1315, May 2011.

[115] K. Yim, H. W. Kim, and C. Lee, "Effects of annealing on structure, resistivity and transmittance of Ga doped ZnO films," *Materials Science and Technology*, vol. 23, pp. 108–112, Jan. 2007.

[116] R. Ebrahimifard, H. Abdizadeh, and M. r Golobostanfard, "Influence of Al nitrate and Al chloride doping sources on structural and optical properties of sol-gel derived Al:ZnO nanoparticles," *Micro Nano Letters*, vol. 7, pp. 572–575, June 2012.

[117] S. Salam, M. Islam, and A. Akram, "Sol–gel synthesis of intrinsic and aluminum-doped zinc oxide thin films as transparent conducting oxides for thin film solar cells," *Thin Solid Films*, vol. 529, pp. 242–247, Feb. 2013.

[118] A. A. Al-Ghamdi, O. A. Al-Hartomy, M. El Okr, A. M. Nawar, S. El-Gazzar, F. El-Tantawy, and F. Yakuphanoglu, "Semiconducting properties of Al doped ZnO thin films," *Spectrochimica Acta Part A: Molecular and Biomolecular Spectroscopy*, vol. 131, pp. 512–517, Oct. 2014.

[119] M. N. H. Mia, U. Habiba, M. F. Pervez, H. Kabir, S. Nur, M. F. Hossen, S. K. Sen, M. K. Hossain, M. A. Iftekhar, and M. M. Rahman, "Investigation of aluminum doping on

structural and optical characteristics of sol–gel assisted spin-coated nano-structured zinc oxide thin films," *Applied Physics A*, vol. 126, p. 162, Feb. 2020.

[120] M. H. Nateq and R. Ceccato, "Enhanced Sol–Gel Route to Obtain a Highly Transparent and Conductive Aluminum-Doped Zinc Oxide Thin Film," *Materials*, vol. 12, p. 1744, Jan. 2019.

[121] J. Zhang and W. Que, "Preparation and characterization of sol–gel Al-doped ZnO thin films and ZnO nanowire arrays grown on Al-doped ZnO seed layer by hydrothermal method," *Solar Energy Materials and Solar Cells*, vol. 94, pp. 2181–2186, Dec. 2010.

[122] Y.-S. Kim, W.-P. Tai, and S.-J. Shu, "Effect of preheating temperature on structural and optical properties of ZnO thin films by sol–gel process," *Thin Solid Films*, vol. 491, pp. 153–160, Nov. 2005.

[123] M. Ohyama, H. Kouzuka, and T. Yoko, "Sol-gel preparation of ZnO films with extremely preferred orientation along (002) plane from zinc acetate solution," *Thin Solid Films*, vol. 306, pp. 78–85, Aug. 1997.

[124] T.-Q. Liu, O. Sakurai, N. Mizutani, and M. Kato, "Preparation of spherical fine ZnO particles by the spray pyrolysis method using ultrasonic atomization techniques," *Journal of Materials Science*, vol. 21, pp. 3698–3702, Oct. 1986.

[125] Y. Ohya, H. Saiki, T. Tanaka, and Y. Takahashi, "Microstructure of TiO2 and ZnO Films Fabricated by the Sol-Gel Method," *Journal of the American Ceramic Society*, vol. 79, no. 4, pp. 825–830, 1996.

[126] J. Chen, D. Chen, and Z. Chen, "Optimization of the process for preparing Al-doped ZnO thin films by sol-gel method," *Science in China Series E: Technological Sciences*, vol. 52, pp. 88–94, Jan. 2009.

[127] D. R. Uhlmann, D. R. Ulrich, and University of Arizona, eds., *Ultrastructure Processing of Advanced Materials*. New York: Wiley, 1992.

[128] "Manual of Mineral Science, 23rd Edition — Wiley." https://www.wiley.com/en-us/Manual+of+Mineral+Science%2C+23rd+Edition-p-9780471721574.

[129] "Schematic-of-scanning-electron-microscope.jpg (444×320)." https://www.nanoscience.com/wp-content/uploads/2018/05/Schematic-of-scanning-electron-microscope.jpg.

[130] Ponor, "English: Teardrop-shaped electron–matter interaction volume and limits to the depths from which each signal type can be emitted or detected.," Aug. 2020.

[131] "Atomic-force-microscope-diagram.png (500×517)." https://www.polymersolutions.com/blog/wp-content/uploads/2014/05/Atomic-force-microscope-diagram.png.

[132] "EEM. Nanotechnology and Nanoelectronics - ppt video online download." https://slideplayer.com/slide/9702681/.

[133] M. G. Mellon, "Analytical experiments in spectrophotometry," *Journal of Chemical Education*, vol. 19, p. 415, Sept. 1942.

[134] erik.secula@nist.gov, "The Hall Effect." https://www.nist.gov/pml/nanoscale-device-characterization-division/popular-links/hall-effect/hall-effect, Apr. 2010.

[135] X. Zhao, H. Shen, C. Zhou, S. Lin, X. Li, X. Zhao, X. Deng, J. Li, and H. Lin, "Preparation of aluminum doped zinc oxide films with low resistivity and outstanding transparency by a sol–gel method for potential applications in perovskite solar cell," *Thin Solid Films*, vol. 605, pp. 208–214, Apr. 2016.

Appendices

Appendix A

Dip Coater Arduino Code

```
#include <TMC2130Stepper.h>
#include <TMC2130Stepper_REGDEFS.h>
#include <TMC2130Stepper_UTILITY.h>

#define EN_PIN                          PB4
#define DIR_PIN                         PB3
#define STEP_PIN                        PB1
#define RELAY_PIN                       PB5
#define CS_PIN                          PB0
#define DIP_PB                          PB10
#define LIM_SW                          PB11
#define SEL_SW                          PB13
#define GREEN_LED                       PB14

//Variables
bool up = 0;
bool down = 1;

int lead_pitch = 8;
int rot_steps = 200;
```

```
int tot_steps;
int dip_count;
int cool_count;

long count;
long req_steps;
long cooldown_steps;
long slowdown_steps;
long step_count;

float home_rate;
float dip_rate;
float pre_dip_rate;
float program_rate;
float run_rate;
float cool_rate;

float home_step_dur;
float pre_dip_step_dur;
float dip_step_dur;
float program_step_dur;
float run_step_dur;
float cool_step_dur;

//User Defined Variables
int micro_steps = 8;
int req_dips = 9;
int heat_time = 15;
int cooldown_time = 2;
int dwell_time = 45;
```

```
float home_travel_rate = (80 / 6);
float pre_dip_travel_rate = (2.5 / 6);
float dip_travel_rate = (2.5 / 6);
float cool_travel_rate = (20 / 6);
float run_travel_rate = (80 / 6);
float program_travel_rate = (30 / 6);
float dip_depth = 50;
float cooldown_distance = 140;



void setup()
{

//defining output pins
pinMode(GREEN_LED, OUTPUT);
pinMode(DIR_PIN, OUTPUT);
pinMode(EN_PIN, OUTPUT);
pinMode(STEP_PIN, OUTPUT);
pinMode(RELAY_PIN, OUTPUT);

//defining input pins
pinMode(DIP_PB, INPUT);
pinMode(LIM_SW, INPUT);
pinMode(SEL_SW, INPUT);

//tmc2130 setup
TMC2130Stepper TMC2130 = TMC2130Stepper(EN_PIN, DIR_PIN, STEP_PIN, CS_PIN);
TMC2130.begin();
TMC2130.microsteps(micro_steps);
TMC2130.SilentStepStick2130(600);
```

```
TMC2130.stealthChop(1);
TMC2130.hold_current(0);

//calculate total steps/rotation
tot_steps = micro_steps * rot_steps;

//rotation rate calculations based on various travel rates
home_rate = home_travel_rate / lead_pitch;
pre_dip_rate = pre_dip_travel_rate / lead_pitch;
dip_rate = dip_travel_rate / lead_pitch;
cool_rate = cool_travel_rate / lead_pitch;
program_rate = program_travel_rate / lead_pitch;
run_rate = run_travel_rate / lead_pitch;

//step duration calculation based on desired microsteps and rotation rates
home_step_dur = (1 / (home_rate * tot_steps)) * 1000000;
pre_dip_step_dur = (1 / (pre_dip_rate * tot_steps)) * 1000000;
dip_step_dur = (1 / (dip_rate * tot_steps)) * 1000000;
cool_step_dur = (1 / (cool_rate * tot_steps)) * 1000000;
program_step_dur = (1/ (program_rate * tot_steps)) * 1000000;
run_step_dur = (1/ (run_rate * tot_steps)) * 1000000;

//step count calculation based on desired distances
cooldown_steps = (cooldown_distance/lead_pitch)*tot_steps;
slowdown_steps = (dip_depth/lead_pitch)*tot_steps;

digitalWrite(GREEN_LED, LOW);
digitalWrite(EN_PIN, LOW);
digitalWrite(DIR_PIN, up);
```

```
while (digitalRead(LIM_SW) == HIGH)
{
digitalWrite(STEP_PIN, HIGH);
delayMicroseconds(home_step_dur/2);
digitalWrite(STEP_PIN, LOW);
delayMicroseconds(home_step_dur/2);
}

}

void loop()
{

////////////PROGRAM MODE//////////////
//if position switch in program mode
if (digitalRead(SEL_SW) == HIGH)
{

//setting dip distance loop
if (digitalRead(DIP_PB) == HIGH)
{
count = 0;
req_steps = 0;
dip_count = 0;
digitalWrite(DIR_PIN, down);

//lower platform while PB is pressed while counting number of steps taken
while (digitalRead(DIP_PB) == HIGH)
{
//lower faster while in heater
```

```
while(count < cooldown_steps)
{
digitalWrite(STEP_PIN, HIGH);
delayMicroseconds(program_step_dur/8);
digitalWrite(STEP_PIN, LOW);
delayMicroseconds(program_step_dur/8);
count++;
}
//slow down once heater cleared
digitalWrite(STEP_PIN, HIGH);
delayMicroseconds(program_step_dur/2);
digitalWrite(STEP_PIN, LOW);
delayMicroseconds(program_step_dur/2);
count++;
}

req_steps = count;
step_count = req_steps;

delay(1000);

//raise platform back to initial position
digitalWrite(DIR_PIN, up);
while (count > 0)
{
digitalWrite(STEP_PIN, HIGH);
delayMicroseconds(program_step_dur/8);
digitalWrite(STEP_PIN, LOW);
delayMicroseconds(program_step_dur/8);
count--;
```

```
}
digitalWrite(GREEN_LED, HIGH);
}
}

////////////RUN MODE////////////
//if position switch in run mode
if (digitalRead(SEL_SW) == LOW)
{
//main dip loop
if (digitalRead(DIP_PB) == HIGH)
{
//while loop for meeting number of required dips
for (dip_count; dip_count < req_dips; dip_count++)
{
if (dip_count == 0)
{
digitalWrite(DIR_PIN, down);

//lower at run travel rate until slowdown distance is reached,
after which it will slowdown to half of dip rate
while (step_count > slowdown_steps)
{
digitalWrite(STEP_PIN, HIGH);
delayMicroseconds(run_step_dur/2);
digitalWrite(STEP_PIN, LOW);
delayMicroseconds(run_step_dur/2);
step_count--;
}
```

```
//slowdown distance reached, travel desired dip distance at half of dip rate
while (step_count  > 0)
{
digitalWrite(STEP_PIN, HIGH);
delayMicroseconds(pre_dip_step_dur/2);
digitalWrite(STEP_PIN, LOW);
delayMicroseconds(pre_dip_step_dur/2);
step_count--;
}

delay(1000 * dwell_time);

digitalWrite(DIR_PIN, up);

//raise for desired dip distance at desired dip rate
while (step_count < slowdown_steps)
{
digitalWrite(STEP_PIN, HIGH);
delayMicroseconds(dip_step_dur/2);
digitalWrite(STEP_PIN, LOW);
delayMicroseconds(dip_step_dur/2);
step_count++;
}

//travelled desired dip distance, now speed up to run travel rate until platform reaches t
while (step_count < req_steps )
{
digitalWrite(STEP_PIN, HIGH);
delayMicroseconds(run_step_dur/2);
digitalWrite(STEP_PIN, LOW);
```

```
delayMicroseconds(run_step_dur/2);
step_count++;
}

digitalWrite(RELAY_PIN, HIGH);

delay(60 * 1000 * heat_time);

digitalWrite(RELAY_PIN, LOW);
}

if (dip_count > 0)
{
digitalWrite(DIR_PIN, down);

//lower at half of run travel rate until cooldown distance is reached,
after which it will wait for desired cooldown period before continuing
while (cool_count < cooldown_steps)
{
digitalWrite(STEP_PIN, HIGH);
delayMicroseconds(cool_step_dur/2);
digitalWrite(STEP_PIN, LOW);
delayMicroseconds(cool_step_dur/2);
step_count--;
cool_count++;
}

delay(60 * 1000 * cooldown_time);
cool_count = 0;
```

```
//lower at run travel rate until slowdown distance is reached,
after which it will slowdown to half of dip rate
while (step_count > slowdown_steps)
{
digitalWrite(STEP_PIN, HIGH);
delayMicroseconds(run_step_dur/2);
digitalWrite(STEP_PIN, LOW);
delayMicroseconds(run_step_dur/2);
step_count--;
}

//slowdown distance reached, travel desired dip distance
at half of dip rate
while (step_count  > 0)
{
digitalWrite(STEP_PIN, HIGH);
delayMicroseconds(pre_dip_step_dur/2);
digitalWrite(STEP_PIN, LOW);
delayMicroseconds(pre_dip_step_dur/2);
step_count--;
}

delay(1000 * dwell_time);

digitalWrite(DIR_PIN, up);

//raise for desired dip distance at desired dip rate
while (step_count < slowdown_steps)
{
digitalWrite(STEP_PIN, HIGH);
```

```
delayMicroseconds(dip_step_dur/2);
digitalWrite(STEP_PIN, LOW);
delayMicroseconds(dip_step_dur/2);
step_count++;
}
delay(60 * 1000 * cooldown_time);
//travelled desired dip distance, now speed up to run
travel rate until platform reaches top
while (step_count < req_steps )
{
digitalWrite(STEP_PIN, HIGH);
delayMicroseconds(run_step_dur/2);
digitalWrite(STEP_PIN, LOW);
delayMicroseconds(run_step_dur/2);
step_count++;
}

digitalWrite(RELAY_PIN, HIGH);

delay(60 * 1000 * heat_time);

digitalWrite(RELAY_PIN, LOW);
}
}
while (dip_count == req_dips && digitalRead(SEL_SW) == LOW)
{
digitalWrite(GREEN_LED, HIGH);
delay(1000);
digitalWrite(GREEN_LED, LOW);
delay(1000);
```

```
}

}

}

}
```